Direct Identification and Counting of MicroRNAs in Single Cells by Transient Binding and Kinetic Fingerprinting

by

Karen Montoya

A dissertation submitted in partial fulfillment
of the requirements for the degree of
Doctor of Philosophy
(Chemistry)
in the University of Michigan
2023

Doctoral Committee:

        Professor Nils G Walter, Chair
        Professor Ryan Bailey
        Assistant Professor Kristin Koutmou
        Professor Muneesh Tewari

Karen Montoya

kmontoya@umich.edu

ORCID iD: 0000-0001-5029-5001

Dedication

Le dedico esta tesis a mi familia.
En especial a mis padres y sobrina.
Maria de la luz Cortés,
Martin Montoya,
y Jayleen Ramirez Corona

Acknowledgements

I would first like to thank my parents for their unconditional love and support.

Gracias mami y papi por darme oportunidades que ustedes no tuvieron. Completar mi tesis lejos de ustedes ha sido una de las experiencias mas dificiles que he tenido y no hay suficiente palabras para agredezerles por todo su amor y apoyo. Gracias por siempre creer en mi y por estar detras de todas mis metas. Me da mucho orgullo tenerlos de padres. Los quiero mucho!

I would like to thank my sister, Selene Ramirez, and my niece Jayleen Ramirez Corona for driving me across the country with my mom. It was not easy for a 2-year-old, but I'm grateful you helped ease my journey away from home. I feel fortunate to have had these lovely ladies help me settle in. They're not only my family, but my best friends and greatest motivators. Now, I am blessed with another baby motivator, my niece, Katelyn. I am also grateful to my brothers, Christopher Montoya and Allan Ramirez for their encouragement.

I would like to thank my advisor, Professor Nils Walter, for his guidance and encouragement that have helped me develop into the scientist I am today. He has impacted the single molecule community and established a successful research group I am glad to be a part of. I also thank my committee members Professors Kristin Koutmou, Muneesh Tewari, and Ryan Bailey, who have provided helpful feedback, mentorship, and support from the start of my graduate career.

I also owe thanks to the Walterians, current and alumni: Alex Johnson-Buck, Paul Lund, Adrien Chauvier, Zi Li, Andreas Schmidt, Lidan Li, Shiba Sundar, Liuhan Dai, Guoming Gao, Emily

Table of Contents

List of Tables

List of Figures

Abstract

Cancer is the second leading cause of mortality worldwide. Within the U.S. alone, it is estimated that 1.9 million people will be diagnosed this year and over 610,000 people are expected to perish. Despite advances in diagnostic and treatment strategies, a significant number of patients still develop late-stage cancer, where treatment options are inadequate. This suggests early detection is critical to reducing cancer morbidity and mortality, motivating interest in liquid biopsies, an alternative to invasive procedures. Body fluids like blood and urine are analyzed for biomarkers to detect cancer and regularly monitor disease. Of various biomarkers, circulating tumor cells (CTCs) provide substantial information for better understanding tumor biology and the metastatic cascade. With recent technological developments, molecular characterization of CTCs at the single-cell resolution is now possible, opening new windows into metastasis and laying groundwork for development of single cell technologies to diagnose and monitor disease.

MiRNAs are non-coding RNAs with pervasive gene regulatory function in higher eukaryotes. Although short in length, miRNAs regulate essentially all cellular pathways relevant to human health. Over the past few decades, it has become clear that due to their abundance and relative stability in body fluids, the levels of miRNAs in liquid biopsies can be compared between healthy individuals and cancer patients, making them suitable biomarkers of disease. Several technologies have been investigated and established for nucleic acid profiling. Current gold standards include the Polymerase Chain Reaction (PCR) and Next

Generation Sequencing (NGS). These techniques have high sensitivity and throughput, respectively, however they come with practical shortcomings. For instance, detection via PCR often introduces enzymatic amplification bias leading to false negatives. To overcome these pitfalls, our group developed a novel, innovative technology capable of direct single-molecule identification and counting of various analytes. Our approach, termed Single-Molecule Recognition through Equilibrium Poisson Sampling (SiMREPS), measures the transient binding of a detection probe to a target immobilized on a glass surface. The equilibrium binding of the fluorescent detection probe to the target is detected in a single molecule microscope and is distinctive in its kinetic signature, or fingerprint, a feature used to achieve ultra-high specificity. The ultimate vision of this dissertation is to develop a technology platform for the rapid, robust single molecule analysis of a panel of microRNA (miRNA) biomarkers in single human cancer cells utilizing SiMREPS.

After an introduction in Chapter 1, Chapter 2 focuses on the development of an *in situ* based detection platform, expanding the capabilities of SiMREPS. Here, a FRET detection scheme is developed to complement the new detection environment. In this chapter, the optimization of the technology workflow is described with a detailed strategy for FRET probe development to obtain desirable kinetic behavior and applied to miRNAs in single cells *in* situ. Chapter 3 focuses on the development of an assay utilizing microfluidics for isolation and lysis of single cells that will undergo SiMREPS analysis. Details of the optimization of the acquisition time, slide preparation, and incorporation of a system to improve sensitivity are discussed. A final Chapter 4 concludes the thesis and discusses future directions. Together, this thesis presents a proof-of-concept for using either *in situ* or microfluidic approaches to detect miRNAs in single

cells with the potential to better understand the mechanisms behind miRNA variability in single

cells for application in cancer diagnosis, prognosis, and monitoring.

Chapter 1 : Progress Towards a Single-Molecule Understanding of Single Cells[1]

1.1 Overview

In the seventeenth century, Robert Hooke and Antony van Leeuwenhoek paved the way for investigating a 'new visible World'. By the fabrication and use of microscopes, they uncovered the existence of microscopic organisms and set forth the theory that the cell is the basic structural unit of life[1].

The research presented in this thesis dives deep into the world of the cell with the quest of uncovering biomarker expression levels to profile the genetic composition of aberrant cells causing disease. This chapter introduces the fight against cancer and the significance of single cell work followed by a detailed overview of the biomarker class studied, microRNAs (miRNAs). I review the regulatory role of miRNAs and available profiling technologies. I then provide an introduction of single molecule fluorescence microscopy and its application in the assay design. Lastly, I focus attention on a novel technology that is capable of nucleic acid detection utilizing transient binding events – a foundational aspect of my assay design.

1.2 Battle Against Cancer: One Cell at a Time

Cancer is the second leading cause of death both worldwide and in the US alone [2,3]. Since the 1970s, we have come a long way in understanding the biology of this disease. However, we are still confounded by the complexity faced due to the genetic variability [4], making it a difficult battle to conquer. In the past decade, there has been a shift in the traditional "one-size-fits-all" model into molecular profiling for precision cancer therapies [5]. This emerging approach has, for the better, changed the battle against cancer by uncovering tumor-specific molecular profiles which can lead to improved diagnoses and tailored treatment plans [5,6]. In addition, during the course of the disease, it has come to knowledge that cancers become more heterogenous as they develop [7]. Heterogeneity leads to survival by providing "the fuel for resistance", analogous to the way bacteria develop resistance to antibiotics via mutation. Therefore, a specific diagnosis of tumor heterogeneity is key for the development of effective therapies [8]. More specifically, lethal metastases are seeded by circulating tumor cells (CTCs) (**Figure 1-1**) which maintain primary tumor heterogeneity and reproduce tumor properties, making them a potential therapeutic target [9]. Many scientists have demonstrated that indeed to be the case and they may be used for prognosis and efficacy assessment of treatment [9–11]. Previously, CTC analysis only required enrichment and enumeration [12], but we now know it is an incomplete diagnosis because of the heterogeneity of CTCs [10,13,14]. Multidimensional analysis of CTCs in combination with biomarkers such as miRNAs at single-cell resolution [14] could provide further information allowing identification of cell state and fate. As such, we enter a new challenge and need a solution – to develop and/or optimize methods with high levels of sensitivity and precision to study the molecular heterogeneity of CTCs at the single cell level

which will tremendously enhance our understanding of cancer biology and has the potential to revolutionize medicine as we know it.
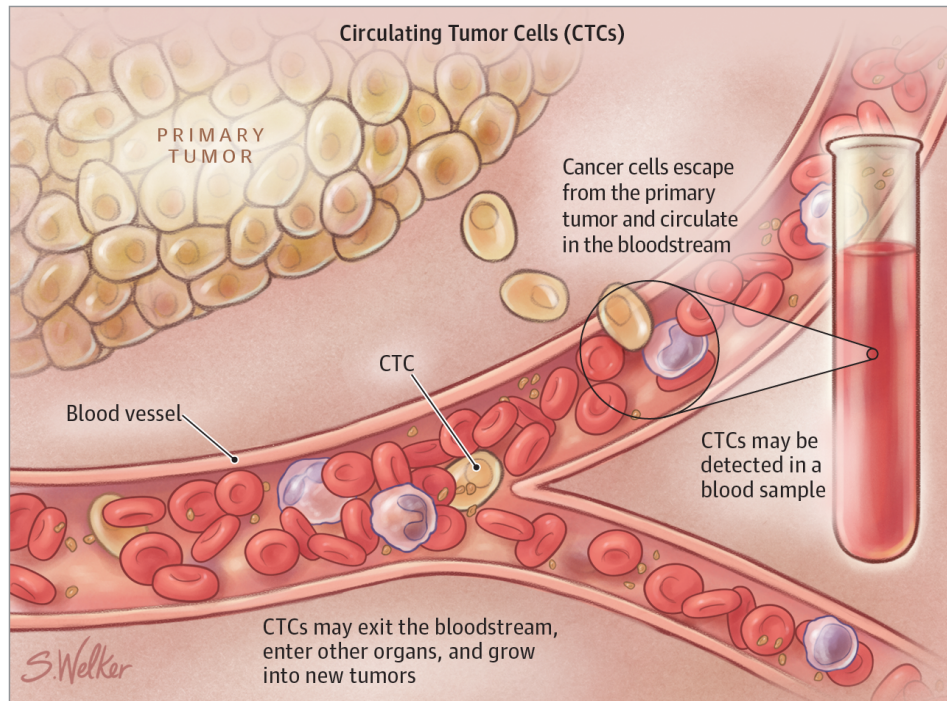
Figure 1-1 Depiction of cancerous tumors shedding circulating tumor cells (CTCs) which flow into the bloodstream. The CTCs may exit the bloodstream to grow into new tumors [15].

1.3 MicroRNAs as Master Gene Regulators

The central dogma provides the basic framework for how genetic information is transferred from DNA to a protein product by a messenger RNA [16,17]. For many years, it was believed that RNA just serves as a messenger. However, we now know different types of RNA exist in the cell. Advances have further revealed that less than 2% of DNA encodes for protein while the majority is transcribed into noncoding RNAs (ncRNAs) [18]. Noncoding RNAs are RNA molecules that are mostly not translated into a protein. Despite that, they have been shown to have functionally important regulatory roles in translation and stability of protein-coding genes. A particular class of ncRNAs, miRNAs, has been widely studied given their involvement in regulating gene expression.

Since their discovery in the 1990s with *lin*-4 in the model organism *Caenorhabditis elegans*, it was evident that miRNAs have a significant role in biology [19]. Since then, over 2,500 miRNAs have been catalogued across species with nearly 2,000 miRNAs identified in humans [20]. These endogenously expressed and processed small RNAs are typically ~22 nucleotides (nt) in length. They act as master gene regulators which function by binding to short complementary (6-8 nt) "seed" sequences in the 3'UTRs of target messenger RNAs (mRNAs) to typically downregulate the gene expression of target mRNAs at the post-transcriptional level [21,22]. Once bound, miRNAs can orchestrate repression of protein production through translational silencing or mRNA destabilization by activating a degradation machinery [21,23,24]. Furthermore, a single miRNA can act on hundreds of gene targets [21,25], and computational studies have predicted that miRNAs influence greater than 60% of protein-coding mRNA transcripts in humans [26]. Most importantly, this class of small noncoding RNA has been implicated in various biological processes including development [27], metabolism [28], cell growth and proliferation [29,30], as well as diseases including cancer [27,31–34].

1.3.1 Biogenesis & Mechanism

The biosynthesis of miRNAs involves a regulated multi-step pathway (**Figure 1-2**). MiRNAs must undergo several maturation steps before becoming active in gene regulatory functions. Biogenesis begins in the nucleus where miRNAs are transcribed by RNA polymerase II as primary miRNAs (pri-miRNAs) that fold into one or several stem-loop structures also known as hairpins. These pri-miRNAs are then cleaved into a ~70 nucleotide precursor miRNA (pre-miRNA) by a Microprocessor complex composed of Drosha (an RNAse III type endonuclease) and cofactor DGCR8. The pre-miRNA is then exported out of the nucleus into the

cytoplasm through the activity of Exportin-5 via the nuclear pore complex. In the cytoplasm, the pre-miRNA is further cleaved by the protein Dicer into a small double stranded RNA, a mature miRNA and its complementary strand. An Argonaut (Ago) protein then recruits the one strand, the mature miRNA, to form the RNA-induced Silencing Complex (RISC) while the other strand (passenger or miRNA*) is released and degraded [35]. Within the RISC complex, miRNAs proceed to target a specific mRNA sequence that will result in gene expression regulation in diverse mechanisms.
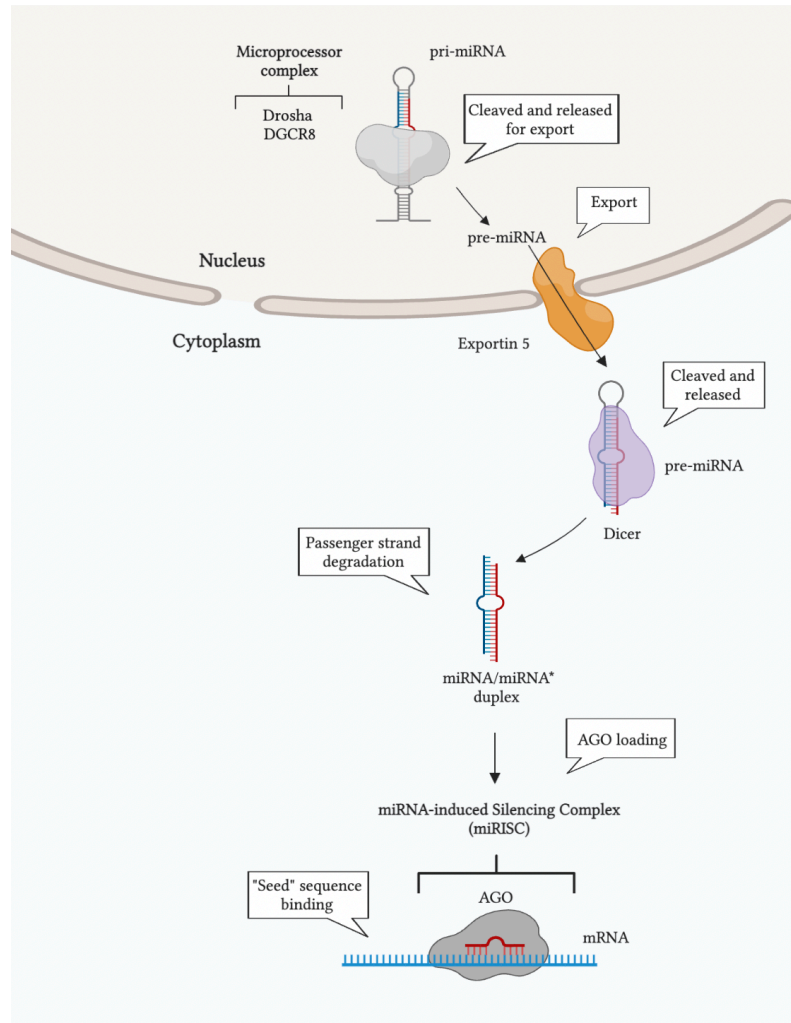
Figure 1-2 Overview of events in the miRNA biogenesis pathway. miRNA genes are transcribed in the nucleus by RNA Pol II as long pri-miRNA transcripts. The pri-miRNA sequence folds into a hairpin loops structure that is

recognized and cleaved by the Microprocessor complex Drosha-DGCR8, generating a pre-microRNA. The pre-miRNA is exported from the nucleus to the cytoplasm by Exportin 5, where it is further cleaved by Dicer, yielding a ~22 nt double-stranded RNA called the miRNA/miRNA* duplex. The functional mature miRNA is loaded together with Argonaute proteins (Ago) into the miRISC complex, guiding RISC to regulate gene expression. Figure generate using Biorender.

Translation regulation mechanisms were first discovered in *C. elegans* by the Lee *et al.* during their investigation of lin-4. In the discovery of lin-4 and its antisense complementarity to the lin-14 gene, their studies indicated a temporal decrease in lin-14 protein. From here on, various studies were performed on short RNA-mediated translation regulation mechanisms which include short-hairpin RNAs (shRNAs), small interfering RNAs (siRNAs), and microRNAs (miRNAs). As mentioned above, miRNAs undergo numerous processing steps after which a single ~22 nucleotide strand gets incorporated within a protein of the Argonaut (AGO) family possessing PIWI domains, and act as guides to direct the silencing RNA-protein complexes to their target RNAs. Typically, they bind to the sequence-complementary regions in the 3' untranslated regions (UTRs) of mRNAs. While other small RNA-based pathways such as siRNAs bind to 21-nt long sequence-complementary regions and stimulate AGO2's endonucleolytic activity. miRNAs, on the other hand, guide the RNA-induced silencing complex (RISC) via sequence complementarity to binding sites present on mRNAs, called miRNA recognition elements (MREs), and recruit mRNA degradation enzymes to the target.

A very remarkable characteristic of miRNAs mechanism is their ability to target, and in result, control the expression of hundreds of different mRNAs. This feature is possible due to the limited complementarity that is required for miRNAs to target mRNAs [36]. This creates a serious dilemma. On the one hand, miRNAs can contribute to a balanced regulation of gene expression. On the other hand, a slight variation in just one miRNA level can have a tremendous

impact on health. Due to this, it is vital to discover more mechanistic information on miRNAs as well as to detect and measure to understand their effect on a biological state.

1.3.2 MiRNAs as Biomarkers of Disease

An ideal biomarker must be stable, accessible, and demonstrate a good correlation to progression/severity of disease [37,38]. Considering the main role of miRNA in the human body, it is an appropriate molecule which can indicate health or disease. In fact, miRNA levels have been shown to remain stable across different perturbations [39]. Bioinformatic programs have predicted miRNAs control the translation of >60% of all protein-coding genes [26]. Experimental research has shown miRNAs have been linked to cancer [34,40,41] and other diseases [42,43], making them an attractive target for diagnosis, prognosis, and therapeutic exploration.

1.4 Profiling Technologies for Biomarkers

The detection and quantification of biomarkers have numerous applications in biological research and medicine. High specificity and sensitivity play a crucial role in a variety of clinical settings, including the early detection of disease, the assessment of the response to therapy, and the prognosis of disease relapse. Methods have been developed for analyzing nucleic acid biomarkers (**Table 1-1**), however, most techniques are challenging to implement for clinical use due to insufficient analytical performance, high cost, and/or other practical shortcomings. For instance, the detection of nucleic acid biomarkers by digital polymerase chain reaction (PCR) and next-generation sequencing (NGS) requires time-consuming nucleic acid extraction steps,

7

can often introduce enzymatic amplification bias, and can be costly when high specificity is required.

As described in **Section 1.3**, miRNAs have gathered a great interest as biomarkers due to their influence on many biological processes. Their expression patterns can be immensely rich in biological information making their detection of utmost importance. As such, there has been many efforts in the advancement of miRNA profiling technologies which will be summarized below. The strengths and shortcomings will be addressed to better discern their effectiveness and potential applications in research and/or clinical settings.

Table 1-1 Nucleic acid detection technologies and their analytical performance.

Technology	Quantitative	Amplification	Sensitivity (dynamic range)	Single-Nucleotide Specificity	Multiplexing ability	Instrumentation	Reagents
qRT-PCR [44–48]	Yes	Amplification-based	zM to fM	>95%	Limited	Real-time PCR instrument (e.g., ThermoFisher QuantStudio. Bio-Rad CFX96)	Extraction kits, primers, fluorogenic probes, thermostable polymerase, dNTPs
ddPCR [45,49]	Yes	Amplification-based	zM to fM	99.99%	Limited	Droplet generator + droplet reader (e.g., Bio-Rad QX100), thermal cycler	Extraction kits, droplet generation reagents, primers, fluorogenic probes, thermostable polymerase
Illumina sequencing (TruSeq) [45]	Yes	Amplification-based	zM to fM	>99%	High	Illumina sequencer (e.g., MiSeq, HiSeq, NovaSeq), thermal cycler	Extraction kits, library preparation kits, fluorescent dNTPs, thermostable polymerase, flow cells
Microarray [45,47]	Yes	Amplification-free	nM to mM	50-80%	High	Microarray plate scanner (e.g., AffyMetrix GeneChip HT)	Extraction and PCR/labeling kits, microarray chips
ADNA [50]	Yes	Amplification-free	aM to fM	Not available	Not available	Dark field microscope (e.g., Zeiss Axiovert 200M)	Probe-conjugated nanoparticles, patterned lipid arrays
NanoString [45]	Yes	Amplification-free	fM to nM	90-95%	High	nCounter system (e.g., nCounter *MAX*)	Flow cells, capture probes, fluorescently barcoded affinity probes
Simoa [51]	Yes	Amplification-free	fM to pM	>95%	Limited	Simoa analyzer (e.g., HD-1, SR-X)	Probe-conjugated microparticles, droplet generation reagents, primary and secondary detection probes, enzymatic signal developing reagents
Time gated FRET ligation [52]	Yes	Amplification-free	pM to nM	Not available	Limited	Fluorescence plate reader (e.g., ThermoFisher KRYPTOR)	FRET probes, adaptor probes, DNA or RNA ligase
SiMREPS [53]	Yes	Amplification-free	fM to pM	≥99.99999%	Limited	TIRF microscope (e.g., Olympus IX83, Oxford NanoImager)	Flow cells, capture probes, fluorescent probes

1.4.1 MiRNA Attributes and Considerations

To achieve specific detection of miRNAs, it is crucial to consider their characteristics. MiRNAs are small in size (~22 nt) making them difficult to be amplified. Their short length does not permit the use of traditional primers [54]. They also lack a poly-A tail which typically serves as selective anchor for poly-T primers as observed in mRNA profiling. Their size also affects specificity in detection by direct hybridization due to probe binding thermodynamics. Lastly, miRNAs share sequence homology across family members resulting in further challenges in specificity [55,56]. In addition, miRNA represents a low fraction (~0.01%) of total RNA [54]. To be able to assess individual miRNA copies requires a highly sensitive tool. As such, profiling of miRNAs is complex as there are many factors to consider. Nevertheless, a number of technologies have been successfully designed to overcome many of these barriers.

1.4.2 PCR-based Methods

The most widely used techniques to detect miRNAs, nucleic acids in general, are based on PCR [57]. Particularly, quantitative PCR (qPCR) is considered a gold standard for gene expression quantification and so many institutions have pursued development of qPCR for miRNA expression detection [58]. PCR exploits the differential hybridization efficiency of primers and probes to detect homologous nucleic acid sequences [59]. This feature has been extended into miRNA detection by utilizing a stem-loop primer [60] followed by a TaqMan probe fluorescence analysis [60,61]. Although, this results in an increase in specificity and sensitivity, the assay requires individual miRNA-specific fluorescent probes (FPs). This is a very costly assay and not receptive to high-throughput analysis.

In general, PCR itself can introduce artifactual sequence changes such as base substitutions during the amplification process through DNA polymerases and thermal cycling. This can lead to false positives when attempting to detect rare single-base mutations [53]. In addition, reverse transcriptases and ligases exhibit significant sequence biases which can also introduce significant artifacts including artificial differences in expression levels and can even result in the complete absence of certain sequences. Also, polymerases and ligases can be obstructed by contaminants such as heparin and heme, which would require further purification steps prior to amplification. This can become a huge problem when dealing with such a low concentration [54].

1.4.3 Hybridization Methods

Another technique utilized for miRNA profiling is microarrays, an oligonucleotide microchip [62]. Microarrays are one of the earlier methods used for parallel detection of miRNA. It functions by tagging miRNAs in sample with a fluorophore tag. The fluorescently labeled miRNA, upon hybridization to discretely "arrayed" capture probes, will allow for detection. The technique in general is advantageous due to its lower cost in comparison to other profiling methods, plus having a multiplexing ability [63]. Further, it avoids amplification-related copying errors and permits detection of targets that cannot be efficiently amplified by PCR. However, they suffer from their own set of challenges. They generally cannot detect single nucleotide variants at relative abundances below ~0.1% due to a finite thermodynamic discrimination factor between closely related sequences. This is exacerbated by the general principle that all miRNA probes on a microarray must undergo the same hybridization conditions although there is a variance in miRNA GC content. These hybridization conditions can lead to sequence-dependent differential hybridization affinities due to the wide variance in melting temperatures which may

result in either false positives due to non-specific hybridization as mentioned previously, or false negatives due to their inability to suppress nonspecific binding of probes to the detection surface.

1.4.4 Next Generation Sequencing

Another miRNA profiling approach is next generation sequencing (NGS) technologies. NGS is very popular due to its high-throughput sequencing of nucleic acids in a complex mixture for screening and early detection of cancer [64]. In this method, adapters are ligated to sample RNA and cDNA libraries are made and amplified by PCR. The libraries are then sequenced and the output reveals sequencing reads of varying lengths corresponding to miRNAs, which are then aligned to the reference sequence of choice [58]. The major advantage of the NGS platform, is that it offers the unique ability to detect novel miRNA within heterogeneous mixtures [65]. However, achieving high sensitivity and specificity with NGS requires high sequencing depth [66] to correct amplification and readout errors, which is time consuming and can often increases cost [67]. In addition to the high cost of instruments and reagents, there are bioinformatic challenges due to large quantities of data. The third generation of sequencing technologies currently under development could eventually provide lower-cost options [63].

1.5 Single Molecule Fluorescence Microscopy (SMFM)

Traditionally, molecules and life science in general have been studied by ensemble averaging. Paradoxically, we have an understanding that the cell is a complex mixture of many single molecules working collectively to sustain life. Although averaging of observations gives us a reasonably representative model, it removes our ability to study the diversity and complexity of functional networks, not to mention the loss of spatiotemporal information. The significant strides towards comprehending single molecules by enhancing single molecule fluorescence

techniques in the last couple of decades has allowed us to fill this gap in providing valuable insights that have greatly advanced our understanding of the structure, dynamics, and function of biomolecules. This section will highlight the importance of single molecule fluorescence through a brief history, followed by the fundamentals of fluorescence and a description of necessary modules and considerations for its application.

1.5.1 Brief History of SMFM

Fluorescence has been observed as early as the 15th century, perhaps well before then considering its existence in nature [68]. However, this phenomenon was not fully understood until George Gabriel Stokes published "On the change of refrangibility of light" in 1852 [69]. He was the first to describe the relationship between light absorption and fluorescence. Although "fluorescence" was understood then, the first observation of single enzyme molecules using fluorescence microscopy did not come until 1961 by Boris Rotman [70]. In 1989, Moerner and colleagues detected single dopant molecules of pentacene inside a solid crystal, but at liquid-helium temperatures [71]. In 1993, Betzig and Chichester obtained the first images of single molecules immobilized on a surface at room temperature [72]. Most relevant to my thesis work, in 1995 single molecule detection in aqueous solution was accomplished which paved the way for investigating and enhancing our understanding of how molecules work synergistically to sustain life and, in my case, making the detection of miRNA in [lysed] cells possible.

1.5.2 Fluorescence

Fluorescence microscopy is an invaluable tool in biological sciences that has allowed us to explore the molecular basis of life. It offers an exceptional signal-to-noise ratio for visualization in combination with high specificity of labeling with minimal perturbation to

biological samples permitting physiological features of native biological systems to remain intact [73]. The physical process of fluorescence involves absorbing a photon of light by a fluorophore and subsequently emitting a photon of lower frequency/longer wavelength. This process is illustrated by the Perrin-Jablonski 'single photon excitation' diagram shown in **Figure 1-3**. The absorption of energy promotes an electron from ground state to a higher state on a time scale of $\sim 10^{-15}$ s. Following this, the molecule is in a non-equilibrium state and will lose its energy through vibrational relaxation at a rapid timescale of $\sim 10^{-14}$-10^{-11} s. The electron will then return to its ground state accompanied by a photon emission, known as fluorescence, with a wavelength longer than the incident photon.
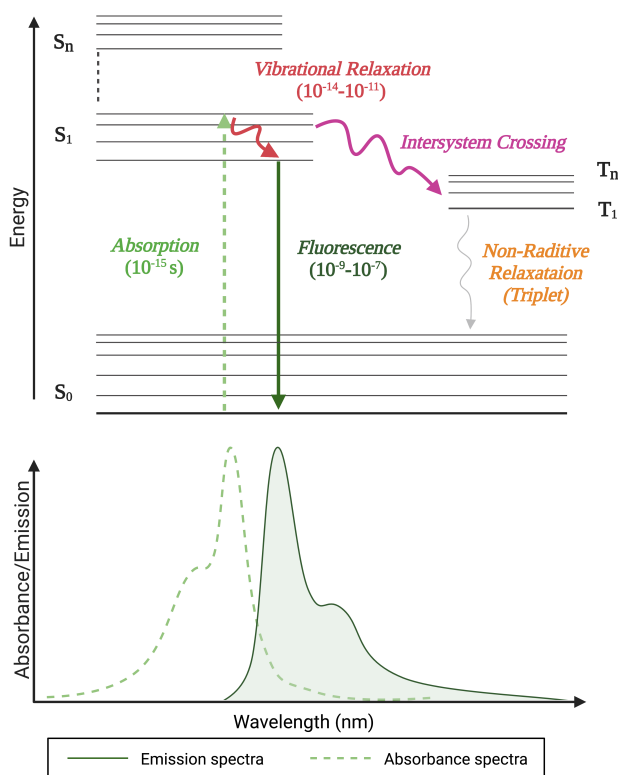
Figure 1-3 Jablonski Diagram displaying the energy states of a molecule. Molecules not absorbing energy are mainly confined to the lowest vibrational states of the ground state S_0. A molecule is promoted from its ground state to a higher state by absorption of a photon which is represented by the green dashed arrow. It is in a non-equilibrium state and will eventually dissipate the energy that it has gained and return to the ground state. That energy is lost is through vibrational relaxation (red arrow). Following this, the molecule returns to its ground state and a photon is emitted, termed fluorescence (green arrow). Figure generated using Biorender.

1.5.3 SMFM Experimental Overview

Single-molecule techniques are typically classified into two main categories, those based on optical observation and others based on the application of force to the system, such as manipulation by optical tweezers and imaging by atomic force microscopy [74]. A thorough explanation of the benefits and specifics of existing SMFM approaches to date are beyond the scope of this chapter, but have been reviewed elsewhere [73,75–77]. Instead, this section will focus on a brief overview of SMFM approaches and highlight the necessary modules and considerations for its application to the work of this thesis.

1.5.4 Illumination

SMFM approaches allow for imaging, localizing and/or tracking of single molecules. In traditional epi-fluorescence microscopy, light passes through the objective's optical axis and illuminates the entire depth of a sample with a specific wavelength, exciting fluorescent molecules within it. However, detecting the signal from single molecules could be challenging due to the whole sample illumination resulting in molecules present in other focal planes also getting excited, yielding a higher fluorescence background.

In general, detecting an individual molecule in the background of other molecules, non-specific binding, and instrumental noise can be challenging. Fluorescence plays a part in discerning true signal from background as emission from fluorescently labeled biomolecules is red-shifted relative to the wavelength of laser used for excitation. The Stokes shift, which is a spectral shift, between the excitation and emission wavelength maxima makes true fluorescence signal easily distinguishable from background.

Additionally, some common strategies to reduce background involve selective excitation. Schemes to illuminate a sample that achieve selective volume illumination include Total internal reflection fluorescence (TIRF) microscopy. Limiting the volume of illumination permits selective imaging of fluorescent molecules and improves signal-to-noise by decreasing out-of-focus emission as seen with an epi-fluorescence setup. TIRF was developed by Daniel Axelrod in the early 1980s and is one of the most frequently used imaging methods (**Figure 1-4**). In TIRF, the selective illumination is attained by propagating light through a medium of high refractive index followed by a lower refractive index medium. Its refractive behavior is dictated by Snell's law – when light strikes the interface of the two media at a sufficiently high angle, its refraction direction becomes parallel to the interface; while at larger angles, it is entirely reflected into the first medium of higher refractive index. Although the light does not go through the medium of lower refraction, the reflected light generates an evanescent field of excitation that extends ~100 nm deep into the sample. The energy of an evanescent field decreases exponentially with distance to the interface so only fluorophores immobilized on the imaging surface are excited resulting in a high signal-to-noise ratio, as fluorophores in the rest of the sample are hardly excited.
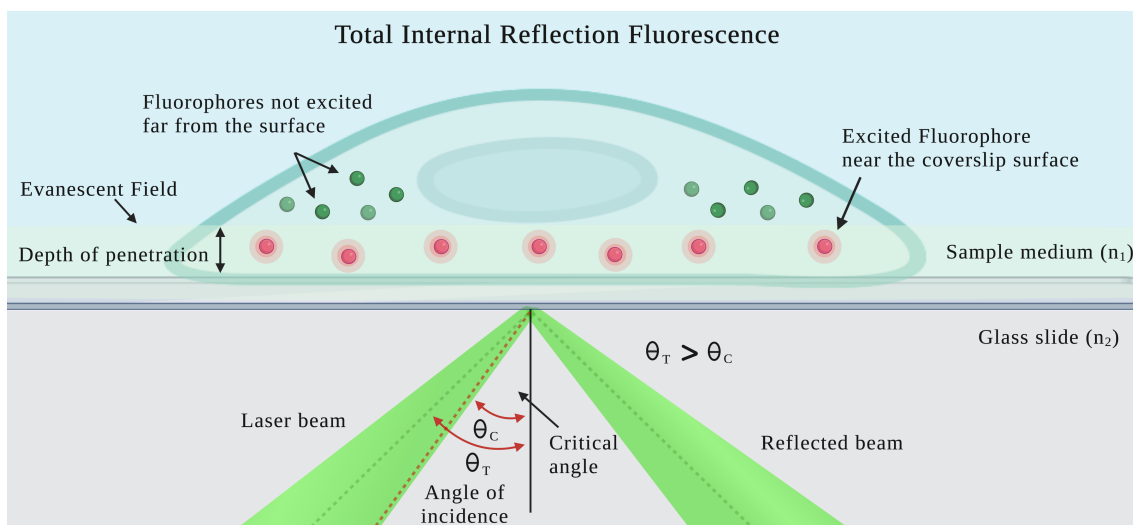
Figure 1-4 The optical basis of TIRF illumination. In TIRF microscopy, the excitation light is refracted parallel to the coverslip/sample interface at the critical angle, θ_C. When the excitation light travels at a high incident angle θ_T, which is greater than θ_C, the excitation light is totally internally reflected from the glass/sample interface and an evanescent field is generated on the opposite side of the interface. The intensity of the evanescent field decreases exponentially with the distance to the interface so only fluorophores close to the surface are significantly excited. To achieve TIRF, the refractive index of the sample (n_1) must be less than that of the coverslip (n_2). Figure generated using Biorender.

Another SMFM approach controlling the illumination area to reduce background is highly inclined and laminated optical sheet (HILO) illumination [77] also termed near-TIRF microscopy. Unlike TIRF, which is limited to imaging near the surface, HILO overcomes this limitation making it possible to do single molecule imaging inside cells. The incident laser beam is refracted into the sample at high inclination from the optical axis, thus illuminating a small lamina as a thin optical sheet within the sample. The thickness is dependent on the diameter of the illuminated field of view (FOV) and the incidence angle at the sample. HILO microscopy can achieve an imaging depth of up to ~10 µm and contains a *z*-component that allows for imaging of molecules that are located micrometers above the coverslip surface. These characteristics make HILO feasible for three-dimensional imaging of samples. Moreover, the excitation beam path for epi-illumination, TIRF and HILO are relatively similar, allowing a single microscope to be used to implement all three schemes.

A powerful biophysical technique which can be performed with TIRF and HILO microscopy is single molecule förster resonance energy transfer (smFRET). It is a distance dependent technique that allows for measurements at a scale of 2-10 nanometers (nm). With smFRET, two fluorophores, a donor and acceptor, exhibit FRET or the transfer of energy when they come within 2-10 nm. Typically, smFRET is utilized for studying specific interactions, intramolecular dynamics, and other.

1.5.5 General Experimental Design

Although there are different types of fluorescence-based approaches, key experimental elements are common to all these methods including sample preparation, fluorescent probes, detection of fluorescence, and data analysis, as discussed below.

1.5.6 Sample Preparation

To detect single molecules, it is key to carefully select the sample concentration. The concentration of molecules of interest should be kept low enough, in the picomolar to nanomolar range, to be able to distinguish one molecule from another. This helps in preventing multiple molecules to be detected which could result in averaging.

In general, many single molecule experiments are surface based. It is most suitable to immobilize molecules to the surface which allows for information to be collected for extended periods of times versus measuring freely diffusing molecules. But of course, it is practiced in the field and comes with its own set of challenges. As mentioned earlier, although in vivo imaging is a field of interest, this section will focus on surface-tethered experiments. Taking into consideration surface immobilization is often crucial for SMFM experiments, it is evident that the surface is a fundamental component. The surface needs to be free of impurities and have low

absorption to avoid non-specific binding. Many different surface cleaning and passivation approaches have been developed – one widely used method involves polyethylene glycol-succinimidyl valerate (PEG-SVA). This polymer is negatively charged, which prevents nonspecific adsorption of biomolecules.

1.5.7 Fluorophore

Single-molecule fluorescence measurements require a fluorophore to exist somewhere to detect the molecule of interest. The single molecule under study or a detector/reader probe must be conjugated to a fluorescent label or have a strong inherent fluorescence to be visualized. Synthetic dyes (Cy dyes, Alexa dyes, rhodamine dyes), fluorescent beads, quantum dots, and fluorescent proteins are common fluorescent probes used in SMFM. Small dyes i.e. cyanine (cy) dyes or Alexa dyes, are typically favored due to their small size hypothesized to introduce minimal perturbation to biological samples. Therefore, the molecule or read probe requires that typically a small-molecule fluorophore be incorporated into the sample in some way such as through NHS ester-, biorthogonal-, and immuno- labeling to name a few (**Figure 1-5**).
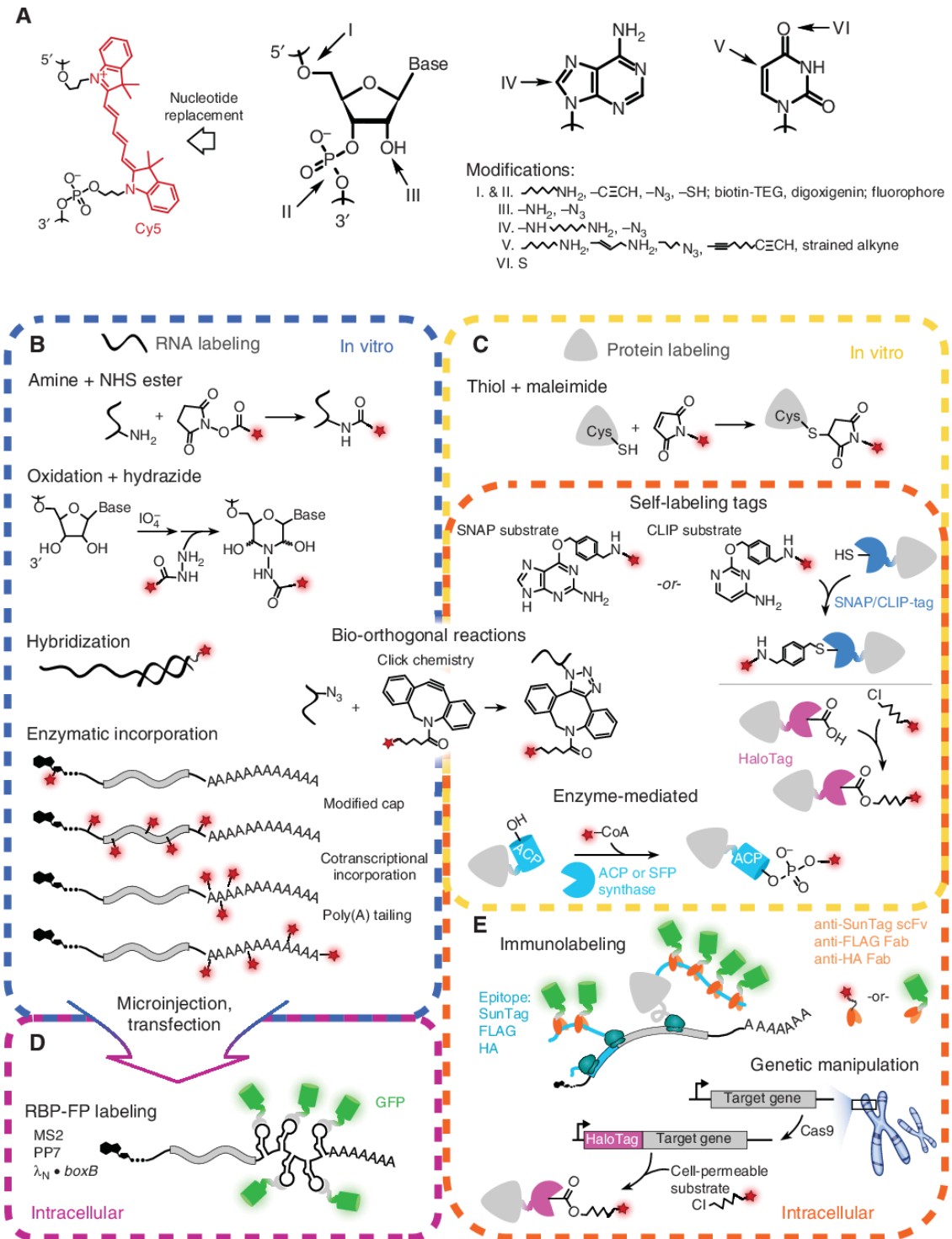
Figure 1-5 Labeling Strategies [78]

With respect to imaging, an ideal fluorophore for SMFM should be photostable and have

a high extinction coefficient and quantum yield. Intersystem crossing (triplet state excitation) and

photobleaching are undesirable processes that affect the quality and length of a single-molecule recording. Although the mechanism is unclear, molecular oxygen is thought to be primarily responsible for photobleaching via photo-oxidation of the fluorophore. Several chemical agents and enzymatic oxygen scavenging systems (i.e. glucoseoxidase and catalase or protocatechiuc acid, trolox, and protocatechuate-3,4-dioxygenase can be used to prevent photobleaching by oxygen. Trolox is used to quench triplet state excitation while, the enzyme systems scavenge oxygen. In addition, brightness, the product of a fluorophore's extinction coefficient and quantum yield, should be high enough for distinguishing signal from noise.

With respect to imaging in more complex biosystems, phototoxicity and autofluorescence can cause issues. Fluorophores, in their excited states, react with molecular oxygen in the cell, resulting in the accumulation of phototoxic free radicals that can affect in vivo experiments. Furthermore, naturally fluorescent molecules present inside cells absorb visible light and fluoresce, contributing to a high background level during imaging. As such, selection of excitation power and wavelength, and time acquisition are important parameters in order to alleviate potential autofluorescence as well as photobleaching.

1.5.8 Data Acquisition & Analysis

SMFM, particularly TIRF microscopy, typically utilize an electron-multiplying charge-coupled device (EMCCD) or scientific complementary metal-oxide-semiconductor (sCMOS) camera to achieve appropriate sensitivity. Both EMCCD and sCMOS cameras do state up to 95% quantum efficiency (QE), meaning there is a 95% probability of a photon being absorbed and converted into an electron in the silicon sensor. EMCCDs amplify the number of photoelectrons through a unique electron multiplying structure built into the chip.

With respect to analyzing collected data, a brief description will be provided for select microscopy methods. For localization microscopy (i.e. stochastic optical reconstruction microscopy), a series of diffraction-limited images are acquired, each containing point-spread functions (PSFs) produced by a sparse set of emitting fluorophores [79,80]. The emitting fluorophores are then localized with high precision. Following this, combining all the recovered emitter positions from each frame, a super-resolved image is produced with resolution typically an order of magnitude better than the diffraction limit (to under 20 nanometers) [80]. Similarly, for Förster resonance energy transfer (FRET) and/or experiments looking at many molecules simultaneously, the emitting fluorophores are identified. But instead of combining all frames, the intensity of each emitter is then tracked as a function of observation time/frames to generate single molecule traces. The traces typically contain some type of fluctuations which allows for the investigation of interactions between neighboring molecules/molecular dynamics such as uncovering distinct patterns of dynamic RNA folding behavior. The hidden Markov model (HMM) [81], initially developed for speech recognition[82], has become a common method used to analyze this type of data. It uses a multi-state model to "idealize" noisy traces into a series of transitions between discrete states. In addition, the Bayesian information criterion (BIC) [81] and the Akaike information criterion (AIC) for model selection is utilized in hidden Markov models (HMM) when the number of states is unknown. While this standard approach has the advantage of simplicity, attempts are still being made at streamlining this analysis pipeline (i.e., using deep learning algorithms) [83].

1.6 Single-Molecule Recognition through Equilibrium Poisson Sampling Assay (SiMREPS)

Methods for detecting and quantifying disease biomarkers with high specificity and sensitivity play an important role in enabling clinical diagnostics as well as uncovering new

biology. The most widely used molecular biomarkers include proteins, nucleic acids, metabolites, and other small molecules. Detection and/or quantification of these disease biomarker is crucial for numerous applications as diverse as prenatal diagnostics [84], gene expression analysis [85], identification of genetic risk factors in disease [86], detection of sequence polymorphisms [87], quantification of telomerase activity [88], detection of pathogens [89], and identification of genetically-modified organisms [90]. Highly specific detection of low-abundance single-nucleotide variants (SNVs) in a large excess of wild-type sequences is increasingly important in clinical diagnostics of cancer and other diseases [91,92]. While various methods have been developed for analyzing biomarkers addressed in Section 1.4, most techniques are challenging to implement for clinical use due to inadequate analytical performance, high cost, and/or other practical shortcomings.

The gold-standard methods for detecting nucleic acids include polymerase chain reaction (PCR) and next-generation sequencing (NGS). PCR-based detection methods rely on enzymatic amplification steps in which a small number of target nucleic acid molecules in the sample are exponentially amplified for increasing sensitivity. However, PCR amplification introduces errors caused by heat-induced chemical damage (i.e. nucleotide deamination and oxidative damage) [93,94] and imperfect copying fidelity of DNA polymerases (can be susceptible to inhibition by contaminants i.e. heparin and heme) [53,95]. Such errors can be exponentially amplified during thermal cycling in PCR. Thus, the necessity of amplification in PCR-based methods imposes limits on the specificity of nucleic acid detection, particularly for SNVs. Next-generation sequencing (NGS) technologies digitally tabulate the sequence of many individual nucleic acid fragments, offering the unique ability to detect nucleic acid sequences within heterogeneous mixtures without prior knowledge [96]. However, to detect rare SNVs, NGS typically depends

23

on high sequencing depth, at considerable increase in cost, and/or targeted PCR of specific genetic loci. To address the drawbacks of these existing technologies and establish a universal diagnostics platform capable of detecting different types of analytes, a new approach termed Single Molecule Recognition through Equilibrium Poisson Sampling (SiMREPS) has been developed. SiMREPS is a SMFM method. Below there will be a detailed section of its general experimental design and analysis as seen for Section 1.5.

1.6.1 Kinetic Fingerprinting Technology

In 2006, Hochstrasser and colleagues introduced pointillist super-resolution imaging technique PAINT (Points Accumulation for Imaging in Nanoscale Topology), which relies on the repetitive interrogation of nanoscale structures by transiently binding dye molecules. Subsequently, Jungmann *et al.* adapted this concept to transiently binding oligonucleotide fluorescent probes, giving rise to a family of methods known as DNA-PAINT. Taking inspiration from these methods, SiMREPS employs the transient binding of FPs not for the imaging of nanoscale features but to generate distinctive temporal patterns (kinetic fingerprints) for the high-confidence detection of single-molecule analytes [53,67,97–99].
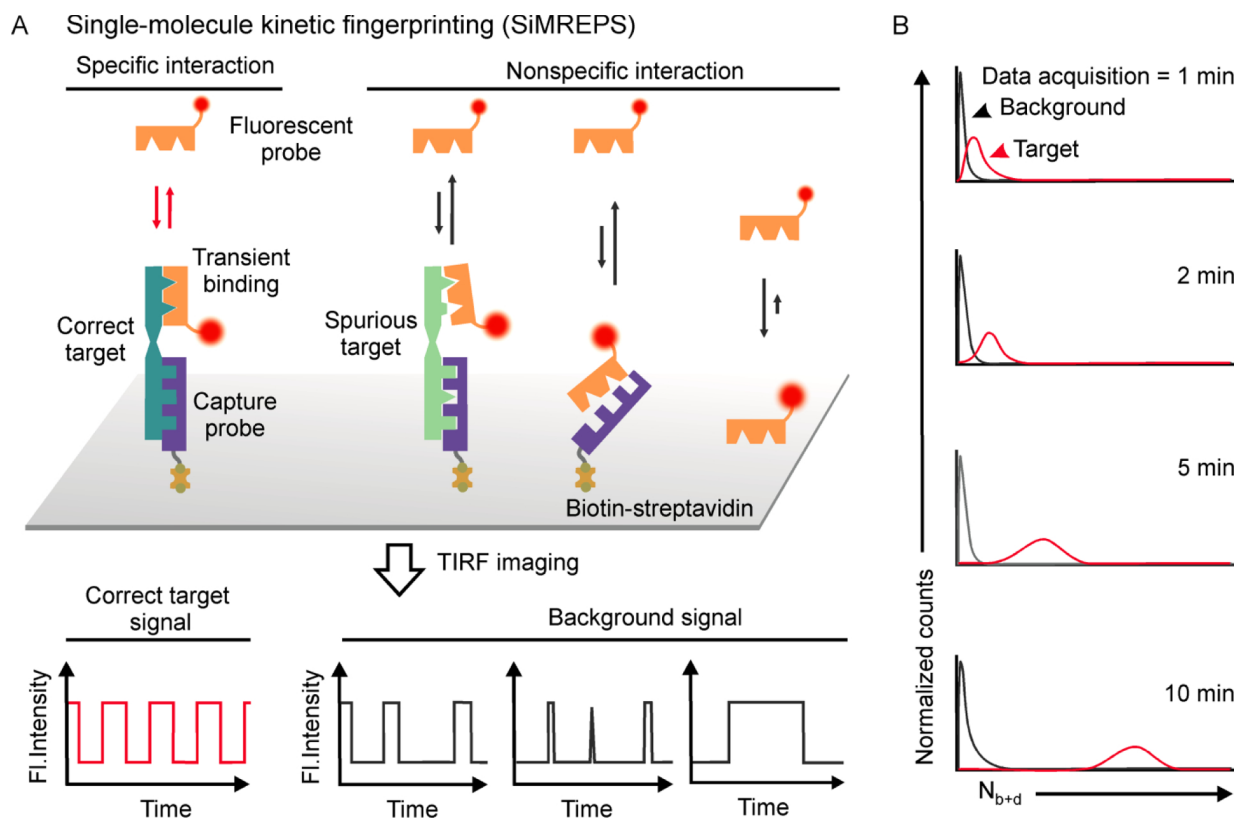
Figure 1-6 Schematic of the principle of single-molecule kinetic fingerprinting (SiMREPS) method. A) SiMREPS uses the transient and reversible binding of fluorescent probes to immobilized target molecules to generate disting kinetic fingerprints that permit high-confidence differentiation between specific binding to correct target and nonspecific background binding. Probe binding and dissociation to single molecules is observed in real time by TIRF microscopy. B) Predicted distribution of the number of binding and dissociation (N_{b+d}) events as a function of time. With increasing acquisition time, a better separation is obtained between specific and nonspecific or background binding [67].

For SiMREPS detection, any analyte of interest that can be stably bound to a surface and probed repeatedly is a candidate (**Figure 1-6**). SiMREPS employs TIRF microscopy to suppress background fluorescence from the freely diffusing FPs present in the imaging solution, thus permitting single-molecule detection at or near the surface of a slide or coverslip. The repeated binding of FPs to individual analyte molecules can be modeled as a Poisson process with random arrival times of individual FPs but a well-defined mean number (μ) of binding and dissociation events (N_{b+d}) per target molecule for a given observation time and a standard deviation (σ) proportional to (and theoretically equal to) N_{b+d} [99,100]. As a result, the coefficient of variation

(CV = σ/μ) decreases as N_{b+d} increases [99], implying that any kinetic difference between specific and nonspecific binding, no matter how small, can be resolved with a sufficiently long observation period. Below, a description of both theoretical and practical considerations for the ultraspecific detection of biomarkers using SiMREPS will be presented.

1.6.2 Experimental Considerations for Single-Molecule Kinetic Fingerprinting by SiMREPS

SiMREPS achieves extremely high specificity in single-molecule detection by monitoring the repeated, transient interaction of FPs to individual analyte molecules over time [97] which are typically captured at or near the surface of a microscope slide or coverslip for time-resolved imaging. There will be a focus on assay chip preparation, sample preparation & assay conditions, and data acquisition & processing.

Assay Chip Preparation

In principle, the SiMREPS concept is compatible with any sample geometry that permits the observation of single FP binding under relatively low oxygen conditions. In practice, the sample chamber design varies depending on the type of microscope used (i.e., prism-type or objective-type TIRF) as well as the desired throughput and sensitivity [99]. Objective-type TIRF permits an open-top chip design and requires only a single substrate functionalized for sample immobilization (i.e., a glass coverslip); sample wells are constructed by cutting pipet tips or 3D printed wells and attaching them to passivated coverslips. In contrast, prism-type TIRF usually requires placing the sample cell between a prism and an objective lens. In this case, closed flow cells sandwiched between a passivated microscope slide (fused silica or glass) and a glass

coverslip are preferred. The coverslips or slides are functionalized with an aminosilane followed by a mixture of succinimide esters of biotin-PEG and methoxy-PEG in a certain ratio (e.g., 1:10 or 1:100) and further passivated by disulfosuccinimidyl tartrate to quench the unreacted amine groups. Subsequently, the surface is coated with streptavidin to permit the immobilization of biotinylated CPs. In the case of in situ analyte SiMREPS detection within cells (e.g., miRNAs [101]), objective-type TIRF is used together with glass-bottom cell culture dishes. Cellular fixation is performed using treatment with paraformaldehyde or 1-ethyl-3-(3-dimethylaminopropyl) carbodiimide (EDC). The fixed cells are ethanol permeabilized prior to imaging [102].

Sample Preparation and Assay Conditions

As mentioned above, SiMREPS does not require enzymatic amplification and have shown robust performance in a variety of buffers and minimally treated crude biofluids. Detailed sample preparation and assay protocols are described elsewhere. Briefly, dsDNA samples require a short denaturation (e.g., heating to 80-95°C for 3 min) in the presence of carrier oligonucleotides (e.g., dT_{10}) and cooling to room temperature before surface capturing. For the direct capture of miRNAs from serum or cell extract, samples can be pretreated with sodium dodecyl sulfate (SDS) and proteinase K. Protein analytes have been directly captured from 1 or 25% serum and can be detected without washing away excess serum or detection probes. Notably, like other techniques utilizing passive surface capture, the sensitivity of SiMREPS is limited by analyte diffusion to the surface and by the capture kinetics, typically yielding capture efficiencies of ~1%. Nevertheless, limits of detection of <10 fM are typical.

The imaging buffers for most SiMREPS assays contained 25-100 nM FP in $1\times$ to $4\times$ PBS buffer. To prolong the usable lifetime (i.e., reduce the photobleaching rate) of fluorophores for more accurate and reproducible kinetic fingerprinting, an oxygen scavenger system comprising 3,4-dihydroxybenzoate, protocatechuate dioxygenase, and Trolox is typically added as mentioned in Section 1.5.7. In protein-SiMREPS assays, Tween 20 is often added to the imaging buffer to reduce the nonspecific binding of FPs to the imaging surface. To achieve the desired repetitive binding of FPs to targets yielding reproducible kinetic fingerprints distinct from the background, it is important to control the imaging temperature ($\pm$ 2 °C) and the ionic strength.

Data Acquisition and Processing

Data acquisition, as mentioned in Section 1.8.1 is typically performed on a pTIRF or oTIRF microscope, using an excitation intensity of 10-100 W/cm^2 at a wavelength near the excitation maximum of the fluorescent dye employed (e.g., a 640-nm continuous-wave laser with an output power of 25 mW is typically used to excite Cy5 or Alexa Fluor 647). Fluorophores excited toward the red end of the visible spectrum are particularly attractive for biological samples because of the relatively little autofluorescence of most biological samples in this range of wavelengths. Wide-field detection is usually accomplished using an electron-multiplying charge-coupled device (EMCCD) or scientific complementary metal-oxide-semiconductor (sCMOS) camera with a frame exposure time of 100-500 ms, or the fastest frame rate that provides sufficient signal-to-noise for accurate determination of kinetics (typically a signal/noise ratio of 3-10 for single fluorophores). The optimal excitation intensity and camera exposure time depend on probe concentration as well as the molar extinction coefficient, quantum yield, and photostability of the chosen fluorophore.

For each sample analyzed, data are collected from multiple fields of view, resulting in multiple movies recording the repeated binding of single FP molecules to the imaging surface. After movies are collected, they are subjected to further data processing to determine which fluorescent signals originate from FP binding to the target (as opposed to nonspecific binding to the surface or other surface-bound molecules). MATLAB scripts are used to (1) identify regions of the image with frequent fluctuations in fluorescence intensity, (2) calculate in- tensity versus time trajectories (or "traces") for each candidate region of the image, (3) perform hidden Markov modeling (HMM) to establish the number of transitions between bound and unbound states (N_{b+d}) as well as the lifetime in each state (τ_{bound} and $\tau_{unbound}$), and (4) use filtering criteria to differentiate true positives from background. Typical filtering criteria include: minimum signal-to-noise ratio, minimum intensity difference between bound and unbound state, minimum number of binding and dissociation events (N_{b+d}) per trace, minimum and maximum values for the median lifetimes in the bound ($\tau_{bound,\ median}$) and unbound ($\tau_{unbound,\ median}$) states in each trace. The appropriate thresholds for these values must be determined empirically by comparing positive and negative control experiments. To obtain the greatest difference between kinetic fingerprints generated by the target and nonspecific binding, optimizations can be made to the probe design or experimental conditions which will be further discussed in Chapter 2.

For this thesis, the main application of SiMREPS will focus on miRNA detection in view of their link to various types of cancer with the intention of providing a low-cost, robust, highly specific, and sensitive platform for the use of early detection of disease, prognosis, and indicators of successful treatment plan.

1.7 Single Cell Analysis

Cell-to-cell heterogeneity is always present within a cell population and understanding the differences within a population can be critical to uncover distinctive functions and fate. These cell-to-cell differences in RNA and protein expression can be key to answering questions in cancer, developmental biology and other. Conventional assays used for analysis of a population of cells, resulted in masking individual cell phenotype and genotype. For example, a tumor microenvironment is an intricate heterogenous system consisting of cells working in concert. This diversity results in different kinds of cells with unique behaviors presented in different implications in pathogenic conditions such as the capacity for local invasion and metastasis [103]. This variation in behaviors across cells motivated the emergence of single cell analysis to better understand the diversity of cells.

This thesis focused on single-cell analysis to get a clearer understanding of the genetic diversity in cancer. Tumor ecosystems are composed of various cells which interact and collectively dictate disease progression, including response to treatment [104,105]. It is widespread knowledge that cancer treatment options do not work efficiently for every cancer patient which has shifted physicians toward precision medicine [5]. Single-cell analysis permits better characterization of the whole tumor microenvironment and allows for diagnosing, monitoring disease progression, and investigating the response and rejection to treatment to improve personalized treatment strategies.

1.8 Overview of Dissertation

In the following chapters, I describe an assay design founded on SMFM to investigate the expression levels of a panel of miRNAs in single cells. I will discuss how smFRET, SMFM and kinetic fingerprinting put together allows for a faster, quantitative assay and expands the

capabilities of SiMREPS from surface-based to *in situ* application. Additionally, I will discuss further application of SiMREPS with microfluidics for an alternate, higher throughput advancement in the technology.

In Chapter 2, I describe the integration of smFRET and SiMREPS for *in situ* detection of single miRNA molecules. By designing and optimizing a pair of FRET probes, I demonstrate the ability of *in situ* detection with a simplified approach which accelerates detection quicker than traditional miRNA *in situ* hybridization methods. A detailed guide on cellular and imaging conditions will be thoroughly discussed.

In Chapter 3, I present an alternative method utilizing microfluidics with the goal of achieving the design of a high-throughput (automated) diagnostic tool. I demonstrate the capability of detection in single cell lysates with an increased sensitivity in contrast to the traditional SiMREPS assay. This chapter will provide a detailed guide on the optimization to the acquisition time, slide preparation, and incorporation of a system to improve sensitivity.

Together, this thesis presented a proof-of-concept for using *in situ* and microfluidic approaches to provide new insight on technologies that can be used for profiling and better understanding the mechanisms behind miRNA variability. The synergistic effort between the powerful techniques described both in Chapter 2 and 3 show a powerful means to uncover heterogeneity across single cells which in result has great potential for a remarkable development in precision medicine.

Chapter 2 : *In situ* Detection of Single MicroRNA Molecules by Transient Hybridization Utilizing FRET-based Probes

2.1 Overview

The accurate detection and quantification of miRNAs is important for accelerating our understanding of their influence on signaling pathways as well as for their adoption as diagnostic biomarkers. Recent advances in miRNA detection, include the use of cellular imaging techniques [106,107] because these approaches do not require cell lysis and RNA extraction which can have downstream effects due to yield and RNA damage. However, like many current techniques used for quantification of microRNAs, many rely on amplification via PCR, which results in errors emerging from heat-induced chemical damage, limited fidelity of the DNA polymerase, and other constraints (Refer to **Section 1.4**). Comparatively, there are challenges with detection reliant on hybridization-based probe, such as RNA-FISH, due to a finite thermodynamic discrimination factor between closely related sequences which requires up to 15 hours of incubation to achieve specificity [108]. To overcome these limitations, we adapted SiMREPS to develop an intracellular single-molecule microRNA quantification method. SiMREPS is amplification-free, requires no RNA extraction, and has no thermodynamic limitations. In contrast to the previous SiMREPS detection strategy, FRET-based probes were adapted to enable intracellular single molecule imaging. This approach exploits the direct binding of two short fluorescently labeled probes to a crosslinked miRNA analogous to SiMREPS, a method that has been successfully used to detect microRNA and DNA strands with a limit of detection around 1

femtomolar. Together, SiMREPS and intracellular image will allow for quantification, analysis of spatial information and significantly improve data acquisition.

2.2 Introduction[2]

Noncoding RNAs, such as miRNAs, have been shown to have functionally important regulatory roles in translation and stability of protein-coding genes [21–24]. The critical role miRNAs play in ¶ gene regulation and biological function, underscored in their dysregulation in tumor cells and presence as biomarkers in biopsies of cancer patients [109,110], warrants further investigation. While current techniques have implicated of miRNAs in an abundance of cellular pathways relevant to human health and disease [34,40–43], the use of PCR and/or hybridization can lead to false positives and negatives [53,54]. On the other hand, imaging techniques such as single-molecule fluorescence in situ hybridization (smFISH), offer an invaluable approach for the localization and quantification of nucleic acids at the single-cell level with single-molecule resolution [111,112].

In smFISH, a multitude of fluorescent dye-labeled oligonucleotide probes designed to be complementary to the target nucleic acids are introduced into fixed cells and allowed to hybridize to the analytes within the cell, and their accumulation on the target and location are detected via fluorescence microscopy. The smFISH approach has been widely applied to the detection of long RNA (especially mRNA) in single cells to better understand the regulation of

---

gene expression [113,114]. However, performing smFISH is often challenging due to 1) the low abundance of many analytes (i.e., many RNAs) in a single cell; 2) the limited sequence "real estate" on short target molecules to accumulate a detectable number of probes; and 3) the poor signal-to-noise ratio due to cellular autofluorescence and the inability to completely wash away un-bound probes [115]. To combat these problems, we adapted SiMREPS due to its very low background which may provide a more general solution to the challenges of detecting single, low-abundance analytes in fixed cells and tissues. In principle, the additional time axis of the kinetic fingerprint allows for better separation between signal and background in analyte detection compared to conventional smFISH approaches [67,97–99]. Recently, Li et al. [101] have used SiMREPS together with a novel type of probe fabricated on fluorescent polymer nanoparticles, termed a nanoflare, to detect cellular miRNA molecules *in situ*. Single-molecule sensitivity and single-mismatch specificity of detection of miRNA without any amplification steps were also demonstrated *in vitro*. Despite the high accuracy and low risk of photobleaching using a nanoflare, the preparation of the polymer nanoparticle and conjugation to a DNA probe makes the detection scheme more complicated. Additionally, potentially high intracellular concentrations of miRNAs may pose challenges to the accuracy of quantification as the signal may be oversaturated. This motivated the development of a simpler approach in which a different SiMREPs probe strategy, FRET-based probes were utilized. FRET is a highly sensitive, biophysical technique based on a distance dependent physical process in which energy transfer occurs between two fluorophores, a donor, and an acceptor. Implementing FRET-based probes not only results in an increase of specificity in comparison to one short probe utilized by Li et al., but it reduces the potential issue of signal saturation in presence of elevated levels of miRNA since the read-out probe will only be detected in presence of the donor probe. Here, we

developed and optimized an assay capable of detecting miRNAs utilizing FRET-probes for application of *in situ* detection of single miRNA molecules (**Figure 2-1**).
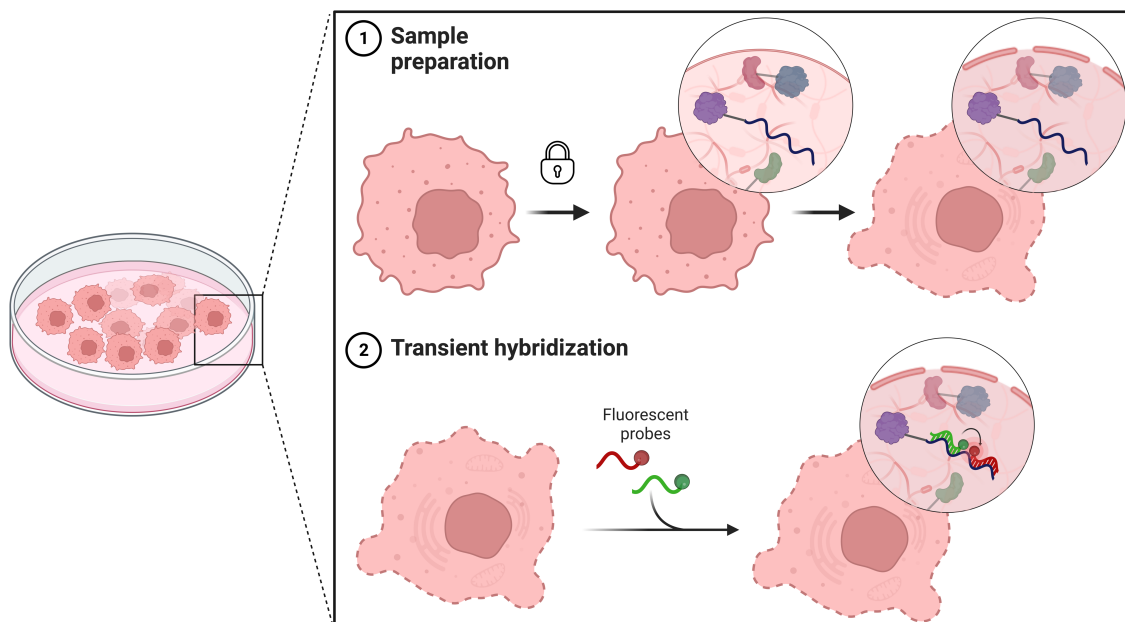
Figure 2-1 Schematic of in situ detection via FRET based probes. Cells are cultured in a cell flask, followed by seeding into wells with a coverslip bottom. Sample preparation consists of fixation of cells and then permeabilization. Finally, fluorescent probes are introduced which will undergo transient hybridization which will be monitored over time to allow for identification and counting via kinetic fingerprinting. Figure generated using Biorender.

2.3 Materials and Methods

2.3.1 Reagents and Consumables

All oligonucleotides were purchased from Integrated DNA Technologies (IDT). Biotinylated miRNAs were purchased with high-performance liquid chromatography (HPLC) purification. A locked nucleic acid (LNA) probe was purchased with a 5' Amino modification usable for subsequent Cy3 labeling via a monoreactive dye pack (Sigma Aldrich, Catalog no. GEPA23001). Fluorescent probe oligonucleotides were purchased with either a 5′ or 3′ fluorophore modification and high-performance liquid chromatography (HPLC) purification. All DNA probes were purchased with standard desalting purification. See **Table 2-1** for all oligonucleotide sequences used in this chapter. To detect each respective miRNA, a Cy3- and

Cy5-labeled fluorescent probes were specifically designed for their corresponding target and were used as a FRET pair in both *in vitro* and *in situ* experiments. All relevant melting temperatures, or T_m values of probes were calculated using the IDT oligo analyzer at 25 nM nucleic acid and 580/870 mM Na+ concentration. All the oligonucleotides concentrations were measured via UV-Vis spectroscopy and then were aliquoted and stored at -20°C prior to use. Streptavidin (S-888) was purchased from Invitrogen. 10× Phosphate-buffered Saline (PBS, pH 7.4, Catalog no. 70011044), Trolox (Catalog no. MFCD00006846), 3, 4-Dihydroxybenzoic Acid (PCA, Catalog no. AC114891000) were purchased from Fisher Scientific. Protocatechuate 3,4-dioxygenase (PCD, P8279-25UN), 1-Methylimidazole (Catalog no. 336092), (3-aminopropyl)triethoxysilane (APTES, Catalog no. A3648) l-Ethyl-3-(3-dimethyl aminopropyl) carbo-diimide (EDC, Catalog no. E7750) were purchased from Sigma-Aldrich and methoxy-polyethylene glycol-succinimidyl valerate (mPEG, MW, 5000), biotin-polyethylene glycol-succinimidyl valerate (biotin-PEG, MW, 5000) were purchased from Laysan Bio, Inc. Disuccinimidyl tartrate (DST) was purchased from Soltec Ventures. Bis-Acrylamide 19:1 (40% Solution) solutions of 19:1 was purchased from Fisher Scientific (Catalog no. BP1406-1). SYBR Gold was purchased from Thermo-Fisher (Catalog no. S-11494). To image fixed cells, an 8 well glass bottom slide was utilized. The μ-Slide 8 Well Glass Bottom was purchased from Ibidi (Catalog no. 80827).

Table 2-1 Detail of sequences of oligonucleotides

ID	Sequence 5'-3', T_m (4×/6× PBS)	Remark
biotin-let-7a	/biotin/UGAGGUAGUAGGUUGUAUAGUU	biotinylated RNA target
let-7a FP.SW	/Cy5/ACTATACAAC, T_m = 17.4/18.5 °C	Cy5 detection probe
let-7a Cy3FP1	/Cy3/ACTACCTCA, T_m = 28.2/29.2 °C	Cy3 detection probe
let-7a Cy5FP1	AACTATACAA/Cy5/, T_m = 15.5/16.8 °C	Cy5 detection probe
let-7a Cy5FP2	AACTATACAAC/Cy5/, T_m = 20.5/21.7 °C	Cy5 detection probe
let-7a LNA probe	+AC+TAC+CT+CA, T_m = 35.6/36.6 °C	LNA detection probe

		blocker
let-7a LNA Cy3 FP	/Cy3/+AC+TAC+CT+CA, T_m = 35.6/36.6 °C	Cy3 LNA detection probe
let-7a inhibitor	AACTATCAACCTACTACCTCA, T_m = 58.3/59.6 °C	let-7a DNA blocker
biotin-miR-21	/biotin/UAGCUUAUCAGACUGAUGUUGA	Biotinylated RNA target
hsa_miR-21_P1	/Cy5/UGAUAAGCU, T_m = 17/18 °C	Cy5 RNA detection probe
miR-2 inhibitor LNA	TC+AACATCAG+TC+TGATAAGC+T, T_m = 61.4/62.8 °C	miR-21 LNA blocker
miR-21 non-seed FP	/Cy5/UCAACAUCA, T_m = 17.5/18.6 °C	CY5 RNA detection probe
miR-21 Cy3 FP1	/Cy3/CTGATAAGCTA, T_m = 28.6/29.8 °C	Cy3 detection probe
miR-21 Cy5 FP1	TCAACATCA /Cy5/, T_m = 17.5/18.6 °C	Cy5 detection probe
miR-21 Cy5FP2	TCAACATCAG/Cy5/, T_m = 22.2/23.2 °C	Cy5 detection probe
miR-21 CP block	TAG CTT ATC AG, T_m = 29.4/30.5 °C	Detection probe blocker
biotin-miR-16	/biotin/UAGCAGCACGUAAAUAUUGGCG	Biotinylated target
miR-16 FP	/Cy5/GCC AAT ATT, T_m = 23.2/24.4 °C	Cy5 detection probe
miR-16_FRET_Cy5	/Cy5/TG CTG CTA, T_m = 22.9/23.8 °C	Cy5 detection probe
miR-16_FRET_Cy3	CG CCA ATA TTT/Cy3/, T_m = 34.4/35.6 °C	Cy3 detection probe
miR-16 Cy5FP1	GCCAATATT/Cy5/, T_m = 23.2/24.4 °C	Cy5 detection probe
miR-16 Cy3FP1	/Cy3/GTG CTG CTA/, T_m = 33.4/34.3 °C	Cy3 detection probe
miR-16 inhibitor LNA	CGCCAA+TATTTACG+TGC+TGC+TA, T_m = 66.9/68.2 °C	miR-16 LNA blocker
miR-16 CP block	TAG CAG CAC G, T_m = 34.5/35.3 °C	Detection probe blocker

Note: T_m of FP-target was calculated using IDT OligoAnalyzer having parameters: Target type: RNA, Oligo conc: 0.025 µM, Na^+: 580 mM (4x PBS)/870 mM (6x PBS).

2.3.2 Preparation of Fluorescently Labeled LNA Detection Probe

Oligonucleotide was ordered with terminal amine modification for fluorescent labeling: a let-7a LNA probe complementary to the 5' end, /5AmMC6/+ AC+TAC+CT+CA. The LNA probe was ordered HPLC purified. The oligonucleotide was labeled with *N*-hydroxysuccinimidyl ester derivatives (by amine-NHS ester coupling) of Cy3 (Sigma-Aldrich, GEPA23001) by a 4-hour incubation in Sodium bicarbonate ($NaHCO_3$) and DMSO in the dark, followed by ethanol precipitation and thorough washing with 80% ethanol until the supernatant was colorless (**Figure**

2-2). Denaturing polyacrylamide gel electrophoresis revealed no detectable free dye. Labeling efficiency was quantified by absorbance at 280 nm and 550 nm (Cy3) using a Beckman DU 640B Spectrophotometer.
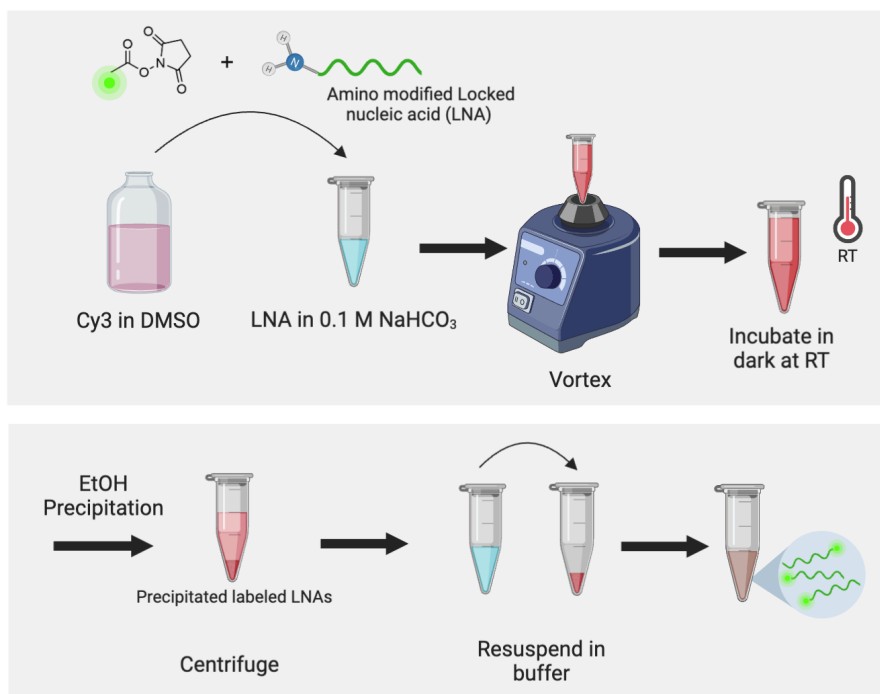
Figure 2-2 Schematic of amino modified LNA coupling with ester of Cy3. Sample is incubated in the dark and ethanol precipitated, washed, and then resuspended in buffer for use. Figure generated using Biorender.

2.3.3 O-TIRF Sample Preparation

Surface Functionalization for *in vitro* Experiments

Prior to an experiment, the imaging surface of the coverslip is first stringently cleaned and functionalized with a 1:10 mixture of biotin-PEG SVA [10 mg] and mPEG SVA [100 mg]. In this protocol, a set of coverslips (No. 1.5, 24×50 mm, VWR no. 48393-241) is first sonicated in acetone for 10 min. This is followed by sonication in 1 M KOH for 10 min to remove aqueous and organic residues from the surface. Next, a "base piranha" solution is prepared which consists of 14.3% v/v of 28-30 wt% NH_4OH and 14.3% v/v of 30-35 wt% H_2O_2. The coverslips are then treated with the piranha solution heated to 60-70 °C for ~30 min. After this incubation is

completed, the piranha is disposed of, and the coverslips are rinsed with water to remove any remaining solution. The coverslips are then functionalized with (3-aminopropyl) triethoxysilane (ATPES), washed and dried under nitrogen flow. The surface amines on the coverslips allow for reaction with *N*-hydroxysuccinimidyl esters of mPEG and biotin-PEG. The coverslips are incubated with the biotin-PEG and m-PEG mixture for ~20 hours. After this, they are further passivated by disulfosuccinimidyl tartrate (DST) to quench the unreacted amine groups. They are rinsed thoroughly with water and dried completely with nitrogen. Coverslips were stored under foil in a nitrogen incubator for up to 4 weeks.

Sample Wells for *in vitro* Experiments

Sample cells were constructed using 20 μL pipet tips (Thermo Fisher Scientific, 02-682-261, low retention). The pipet tips were cut to an ~1 cm length as measured from the wide end of the tips, and the uncut base was adhered to the coated glass coverslip via epoxy resin (Hardman Double/Bubble, Catalog no. 04001) to form (**Figure 2-3**) a cylindrical well.

Figure 2-3 Sample Cell. The coverslip generally has 4 cut pipette tips that are glued with Epoxy to form wells that can hold a 100 μL sample. This design is particularly suitable for O-TIRF microscopy.

Sample Wells *in situ* Experiments

Ibidi μ-Slide 8 Well, Glass Bottom coverslips (Catalog no. NC0704855) were utilized for *in situ* experiments. These coverslips were designed for TIRF, super resolution, and single-molecule applications on fixed or live cells. These μ-slides were sterilized, but not coated. No cleaning or passivation was performed.

2.3.4 Total Internal Reflection Fluorescence Microscopy

In the studies, *in vitro* experiments were mainly carried out using the Oxford Nanoimager (ONI) objective-type TIRF microscope. The ONI is equipped with a $100 \times$ oil-immersion objective (Olympus Plan Apo, NA 1.4) with an XYZ closed-loop piezo stage. Detection probes are excited by a 561-nm and 640-nm laser at TIRF angle of 53°. Fluorescence is detected utilizing a sCMOS camera (ORCA Flash 4, Hamamatsu). Integrated filters were used to split far-red emission onto the right side of the camera and green emission spectra on the left side, enabling FRET and simultaneous dual-color imaging.

For *in situ* experiments, an Olympus IX-81 objective-type TIRF microscope was used for majority of data. The Olympus IX-81 objective-type TIRF microscope is equipped with a 60× oil-immersion objective (APON 60XOTIRF,1.49NA) with both CellTIRF and z-driftcontrol modules as well as a 405 nm (Coherent, 100 mW at source, for imaging DAPI), 561 nm (Coherent ©, 100 mW at source, ~10-20 mW for imaging Cy3 FPs) and 640 nm (Coherent ©, 100 mW at source, ~10-20 mW for imaging Cy5) solid-state lasers. Detection probes were excited in TIRF mode with a calculated penetration depth of ~70-100 nm of the evanescent field using the 561-nm and 640-nm laser. Cy3 excitation was provided by a 561-nm green laser and Cy5 excitation by a 640-nm red diode laser. The indident light intensity was ~10-20 W/cm^2 and detected using a EMCCD camera (IXon 897, Andor, EM gain 50) for fixed cell imaging. The Cy3 and Cy5 emission signals are separated by a dichroic mirror with a cutoff wavelength of 610 nm (Chroma) and projected side-by-side onto an ICCD camera chip (iPentamax HQ Gen III, Roper Scientific, Inc.). The Cy3 channel image was passed through a band pass filter (HQ580/60m, Chroma) and the Cy5 channel was passed through a long pass filter (HQ655LP, Chroma). A Newport ST-UT2 vibration isolation table was used in all experiments utilizing the

Olympus IX-81 microscope. In some experiments, an objective heater (Bioptechs) was used to raise the observation temperature to as high as 36 °C.

2.3.5 *In Vitro* Single-Molecule Detection of miRNA by TIRF

The sample wells constructed from cut pipette tips were used to collect all the *in vitro* data presented in this section. Before imaging, the slide surface was briefly washed with 100 uL T50 buffer (10 mM Tris-HCl, 50 mM NaCl, pH 8.0) followed by the addition of 40 µL of 1 mg/ml streptavidin. After 10 mins of incubation, the excess streptavidin solution was rinsed out by T50 buffer. The surface was then incubated with 40 µL of a solution containing 50 pM of the appropriate biotinylated miRNA in 1× PBS buffer for 10 min. The solution was removed and the excess biotinylated miRNA was rinsed out three times with 100 µL of 1× PBS. Finally, a 100-µl imaging buffer containing 25 nM Cy3 and Cy5 fluorescent probe, 4× or 6× PBS, and an oxygen scavenger system consisting of 5 mM 3,4-dihydroxybenzoic acid, 50 nM protocatechuate 3,4-dioxygenase, and 1 mM Trolox, was added to the sample cell. Transient binding of the Cy5 fluorescent probe via FRET was monitored for 10 min under TIRF illumination by 532-nM laser light with a 250 or 500 ms exposure time (1200 total frames). **Figure 2-4** depicts the process. All oligonucleotide handling was performed in GeneMate low—adhesion tubes.
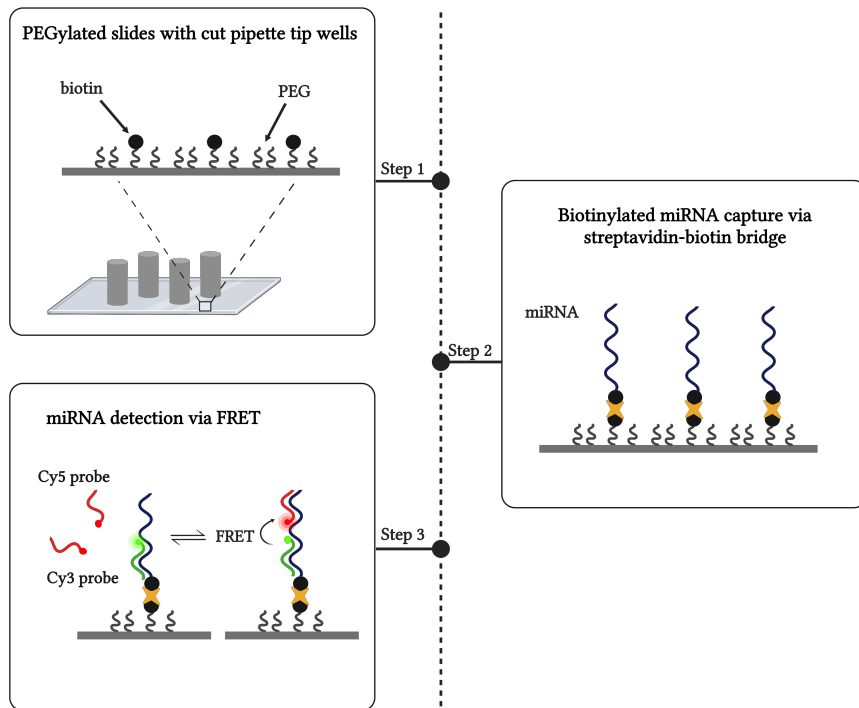
Figure 2-4 Schematic depicting the sample preparation and detection steps for the *in vitro* assay. Step 1: Glue wells onto a PEG coated coverslip. Step 2: The biotin labeled target sample is transferred to the sample wells attached to the coverslip. The target is incubated in the sample wells for 10 min to permit surface capture. Step 3: Single-molecule FRET detection using two FPs: one labeled with Cy3 (FRET donor) the other labeled with Cy5 (FRET acceptor). The Cy3 FP binds to the 5' end of the miRNA, while the Cy5 FPs binds to the 3' end. Since the FRET signal can only be detected when both FPs bind simultaneously to the target, background signal is lowered. Figure generated using Biorender.

2.3.6 Cell Culture & *in situ* Imaging of miRNA

The HeLa cells used in this work were cultured in Dulbecco's modified Eagle's medium (DMEM), high glucose supplemented with 1% Penn/Strep and 10% fetal bovine serum and incubated at 37°C in a humidified atmosphere of 5% CO2/95% air. The cells were seeded in an Ibidi μ-Slide 8 Well coverslip which is suitable for TIRF microscopy. The cells were then fixed with 4% paraformaldehyde in 1× TBS for 15 min at room temperature and washed three times with 1× FBS (**Figure 2-5**). The fixed cells were then immersed in an EDC (0.16 M) solution for

1-2 hours at room temperature for miRNA retention as shown by the Tuschl group [116]. The cells are then permeabilized by a series of 3 min incubation periods in 70-80-99% ethanol and can be imaged or stored in a humidified chamber at 4°C. To image, the fixed cells are incubated with 25 nM Cy3 and Cy5 fluorescent probes in 4×/6× PBS buffer containing the OSS solution. Fluorescence imaging was carried out using the ONI or Olympus O-TIRF. The movies were acquired in the same condition as described in the in vitro detection section.
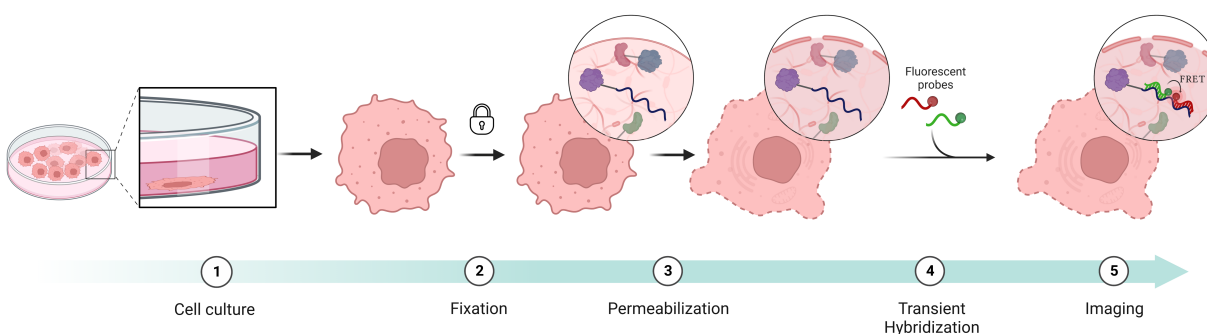
Figure 2-5 Workflow of in situ miRNA detection. Step 1: Culture cells and seed in dish appropriate for fluorescent imaging. Step 2: Fix cells utilizing formaldehyde and EDC. Step 3: Permeabilize cells to allow for probes to enter cell for detection. Step 4: Introduce FRET probes (Cy5 will undergo transient hybridization). Step 5: Image cells on O-TIRF utilizing 532 nm excitation. Figure generated using Biorender.

2.3.7 Analysis of Data

Data Processing of Imaging: Single Channel Analysis

Data were processed by using a MATLAB script to identify areas of high average acceptor intensity within each field of view and generate intensity-versus-time traces from these areas. These traces were then analyzed using a two-state HMM algorithm [117] to generate idealized intensity-versus-time traces to identify transitions between bound and unbound states. Thresholds of a minimum intensity as well as a minimum signal-to-noise (S/N) for the signal were applied to each trace to distinguish genuine transitions from baseline noise. Traces passing the intensity and S/N thresholding were subjected to further kinetic thresholding: number of

binding and dissociating transitions per trace (N_{b+d}), the median bound ($\tau_{on, median}$), and unbound dwell time ($\tau_{off, median}$), and the longest individual dwell times in the bound and unbound states. The manually chosen parameters were used to identify target-bound probes based on their distinct kinetic and intensity behavior and to count the number of accepted counts, or detected target, observed in each FOV. The N_{b+d} histograms were used to evaluate the detector's performance based on the separation from background. The accepted counts were used for quantification and assessment of sensitivity. Further processing included fitting the cumulative frequencies of the bound and unbound dwell time distributions to a single exponential function to obtain the average dwell time in each state. The average dwell times were used to evaluate the probes' ability for distinct and rapid detection.

Data Processing of *in situ* Imaging

Custom MATLAB code was used to identify sites of fluorescent probe binding. To smooth the signal of spots within a cell matrix, an application of blurring or moving window smoothing [118]was performed on cell movies. The blurring filter averages pixel intensities across some number (e.g. 10) of frames, then each of these averaged outputs are averaged altogether. This filtering facilitates identification of individual spots of potential detected single molecules. The next processing step involves utilizing a top hat filter [119], nearest-neighbor filtering, to separate spots from background. The top hat filter utilizes different size regions (e.g. 3 pixels). It will determine the brightest value within this size and compare to the surrounding or "neighbors". If the difference exceeds a certain threshold, then it remains. On the other hand, if it is not exceeded, it is considered background and removed. This filter allows for isolation of objects (single molecules) of images with nonuniform illumination. After spot finding is

achieved, the script finds colocalized molecules. To increase the accuracy of colocalized molecules, a channel mapping is performed. The channel mapping requires taking an image of fluorescent beads that emit fluorescence in both the donor and accepter channel, and then determining the coordinates of the detected spots, in both channels, utilizing a spatial mapping algorithm. This allows for the colocalization or mapping of the individual spots from both the donor and acceptor channel. After channel mapping, the script generates FRET intensity-vs-time traces. The traces were analyzed manually to corroborate the anticorrelation typical of FRET. After verification of FRET detection in fixed cells, the data was then processed utilizing the SiMREPS MATLAB code. Each movie collected with two channels was separated into individual channels via ImageJ. The acceptor channel then was processed utilizing the single channel analysis described above to quantify molecules detected.

2.4 Results and Discussion[3]

SiMREPS was initially developed for the detection of nucleic acid biomarkers. The classical SiMREPS schematic was established for evaluating four human miRNAs that are dysregulated in cancer and other diseases, *hsa-let-7a*, *hsa-miR-21*, *hsa-miR-16* and *hsa-miR-141* [120–122]. Since then, SiMREPS has extended into detection of DNA mutations, proteins, and small molecules [67,99]. Recently, it has extended from a surface-tethered technique into being capable of detection *in situ* [101]. However, this method for *in situ* detection was achieved by utilizing a single short 10 nt detector probe conjugated with a nanoparticle exhibiting high brightness. They showed detection of miR-21 which exhibited low counts per cell (30-300). At elevated expression of miRNA, the high brightness will pose a problem as signal will overlap,

---

[3] Project was conceived by K.M. Some experiments were performed with L.L. including data shown in Figure 2-9 – Figure 2-11, Figure 2-14, Figure 2-21. All data visualization presented were produced by K.M.

making it difficult to distinguish between single molecules. Additionally, the detection scheme differs from the original SiMREPS assay which utilizes two probes, a capture and detector probe. This motivated the development of a different detection strategy utilizing FRET probes, in which the acceptor exhibits a kinetic fingerprint for detection. Using two probes instead of one, not only results in an increase of specificity, but will function at detecting both low and high intracellular concentrations of miRNAs since the acceptor probe will only be detected in presence of the donor probe.

Here, we focused on the improvement of the *in situ* detection assay described in Li et. al. Like the classical SIMREPS methodology, two probes would be employed to enhance specificity. The previous methodology included designing a sequence-specific capture probe with a biotin tag to be immobilized on a streptavidin coated coverslip. To ensure a strong target capture binding, LNAs were utilized given their characteristic of increased affinity. With respect to the read-out FP, a different design was employed. Since we are interested in reversible, repeated binding, the T_m of the interaction between the FP and the target should coincide with the assay temperature. Contrary to classical SiMREPS target immobilization, the miRNA targets are held in space within a cellular matrix. Formaldehyde, a small, cell permeable crosslinker covalently links proteins to nucleic acids and other proteins when they exist in close proximity [123]. To this end, a new design capable of "capturing" single miRNA molecules in space was necessary.

To begin testing the functionality of a set of FRET probes, the classical SiMREPS assay could not be used since it requires capturing the miRNA target via complementarity and therefore would impede the binding of one of the probes. This would only permit the

investigation of one probe. To be able to evaluate the donor probe as well as the combination of the acceptor and donor probe, a new strategy was employed.
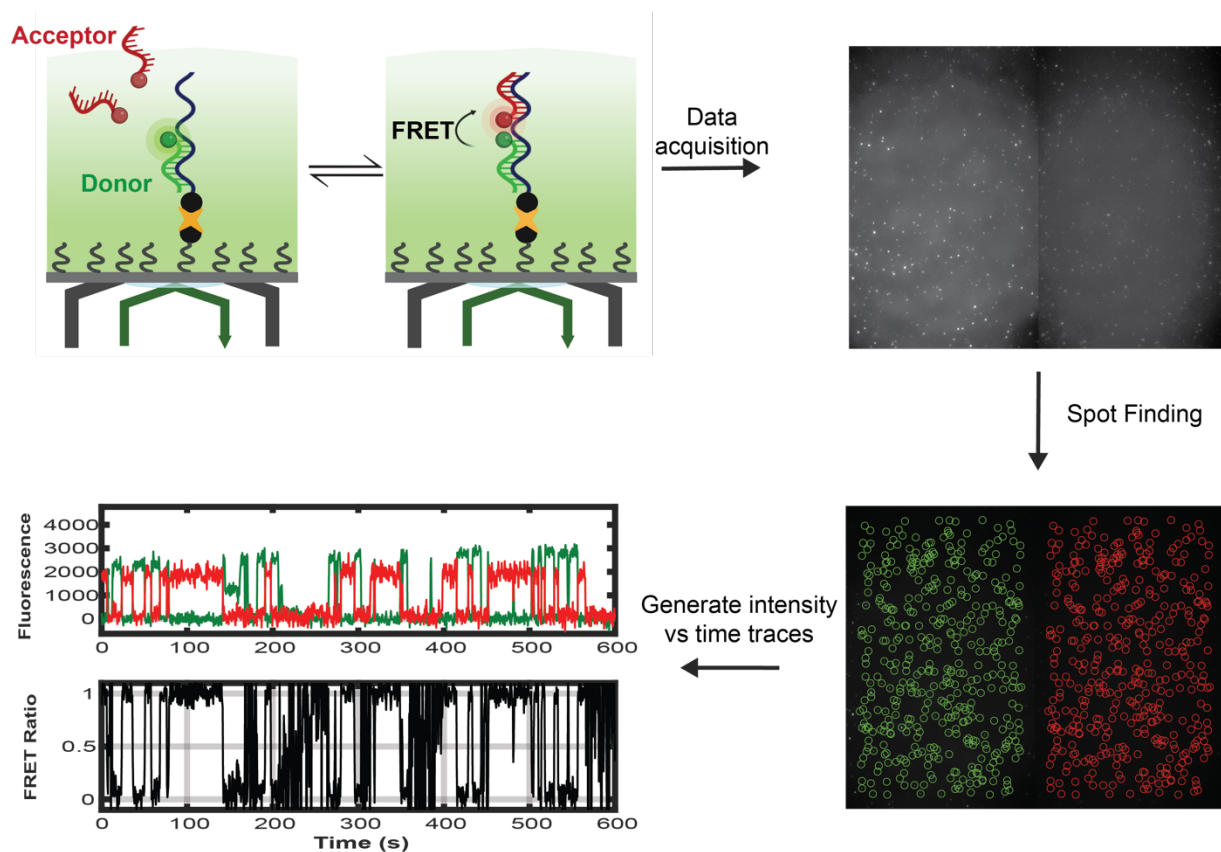
Figure 2-6 Schematic of FRET probe detection and data acquisition and processing to obtain single molecule kinetic fingerprints. The Cy3-labeled donor probe transfers energy to the Cy5-labeled probe which interacts transiently and reversibly with the target and generates a single molecule kinetic fingerprint recorded by a TIRF microscope (Created using Biorender). A representative field of view (top right corner) from TIRF microscopy analyzed with MATLAB programs to identify spots with potential smFRET signals in that field of view (bottom right corner). Intensity vs time FRET traces are generated for colocalized spots (bottom left).

An *in vitro* assay, as depicted in **Figure 2-6**, was designed to evaluate the detection utilizing this new approach. The assay uses a tethered miRNA target to the surface and then generates a FRET signal when the acceptor probe is aligned with the donor probe. Just like with classical SiMREPS, emission of the Cy5 FP emission is recorded by a TIRF microscope. However, the analysis included verification of FRET instances via raw single molecule time traces showing anti-correlated donor and acceptor intensities. After verification, we employed the classical SiMREPSs analysis software (refer to **Section 1.6.2**) for the evaluation of the red

channel to identify the targets via kinetic fingerprinting. Following the optimization of the FRET probe pairs, an introduction into fixed cells was conducted.

This new design and extension of the SiMREPS platform toward application *in situ* will expand the scope of miRNA detection by offering quantification as well as conservation of the spatial distribution of miRNAs in a cell. First, quantification is important to ensure miRNA as reliable diagnostic biomarkers. Second, conserving the spatial distribution of miRNAs contains valuable diagnostic as well as biological information to further understand their role in regulatory pathways. This approach also overcomes other limitations since it does not require cell lysis and RNA extraction which may potentially result in RNA low and/or degradation. Overall, I hypothesize that employing this FRET-based SiMREPS will achieve higher specificity while continuing to diminish background and allow for faster analysis in comparison to traditional FISH. The following sections will describe the rationale behind the design and the proof-of-concept demonstrating the ability to detect miRNA *in situ*.

2.4.1 Design and Optimization of FRET-based Probes

The first FRET-based probes were designed for let-7a detection, a miRNA involved in tumor suppression [124–126]. The donor probe, analogous to the CP, was designed to have a higher melting temperature (T_m, 28°C) for a stronger and more stable interaction to the target, while still binding reversibly to avoid potential photobleaching. The acceptor fluorescence probe, also referred to as the read-out probe or FP, was designed to have a T_m closer to room temperature (20°C) to allow for binding and dissociation to occur frequently so that a kinetic fingerprint could be readily generated. To select potential probes, an IDT-provided online tool was utilized to estimate melting temperatures (refer to **Table 2-1**). For initial optimization, let-7a Cy5 FP1, let-7a Cy5 FP2, and let-7a Cy3 FP1were investigated with the biotinylated, directly

surface attached miRNA (**Figure 2-7**). We also labeled an LNA strand (same sequence as the

Cy3 donor probe) to validate the efficiency of the FRET setup as well as to mimic the classical

SiMREPS strategy which will be thoroughly described below.
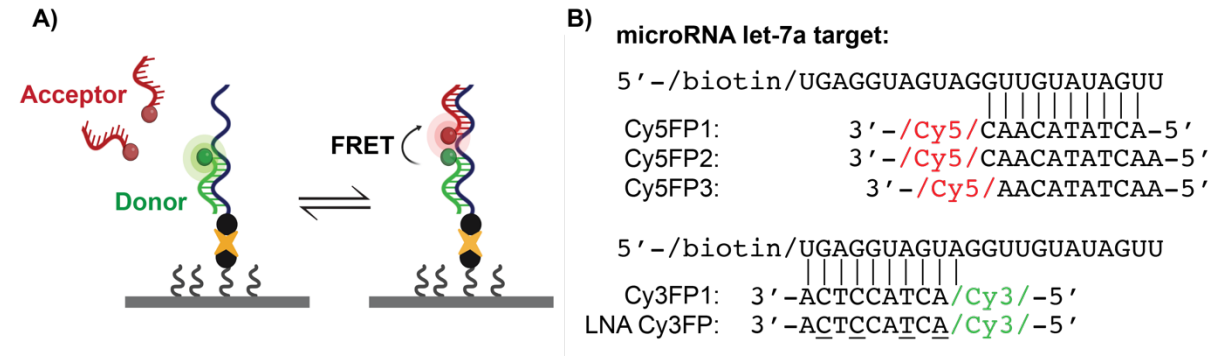
Figure 2-7 MicroRNA detection schematic (a) Probe pair exhibits FRET when both donor and acceptor probe bind to target (Created using Biorender). (b) Fluorescent probe design for let-7a detection. Fluorescent probe sequences have various complementary binding with respect to let-7a.

To evaluate the integrity and assembly of the schematic, denaturing and non-denaturing

polyacrylamide gel were run with lanes for each individual strand of read-out probes, let-7a, and

supplementary strands and/or probes. As seen in (**Figure 2-8**), the let-7a and fluorescent probes

with the exception of LNA labeled strands, are intact. With respect to the lack of bands for let-7a

LNA and let-7a LNA Cy3, it is hypothesized that the SYBR Gold stain is not able to intercalate

in LNA as it can for DNA due to the O2′,C4′-methylene bridge [127].
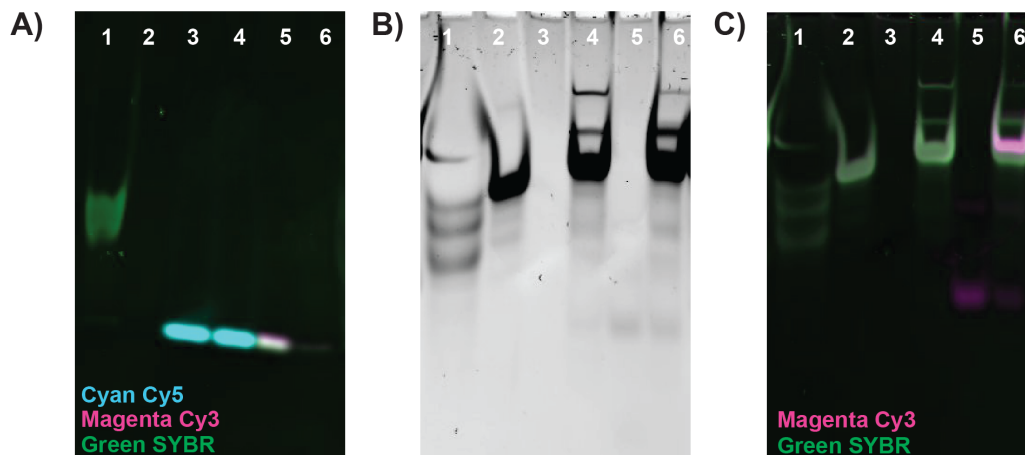
Figure 2-8 Non-denaturing and denaturing gels for probes utilized in the assay. A) 20% denaturing polyacrylamide-urea gel stained with SYBR Gold. Lane 1: biotin let-7a, Lane 2: let-7a LNA, Lane 3: let-7a Cy5FP2, Lane 4: let-7a

Cy5FP1, Lane 5: let-7a Cy3FP1, Lane 6: let-7a Cy3 LNA Cy3 B) 20% non-denaturing polyacrylamide gel stained with SYBR Gold. Lane 1: miRNA ladder (25 nt, 21 nt, 17 nt), Lane 2: let-7a, Lane 3: let-7a LNA, Lane 4: let-7a + LNA, Lane 5: let-7a LNA Cy3 LNA, Lane 6: let-7a + Cy3 LNA C) Gel shown in panel B, illuminated for Cy3 detection.

To further investigate the successful assembly of the schematic and detection approach, a SiMREPS-like assay was designed. The target could not be captured by the traditional setup utilizing a LNA CP, otherwise it would block off the complementary area to the Cy3 FP making FRET difficult to achieve. Instead, a biotinylated target was employed which allows evaluation of both Cy3 (LNA and non-LNA) and Cy5 probes as well as mimic the cross-linked miRNA in a cell (**Figure 2-7**A).

Initial testing of probe behavior would require immobilization of the target at a suitable density on the surface to be able to differentiate between different single molecules in order to allow for the extraction of kinetics. Different concentrations of biotinylated target, including 0 pM, 10 pM and 50 pM were initially tested. The density of each corresponding concentration of biotinylated target can be seen in **Figure 2-9** via Cy5 acceptor signal readout. The Cy5FP2 was chosen to obtain the readout. From this experiment, we were able to observe repetitive binding as hypothesized and deduced 50 pM target was an appropriate density as it would allow us to examine around 500 individual traces from which to extract kinetic information.

Biotin-PEG/mPEG 1:10
1 mg/mL STV
0 pM biotin let-7a

Biotin-PEG/mPEG 1:10
1 mg/mL STV
10 pM biotin let-7a

Biotin-PEG/mPEG 1:10
1 mg/mL STV
50 pM biotin let-7a
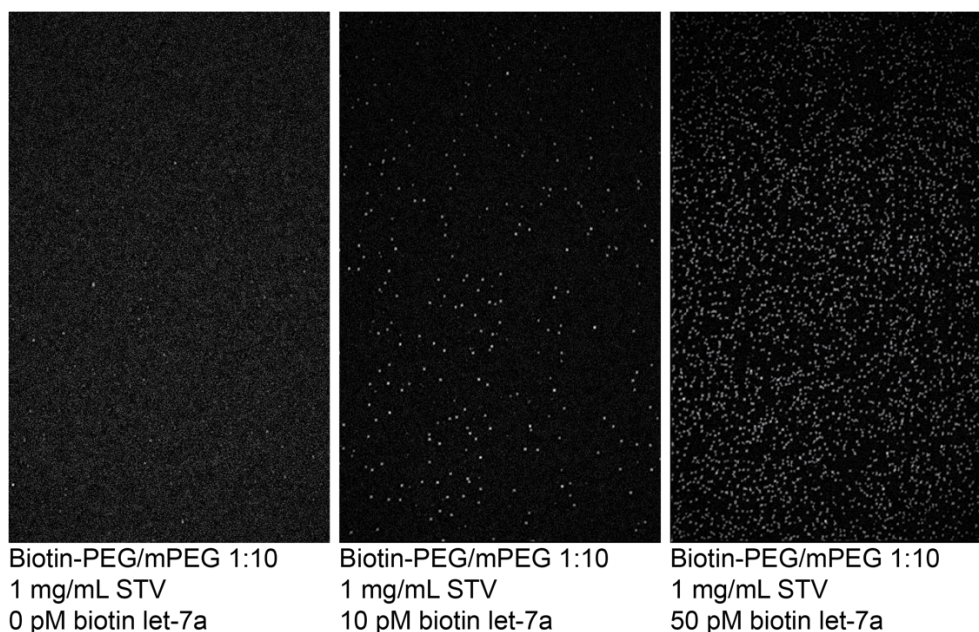
Figure 2-9 Comparison of spot density of captured and detected potential let-7a target molecules with increasing target concentration from 0-50 pM biotinylated let-7a target sample. The images presented, called intensity fluctuation map, were obtained after the first step of SiMREPS data analysis where the average absolute frame-to-frame change in intensity at each pixel was determined. The bright spots represent the binding and dissociation of the fluorescent probes at each location.

In parallel, we tested the behavior of the non-LNA FPs individually, utilizing standard SiMREPS conditions, and found all probes bound to the target and exhibited a varying set of kinetic fingerprints (**Figure 2-10**). As hypothesized based on estimated melting temperatures, the Cy5 FP has a shorter $\bar{\tau}_{on}$ (**Figure 2-10A**), indicative of a more transient interaction, in order to achieve the kinetic fingerprint read-out while the Cy3 FP has a more stable interaction as seen by the longer τ_{on} in the traces (**Figure 2-10B**).
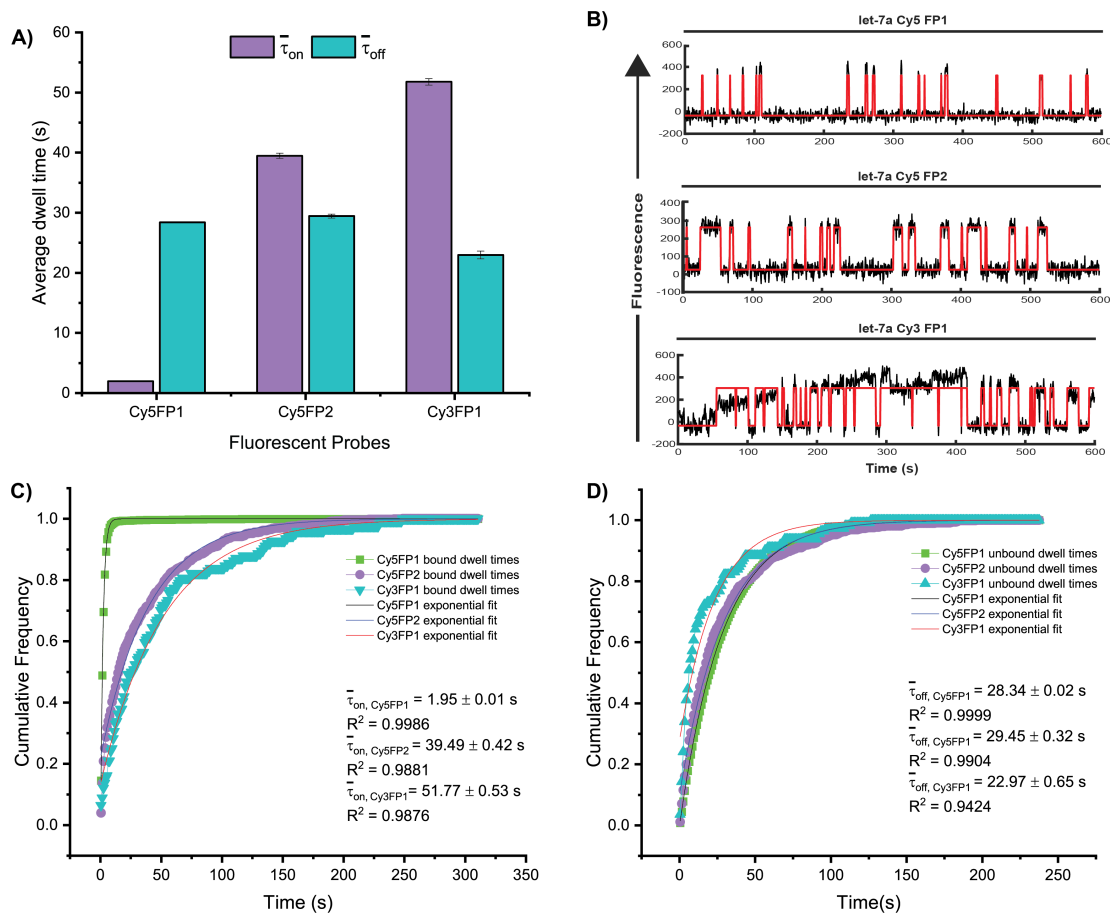
Figure 2-10 Individual assessment of potential FRET probes for let-7a detection. A) The average dwell times of the interactions of each corresponding probe to the let-7a target. B) Representative single molecule kinetic traces of each corresponding fluorescent probe. Traces fitted with HMM were utilized to extract the dwell times of FP bound and unbound states. (C-D) Single exponential fitting of dwell time cumulative frequency for let-7a target bound ($\bar{\tau}_{on}$) and non-target-bound ($\bar{\tau}_{off}$) states for each corresponding FP. All experiments were performed in standard imaging conditions: [FP] = 25 nM, [Na$^+$] = 580 nM. (4× PBS). The time (t1) listed reflects the dwell time calculated from the fitted curve using all accepted traces.

Although both Cy5FPs exhibited a transient interaction, the Cy5FP1 exhibited a lower τ_{on} which could potentially lead to issues in detection since the Cy3FP1 unbinds from the target. We found that Cy5FP1 $\bar{\tau}_{on}$ was significantly lower than the Cy3FP1 $\bar{\tau}_{off}$, meaning there could be instances where the Cy5FP1 could bind, but not be detected since the donor is not replenished fast enough and would not be present for energy transfer. To alleviate this potential issue, we focused on further optimization of the probes. On the one hand, it was necessary to increase the $\bar{\tau}_{on}$ of the Cy5FP1 as this can pose a problem is the time becomes as short as the camera

integration time. On the other hand, the Cy3FP1 $\bar{\tau}_{\text{off}}$ should be decreased to ensure the energy transfer for detection. One avenue to explore was an increase in FP concentration, to have them rebind faster. However, the increase in concentration could later affect our S/N in a cellular matrix so we opted to attempt a different avenue. To ensure an increase in the bound state (decrease in the unbound state), we tested a change in salt conditions. Ionic strength is an important parameter to optimize to obtain optimal FP kinetics. Given that the negatively charged phosphates tend to repel each other as well as the negative charges on the opposite strand of a DNA duplex, an increase in cation concentration in the buffer stabilizes DNA duplexes by shielding electrostatic repulsion between the opposing strands, stabilizing the duplex. SiMREPS typically uses a buffer of high ionic strength (e.g., 4 × PBS) to obtain rapid kinetics of binding of the FP to the target. Given the unique situation with the FPs, we increased the salt concentration from 4× to 6× PBS. In the presence of higher salt, we did not find a significant difference in the $\bar{\tau}_{\text{on}}$ for the Cy5FP1 (**Figure 2-11**). The lack of increase in average bound time could be explained by the slight temperature fluctuation (1-2 °C) experienced while imaging. Considering the initial issue of a low $\bar{\tau}_{\text{on}}$ and the drastic effect seen with a slight change in temperature, Cy5FP1 may not be a suitable choice of probe. The Cy5FP2, on the contrary, showed an increase in $\bar{\tau}_{\text{on}}$ when it was in a higher salt environment (**Figure 2-11**). From these data, we decided to continue pursuing the Cy5FP2 and withdrawing the Cy5FP1 as a potential FRET probe candidate due to the low $\bar{\tau}_{\text{on}}$ making it difficult to manipulate kinetics further.
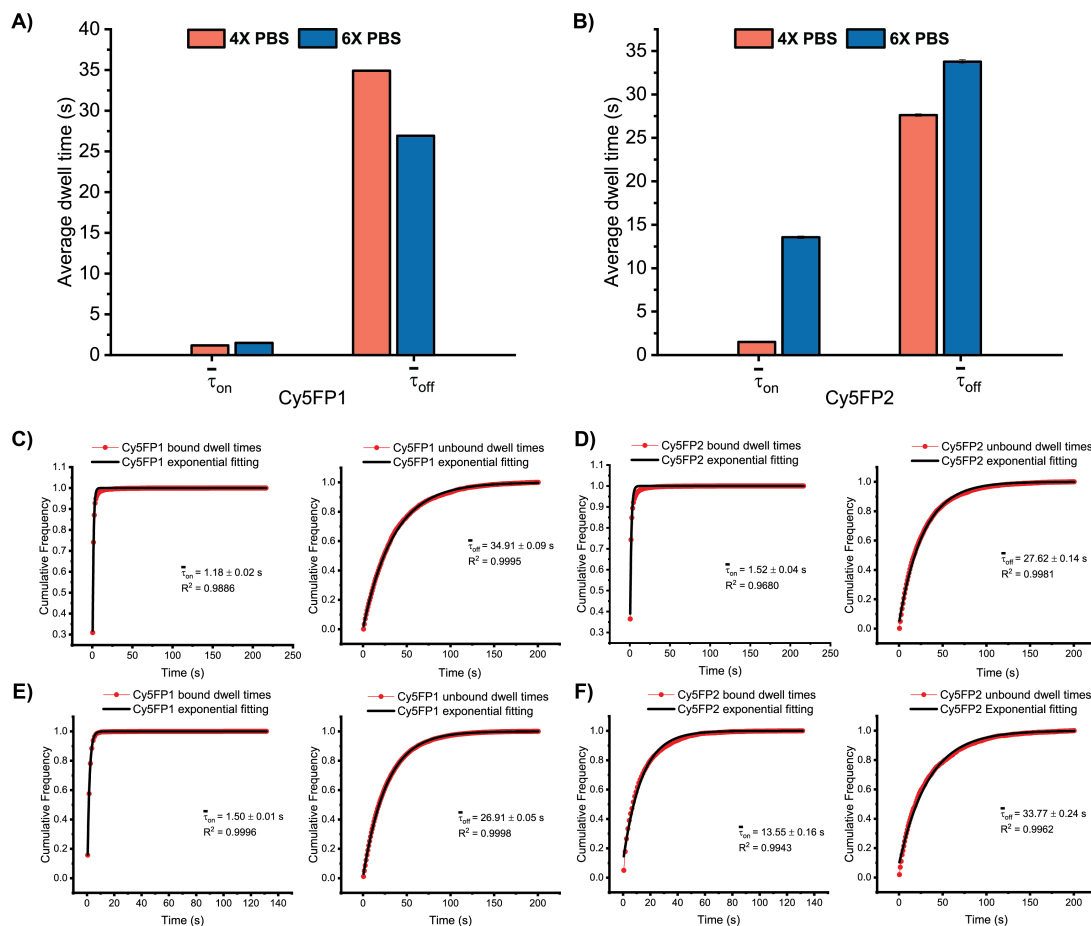
Figure 2-11 Optimization of the Cy5 FRET FPs for let-7a detection. A) The average dwell times ($\bar{\tau}_{on}$ and $\bar{\tau}_{off}$) of the interactions of Cy5FP1 to the let-7a target. B) The average dwell times for Cy5FP2 target bound ($\bar{\tau}_{on}$) and non-target-bound ($\bar{\tau}_{off}$). (C-F) Exponential fitting of dwell time cumulative frequency for Cy5FPs target bound and non-target-bound states for each corresponding FP. Experiments were performed in two different salt concentrations (C-D) [Na$^+$] = 580 nM (4× PBS) and (E-F) [Na$^+$] = 870 nM (6× PBS).

Moving forward, we investigated the Cy5FP2 and Cy3FP1 individually. Each FP was analyzed across temperatures including 22 °C, 24 °C, 26 °C, and 28 °C. This set of experiments was aimed to narrow down a set of parameters that would allow us to achieve the desired kinetics of a transient Cy5 FP and more stably binding Cy3 FP. For let-7a Cy5FP2, we were able to obtain a higher N_{b+d} as the temperature increased (**Figure 2-12**). Additionally, we noted a decrease in the $\bar{\tau}_{on}$ from about 35 sec to 10 sec (**Figure 2-13A)** while the $\bar{\tau}_{off}$ slightly decreased (**Figure 2-13B)** leading to the kinetic fingerprints shown in **Figure 2-12B**. At temperature 22 °C, let-7a Cy3FP1 exhibited high stability with an $\bar{\tau}_{on}$ around 35 sec (**Figure 2-13C)**. At

temperatures 22 °C and 24 °C, the fluorescent probe exhibited different $\bar{\tau}_{off}$ behaviors. Single exponential fitting did not describe the data appropriately which prompted a double exponential fitting. The cumulative frequency for the Cy3FP1 non-target-bound states were fit with a double exponential function.

$$y = A_1 e^{-x/\tau_1} + A_2 e^{-x/\tau_2} + c$$

The coefficients A_1 and A_2 provide the weight of their population of molecules. The coefficients τ_1 and τ_2 describe the average dwell times for shorter- and longer-lived populations, respectively. From this analysis, we observed a decrease in the Cy3FP1 $\bar{\tau}_{off}$, however it should not pose a problem as it was lower than the average bound time of the Cy5FP2 (**Figure 2-13D**).

Overall, it was deduced that an optimal temperature to perform subsequent experiments was 28 °C. At 28 °C, we could observe a higher N_{b+d} for Cy5FP2 which could lead to a lower acquisition time while we still maintained a stable Cy3FP1 that would have instances of being unbound which would lower potential photobleaching of the probe.
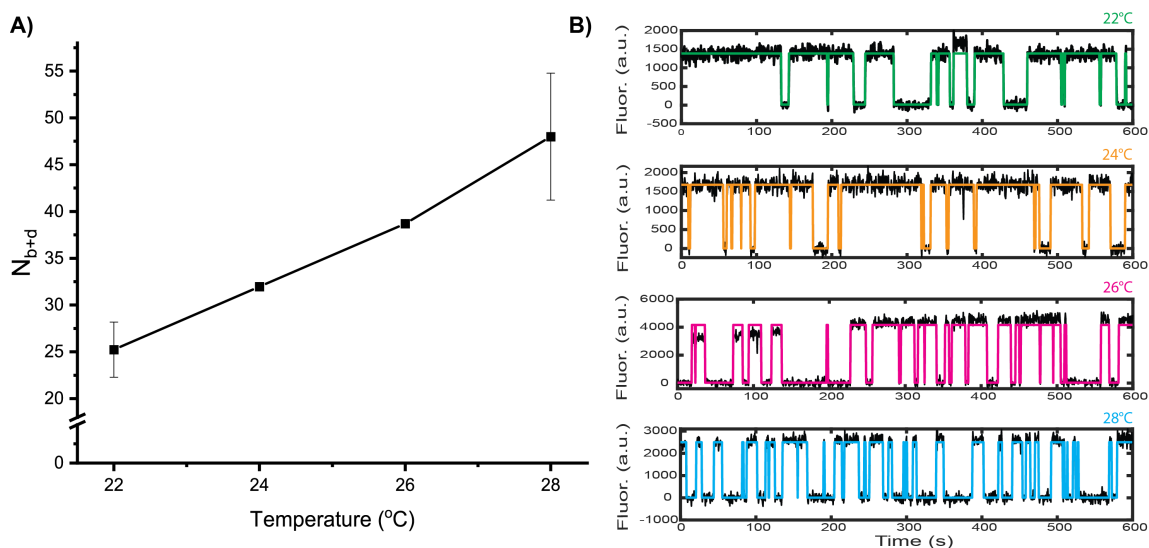
Figure 2-12 Optimization of detection condition for rapid imaging for Cy5FP2 to facilitate data collection. (a) Effect of imaging temperature on the number of binding and dissociation events of Cy5FP2. The error bars represent one standard deviation across the N_{b+d} average extraces from all accepted traces analyzed under each temperature

55

condition. The concentration Cy5 FP used in the imaging buffer was 25 nM for all. (b) Representative kinetic fingerprint for detecting let-7a at each corresponding temperature. Error bars represent the standard deviation of two independent experiments.
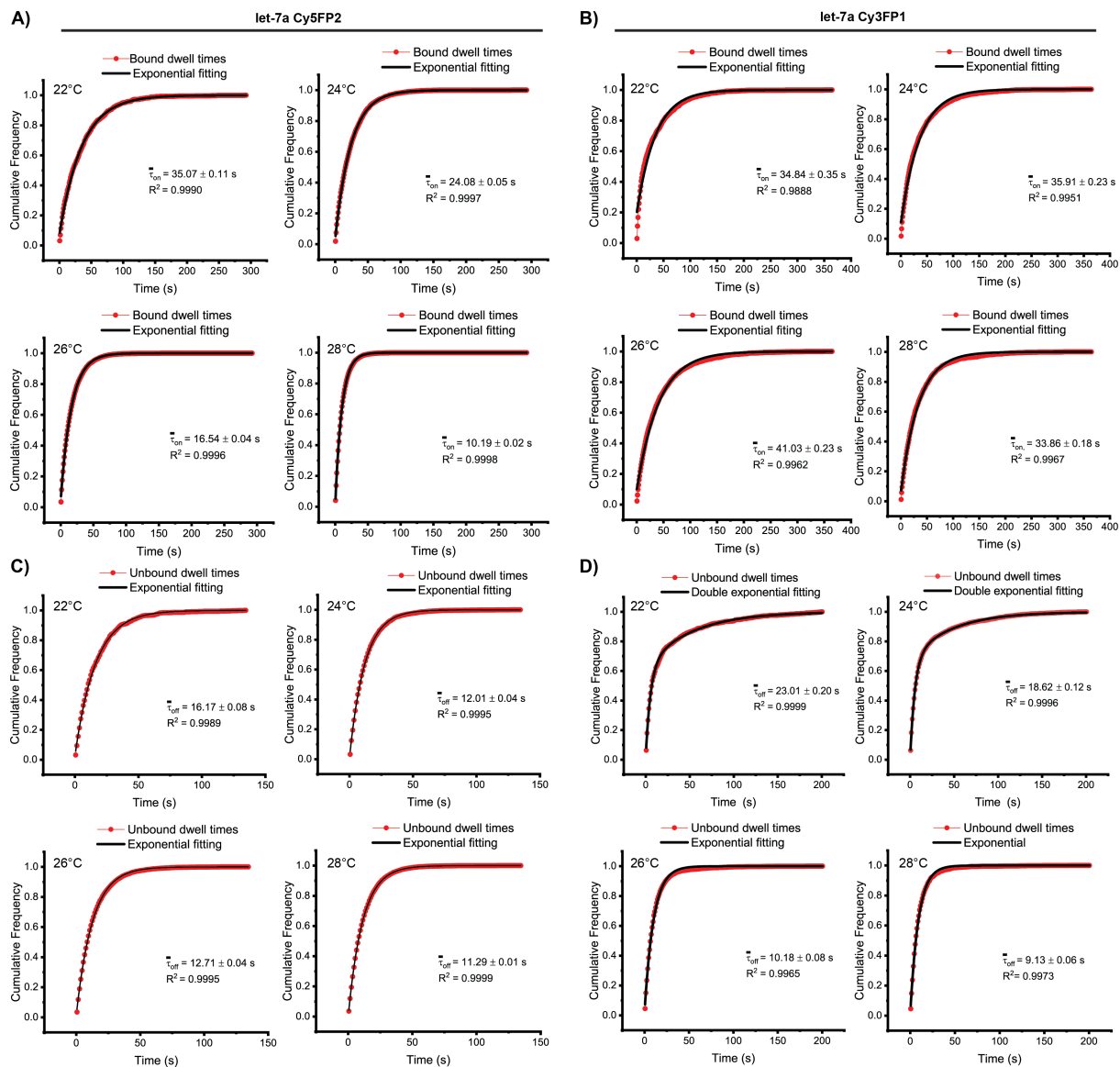
Figure 2-13 Exponential fitting to dwell time cumulative frequency for A) Cy5FP2 target bound and C) unbound states. Estimation of average dwell times of the B) bound and D) unbound state for Cy3FP1. The times listed reflect the average dwell time calculated from single exponential fitting, unless otherwise noted, for all accepted traces.

2.4.2 *In vitro* FRET Detection

As previously mentioned, the final goal is to utilize FRET as the detection method vs direct excitation in order to transfer the SiMREPs capabilities to an *in situ* application. Before moving into FRET detection *in vitro*, we hypothesized a potential issue with the fluorophore

56

labeling that had not been considered before. Both Cy3 and Cy5 have been shown to stack on the end of double-stranded DNA, similar to an additional base pair [128,129]. The affinity seems to be driven by π-stacking interactions with the nucleobases and restricts the rotational isomerization of the dyes and increases their fluorescence [130]. Additionally, the SiMREPs assay functions well due to the constant replenishment of FP to the target which also helps reduce issues arising from photobleaching. Considering the Cy5FP2 is labeled at the 3' end and the Cy3FP1 probe is labeled at the 5' end, photobleaching may occur making it difficult to detect FRET. This stacking effect could also disturb the functionality of the SiMREPS assay since the probes cannot be replenished. To this end we included the analysis of another Cy5 probe labeled at the 5' end (will be referred to as 5'Cy5FP).

That being the case, we began to investigate LNA Cy3 with the two Cy5 FPs. The LNA Cy3 probe was utilized for the following reasons 1) LNA Cy3 would behave similar to the LNA capture probe in the classical setup and 2) the Cy3 fluorophore on the probe would serve as the excitation source for the Cy5 FP. This assay design was tested to avoid potential issues by having too many "moving parts" and to ensure FRET was, indeed, possible. From these initial experiments, we found that both Cy5FP2 and 5'Cy5FP were capable of undergoing FRET with LNA Cy3 FP and 5'Cy5FP showed a higher sensitivity in detection (**Figure 2-14**). Although the Cy5FP2 had lower accepted counts, it was still detected showing that photobleaching did not occur despite our hypothesis.
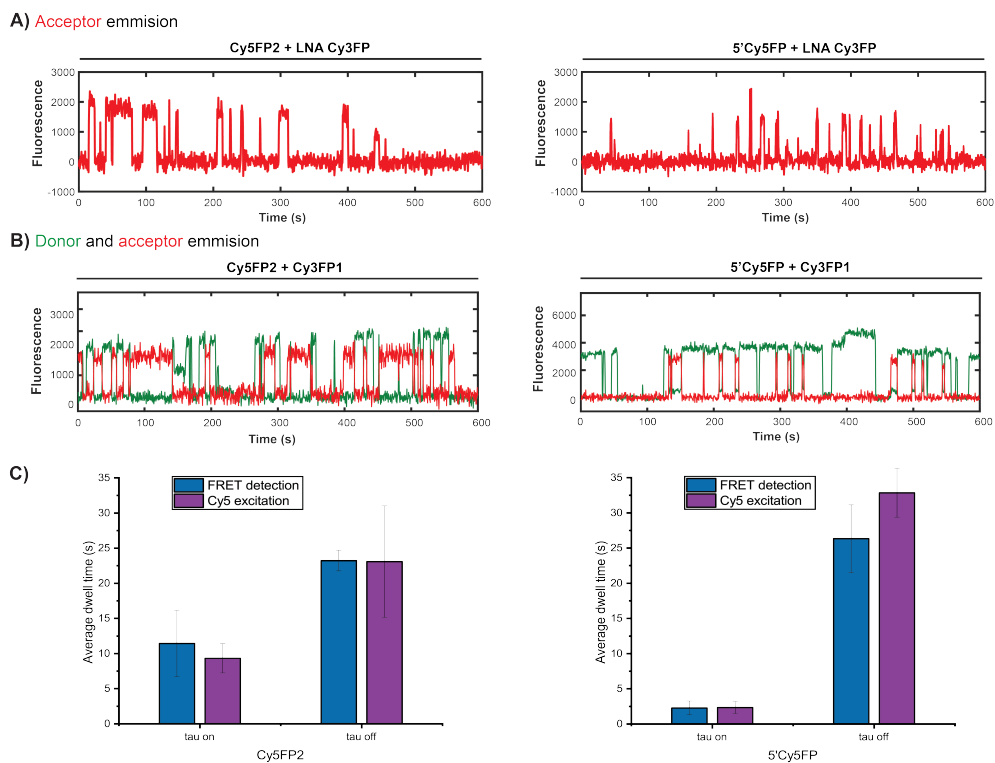
Figure 2-14 Investigation of detection of let-7a utilizing a non-reversible LNA donor probe. A) Kinetic fingerprints extracted from the acceptor channel, utilizing donor excitation for two Cy5FPs. B) FRET traces for each corresponding Cy5FP in presence of a stable, but reversible Cy3 FP donor. C) Average dwell times extracted from Cy5FP2 (left) and 5'Cy5FP (right) when detected via Cy3 donor excitation (532 nm) vs direct Cy5 FP excitation (640 nm).

The next step was to test whether the probes would work with Cy3FP1. Again, both probes were able to detect let-7a, however, the 5'Cy5FP did not exhibit FRET as efficiently with the Cy3FP1 as seen with the LNA Cy3FP (**Figure 2-14B**). In contrast, Cy5FP2 and Cy3FP1 had efficient FRET (**Figure 2-14B**). We further investigated the issue that arose with the 5' labeled fluorescent probes further and found that the average bound time was similar to the Cy5FP1 which was withdrawn as a candidate. The low $\bar{\tau}_{on}$ in comparison with the higher $\bar{\tau}_{off}$ of Cy3FP1 appears to be reducing the possibility of detection. Due to the kinetic analysis, the 5'Cy5FP was unfit to function as a FRET probe and the Cy5FP2 was selected for further optimization because of its successful application in FRET-based detection (**Figure 2-15**).
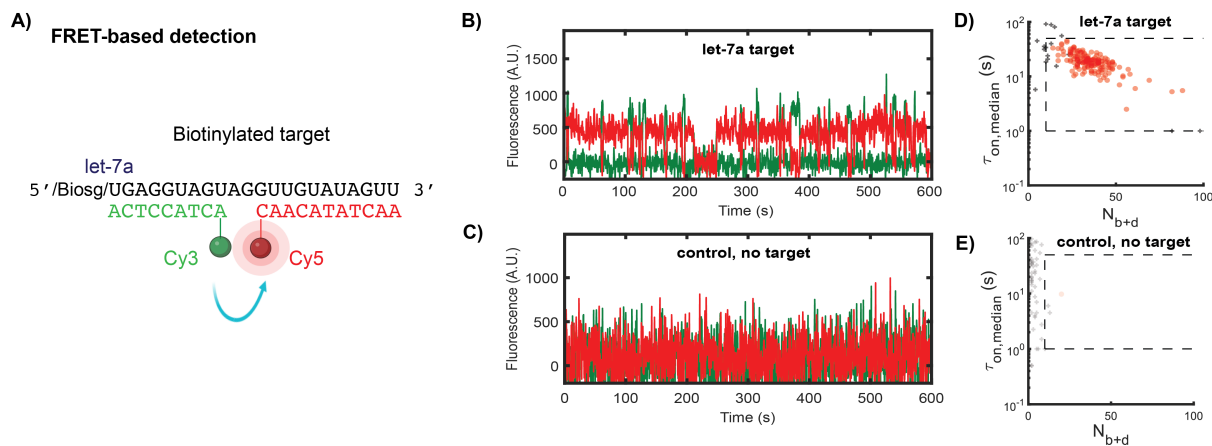
Figure 2-15 A) Schematic depicting the detection of let-7a with optimized FRET probes. B) Representative kinetic fingerprint for detecting let-7a target in a 10 min movie using 25 nM Cy3 FP and 25 nM Cy5 FP. B) Representative FRET trace from a control sample in the absence of the target. D-E) Scatterplot of N_{b+d} and $tau_{on,median}$ for all the trace generated from samples in the presence D) or absence E) of let-7a. Dashed lines indicate the threshold for accepting a trace as a positive count for single molecule miRNA detection.

For the next optimization, we began to focus on decreasing the acquisition time by adjusting the FP concentration and temperature. The FRET pair probes were studied at 4 different concentrations: 25 nM, 50 nM, 75 nM, and 100 nM, and temperatures 28 °C, 30 °C, 32 °C, 34 °C and 36 °C (Data can be found in **Appendix Figure 1**, **Appendix Figure 2**). The increase in temperature looked promising due to the increase in N_{b+d} as seen for the single Cy5FP2 optimization. However, we did not pursue this immediately in fixed cells considering the change in environment may have an effect on the kinetic fingerprints of the FPs observed *in vitro*. Our rationale was to first test our FRET pair probes in 6× PBS at 28 °C and after establishing detection, we would apply our temperature findings as appropriate. Additionally for the change in concentration, we also noted an increase in binding and unbinding events, however, we decided not to pursue this route due to the overall effect that may arise when transferring these parameters into *in situ* imaging. We hypothesized the increase of fluorescent probe utilized may introduce more background which could complicate detection and since 25

nM FP could be used detect target in vitro, we began the evaluation of the assay *in situ* with that concentration.

Another form of development was to ensure the specificity of our probes. To ensure we were, in fact, observing a specific detection of let-7a, as a negative control a different miRNA was probed under similar conditions with the let-7a probes. As seen in the **Figure 2-16**, there is high specificity for let-7a, further confirming the potential to extend SiMREPS into an *in situ* setting. Also, it further supports the specificity of probes to let-7a vs another miRNA in addition to the specificity already seen in comparison to its family member, let-7c [97].
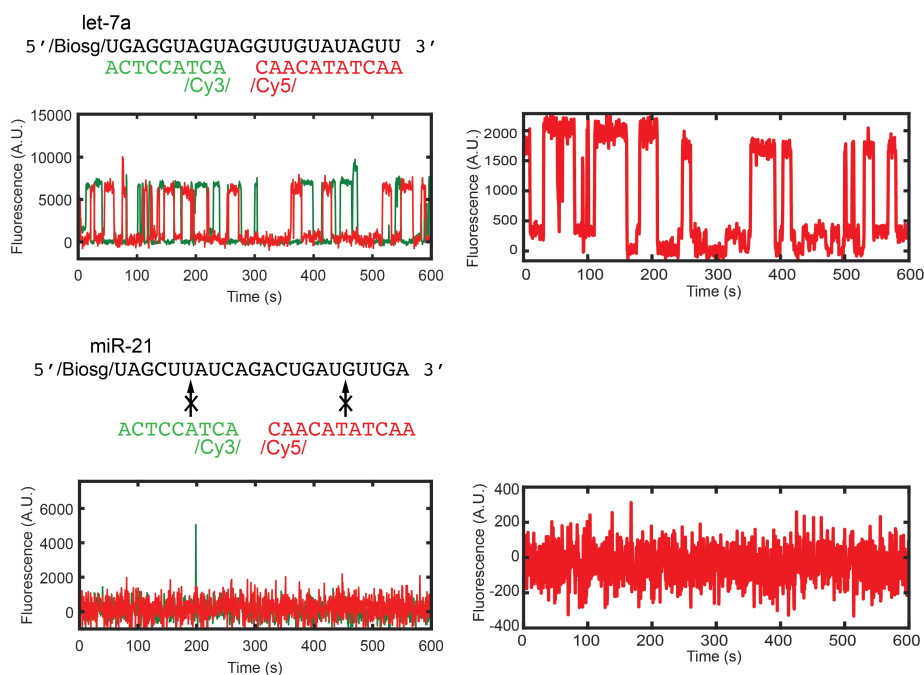
Figure 2-16 Specificity of let-7a detection vs miR-21. The fluorescent probes for let-7a exhibit FRET (top left) and can be detected by analyzing only the acceptor channel (top right). Single molecule traces for miR-21 detection exhibit no FRET and no transient binding was found when investigating the acceptor channel.

2.4.3 miR-16 and miR-21 FRET Probe Detection

Following the completion of let-7a probe design and optimization, we began to expand our biomarkers of detection. We decided to focus on designing and optimizing probes for miR-16 and miR-21, in parallel. Given our knowledge of our optimal FRET probe design for let-7a,

we selected Cy5 probes with a melting temperature close to 20°C (between 18-23°C) and Cy3 probes >30°C (between 28-35°C, see).
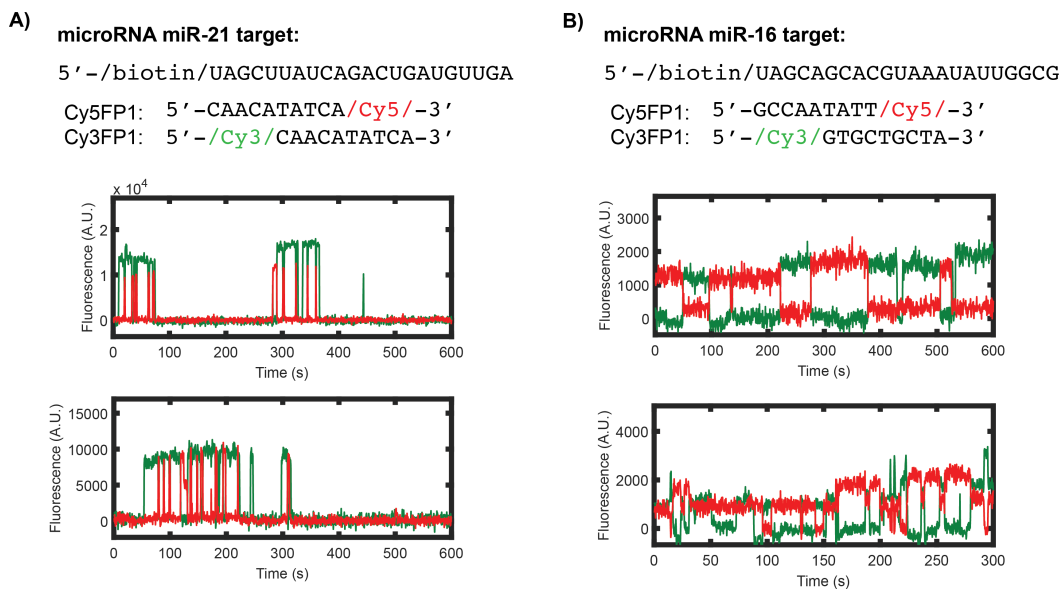
Figure 2-17 Validation of functionality of FRET probe design for A) miR-21 and B) miR-16.

We began testing for FRET given the successful data acquired for let-7a as well as individual probe behaviors simultaneously. As shown in **Figure 2-17**, detection of miR-21 in standard conditions (25 nM FP, 4× PBS, 21°C) led to success, however, there were long unbound states between FRET instances. Contrary to the let-7a FPs, the average dwell times were considerably different **(Figure 2-18B,C)**. Particularily, for the miR-21 Cy3FP1, the $\bar{\tau}_{\text{off}}$ was 61 seconds in comparison to 34 seconds exhibited by the let-7a Cy3FP1. We speculated that perhaps the Cy3 FP has a stronger binding interaction than predicted. This hypothesis could support potential photobleaching which would reduce the detection of the Cy5FP as seen by the FRET traces in **Figure 2-17A**. The Cy5FP1, on the other hand, is exhibiting the desired transiently binding behavior. Additionally, it is of interest to note that the Cy5FP1 is dissociating very fast as seen by the short binding in the traces presented and the calculated $\bar{\tau}_{\text{on}}$ **Figure 2-18A)**. To better resolve the interaction of Cy5FP1 and the target, we decided to reduce our

exposure time from 500 ms to 250 ms. Even so, a higher temperature may be required to tackle the potential strong binding exhibited by the Cy3FP which could interfere with Cy5FP1 detection. For that reason, we investigated a potential replacement of Cy5FP1 by a more stable FP (Cy5FP2) in order to open up more opportunity for optimization if needed. This new design would allow for investigating of temperature increases or introduction of formamide. The Cy5FP2 was investigated alone and in comparison to the Cy5FP1, it had a $\bar{\tau}_{on}$ of ~20 seconds vs ~2 seconds calculate for Cy5FP1. In addition, we set out to investigate the bottleneck posed by the Cy3FP. First, a UV-Vis test was performed to gather information on the FPs labeling efficiency. From this, we discovered that the Cy3FP had a labeling ratio 1.03 dye per nucleic acid (see **Appendix Figure 4**). Following this, we tested an increase in Cy3FP1 to examine the behavior of the probe and assess our theory of potential photobleaching (**Figure 2-19**). From the single molecule traces extracted as shown in **Figure 2-19**, we gathered that the Cy3FP1 may not be photobleaching, instead, it may not be replenished quick enough. This conclusion is not final as this experiment lacked accepted counts for the FP condition of 250 nM. As such, there is not sufficient data to corroborate our hypothesis.

For miR-16, we also found a successful FRET detection of the target **Figure 2-17B**. The probes have also been studied indivually and tested across increasing temperatures as done for let-7a (data not shown). Optimization is still in progress, but it is promising to observe instances of FRET for other miRNA.
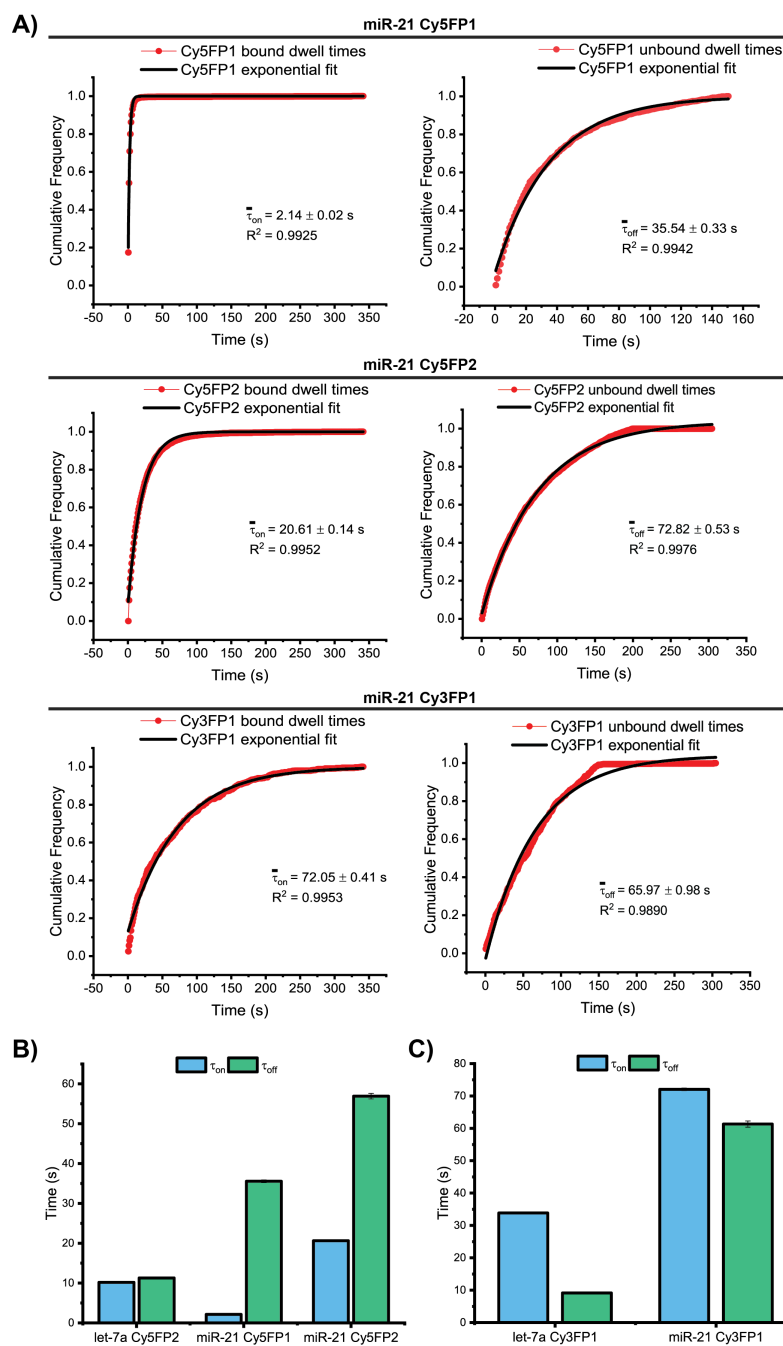
Figure 2-18 Kinetic analysis of FRET probes for miR-21. A) Single exponential fitting of dwell time cumulative frequency for miR-21 target bound ($\bar{\tau}_{on}$) and non-target-bound ($\bar{\tau}_{off}$) states for each corresponding FP. All experiments were performed in imaging conditions: [FP] = 25 nM, [Na$^+$] = 580 nM. (4X PBS). The time (t1) listed reflects the dwell time calculated from the fitted curve using all accepted traces. B) Comparison of average dwell times between Cy5FPs for miR-21 and the let-7a selected probe. C) Comparison of average dwell times between Cy3FPs for miR-21 and let-7a selected probe.
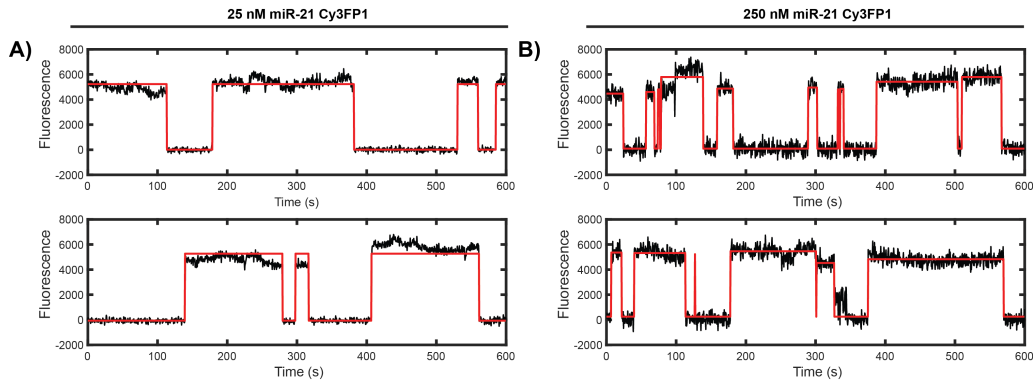
Figure 2-19 Representative single-molecule traces (black) with an idealized HMM fit (red) of Cy3FP1 behavior at A) 25 nM and B) 250 nM.

2.4.4 Optimization of Conditions for *in situ* Detection

Cellular imaging has been widely applied for the investigation of miRNA since it does not require cell lysis or RNA extraction which can compromise detection. Existing methods typically only allow for relative expression profiling versus quantitative information. The method of detection expressed above utilizes single molecule imaging of individual molecules that lends itself to *in situ* detection. For the application in cells, sensitive and specific probes were developed to overcome the short length of miRNA and nonspecific adsorption seen in probes. As discussed, two short fluorescently labeled DNA probes were employed to increase specificity while sensitivity was achieved via FRET vs the binding of many probes simultaneously as utilized for mRNA detection.
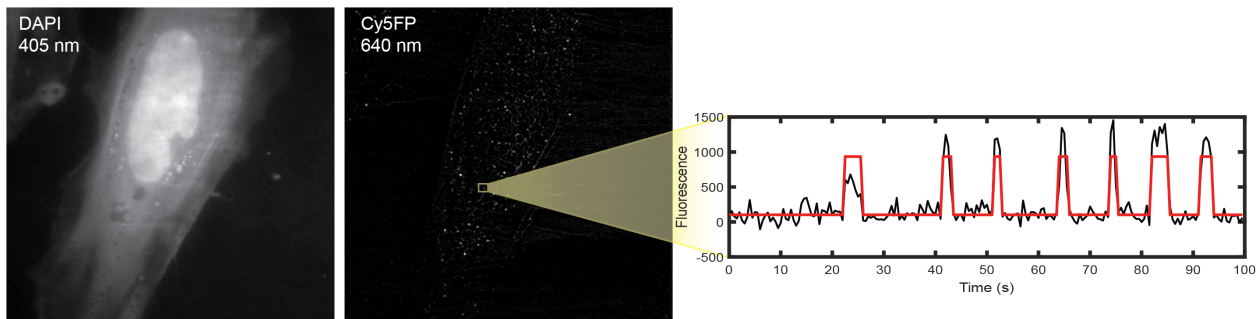
Figure 2-20 Single probe detection of miRNA within a fixed cell. A) DAPI stained fixed cell used to localize cells (left) and 640 nm illuminated cell (right). B) An extracted single molecule trace from direct excitation of a Cy5FP exhibiting a kinetic fingerprint with multiple binding and dissociating events.

Fixation Reagents for miRNA Detection

To demonstrate the application of the probes, we aimed to detect let-7a in single fixed HeLa cells. Fixation is a crucial step in processing the cells for examination and preservation of spatial information. In initial studies, the widely used fixative, formaldehyde, was utilized. As proof of principle, a single Cy5FP probe exhibiting transient binding *in vitro* was introduced into a fixed cell sample. The cells in the sample were also DAPI stained for cell nucleus localization. DAPI is a widely used fluorescent compound that binds preferentially to the minor grooves of AT regions of DNA. After localizing the cells via 405 nm excitation, the cells were then excited with a 640 nm laser and the Cy5 probe emission was collected by an EMCCD camera. As shown in **Figure 2-20**, the detection via a single FP was possible, however, at the expense of specificity. Like many miRNAs, let-7a has family members (10 identified) and all are highly conserved across species in sequence as well as function. Overall, the ability to detect a kinetic fingerprint using a single probe was promising and showed great potential for FRET detection.
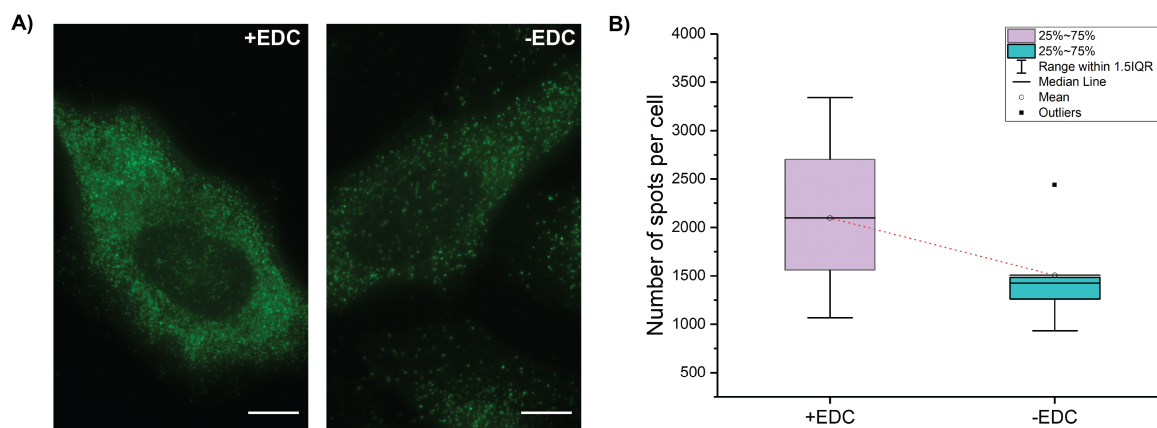
Figure 2-21 A) Visualization of microRNA expression when HeLa cells are treated with formaldehyde-fixed specimens, followed by treatment with EDC (left). B) Cells were analyzed for the Cy3-labeled LNA probe (in green). Cell images were analyzed for number of spots. Plot depicts higher density in presence of a second fixative, EDC. Scale bars are 10 μm.

In preparation for application of FRET detection, formaldehyde was the fixative of choice. Although formaldehyde is used routinely, for the purpose of miRNA detection it poses a

problem. The Tuschl group demonstrated that with only using formaldehyde, there is a loss of miRNA in wash steps. To overcome this, they employed EDC which can cross-link miRNA via the 5' phosphate to an amino group of a protein. This resulted in the preservation of miRNA during their sample treatment. We also utilized EDC in our fixation process to enhance miRNA detection. Our cells were first incubated with formaldehyde followed by EDC fixation. As depicted in **Figure 2-21**, we were able to replicate the preservation of biochemical information.
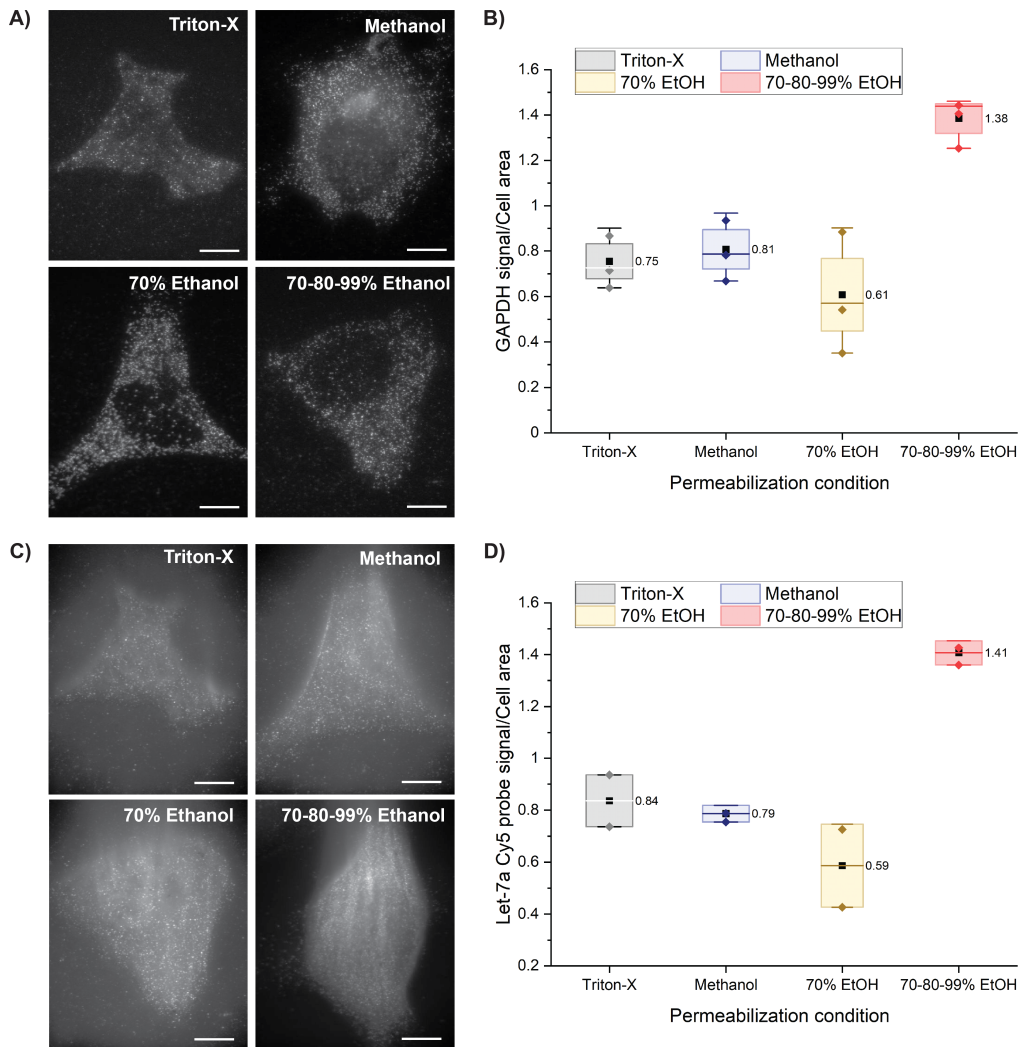
Figure 2-22 An evaluation of permeabilization conditions. A) Images of fixed cells incubated with GAPDH. For each permeabilization, FISH was performed utilizing the house keeping gene. B) The GAPDH signal over the cell's area was plotted to evaluate the efficiency of permeabilization method. C) Images of fixed cells incubated with let-7a Cy5FP to estimate and corroborate efficiency of permeabilization. D) The let-7a Cy5FP signal was plotted as done for GAPDH. Scale bars are 10 μm.

Permeabilization Analysis

Following this, we set out to evaluate permeabilization methods to choose what method best fit with our experimental needs. Cell permeabilization generates pores in the cell membrane to allow molecules, such as reader probes or antibodies, to pass into the cytoplasm to reach targets of interest. However, the permeabilization step may also result in loss of biochemical information and quality when the cell is exposed to harsh chemicals. Here, we evaluated 70% ethanol, 70-80-99% ethanol, methanol, and Triton X-100 as reagents. The organic solvents, ethanol and methanol remove lipids from the cell membrane. They can also be used as fixatives. Detergents such as Triton-X 100 also remove lipids and cholesterol. The exposure of cells to 70% ethanol overnight led to a decrease in biochemical information as visualized in **Figure 2-22**. While 70-80-99% ethanol retained the most biochemical information (**Figure 2-22**). On the one hand, we could use 70% ethanol since it can denature proteins, leading to a more accessible cellular environment. On the other hand, we could utilize 70-80-99% ethanol to avoid the possibility of any miRNA loss within the biochemical information that is removed with 70% ethanol. We decided to move forward with 70-80-99% ethanol to avoid potential loss of information.
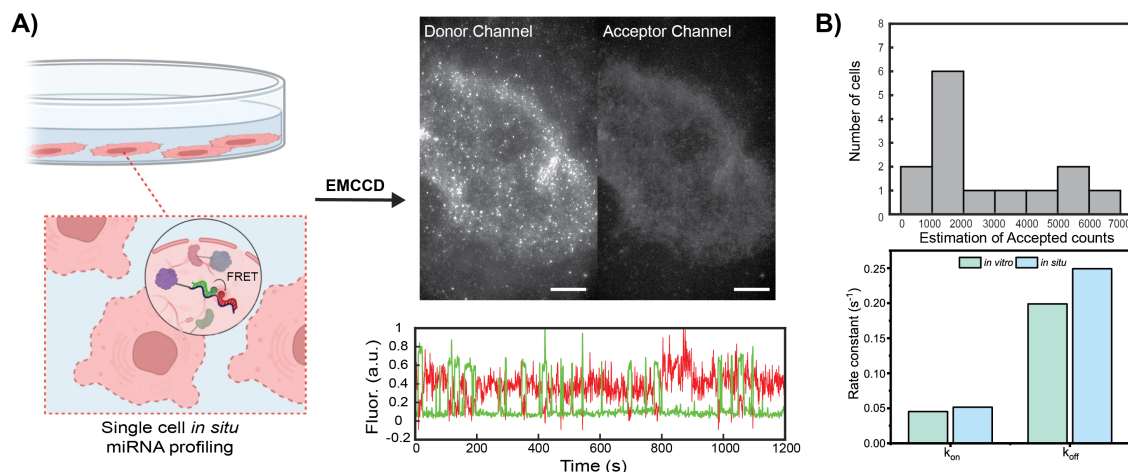
Figure 2-23 FRET detection *in situ*. A) Illustration of *in situ* FRET detection in single cells followed by imaging. Imaging shows a single movie frame of both donor and acceptor channels of data acquired with a representative

single-molecule trace extracted from that data. The single molecule trace is exhibiting anticorrelation events. B) Estimated number of accepted counts per cell extracted from acceptor channel only analysis (top). Rate constants determined from analysis of the average bound and unbound times extracted from accepted traces *in vitro* versus *in situ*.

2.4.5 FRET Detection in Single Fixed HeLa Cells

Next, we set out to introduce both the donor and acceptor probe. Initial experiments showed high signal density which made single molecules indistinguishable. This was a potential issue that was noted earlier. Due to the high concentration of both Cy5FP2 and Cy3FP1 and potential presence of multiple let-7 family members, it was difficult to identify single molecules. To alleviate the issue, we introduced a blocker which could potentially aid in blocking off let-7 members. After incubation with the blocker, we were able to obtain single-molecule resolution. As shown in **Figure 2-23**, the detection of let-7a *in situ* via FRET was successful. Following this, the movies acquired were split into individual channels in ImageJ. The red channel, emitting signal of the transient probe, was analyzed utilizing the single-probe analysis software (see **Section 2.3.7**). From this analysis, we determined accepted counts per cell. Given that our detection only spans 100 nm and that the height of a cell is ~16-20 μm, we increased our accepted counts by 20-fold. As such, we obtained an estimated number of counts per cell (**Figure 2-23B**). Although we were able to detect let-7a, there is not sufficient data to support our assay is robust. Additionally, the cells exhibited a high background which limited detection. In effort to reduce high background, borohydride which is a reducing agent utilized for autofluorescence reduction was employed. As seen in **Figure 2-24**, the addition of borohydride was found successful in reducing background. Further experimentation is necessary, but it is promising to observe anticorrelation events and an estimated number of counts near 1000-3000, which has been previously reported for let-7a per HeLa cell [131–133].
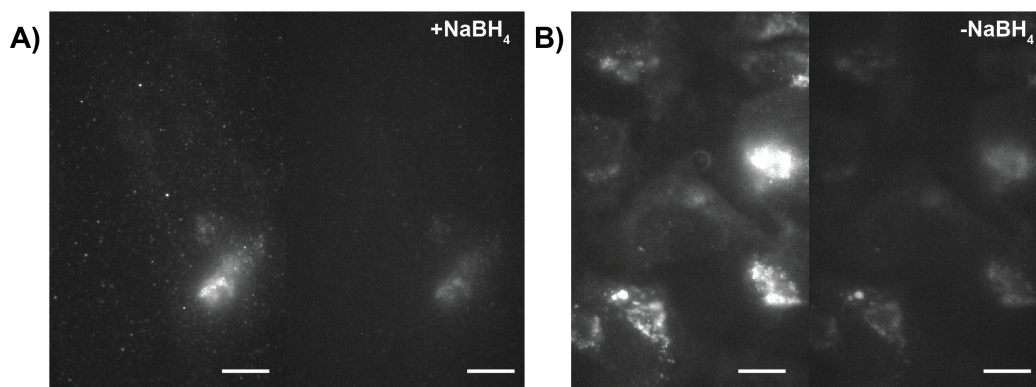
Figure 2-24 Visualization of cells in absence of fluorescent probes that were treat A) with and B) without NaBH$_4$. Scale bars are 10 µm.

2.4.6 Expansion Microscopy: An Alternative

In parallel, we began investigating a different avenue as a solution. Given the crowded environment and the diffraction limit posed by microscope optics, we decided to subject our cells to the expansion microscopy technique. This expansion in space allows us to isotropically expand (~4.5× in the linear dimension) a preserved biological specimen [134], cells in our case. This magnification allows for molecules in diffracted limited areas to be separated and therefore be resolved which has the potential to allow us to enhance our detection method.
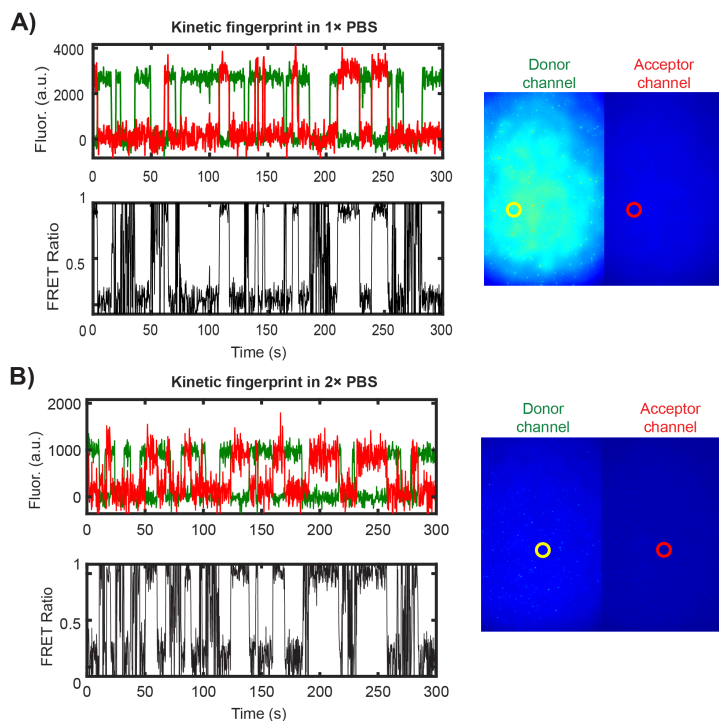
Figure 2-25 Investigation of salt concentration on detection of let-7a *in vitro*. Representative traces for different salt conditions resulting in dynamic kinetic fingerprints. A) FRET trace of donor (green) and acceptor (red) FP exhibiting a kinetic fingerprint in 1× PBS. B) FRET trace of donor (green) and acceptor (red) FP exhibiting a kinetic fingerprint in 2× PBS.

Initial testing included reducing the salt concentration utilized when imaging. This was necessary to lessen the shrinking of the gel caused by the presence of salts. To accomplish this, the detection of let-7a was tested in lower salt conditions (1× and 2× PBS) (**Figure 2-25**). After verifying detection at lower salt conditions, investigation of its application in an expanded environment was initiated. The cells were seeded on a petri dish with coverslips. Following that, the coverslip was placed over a glass slide with coverslips (as shown in **Figure 2-26**) and the gelation solution was pipette into this microfluidic-like design. The gel was then processed and finally expanded ~4× its original size. Following this, the gel was cut and placed on a glass bottom imaging dish and the fluorescent probe was pipetted over the gel. As seen in **Figure 2-26**, the Cy3 FP was able to reach the cell while the Cy5 FP did not. In addition to the unsuccessful probing, while attempting to image the cells the gel began to shrink. It was expected that the use of salts would have an impact on the stability of the gel which prompted the use of a new

protocol for expansion microscopy recently reported which could overcome the issue at hand. Further investigation is necessary to test the practicality of this application.
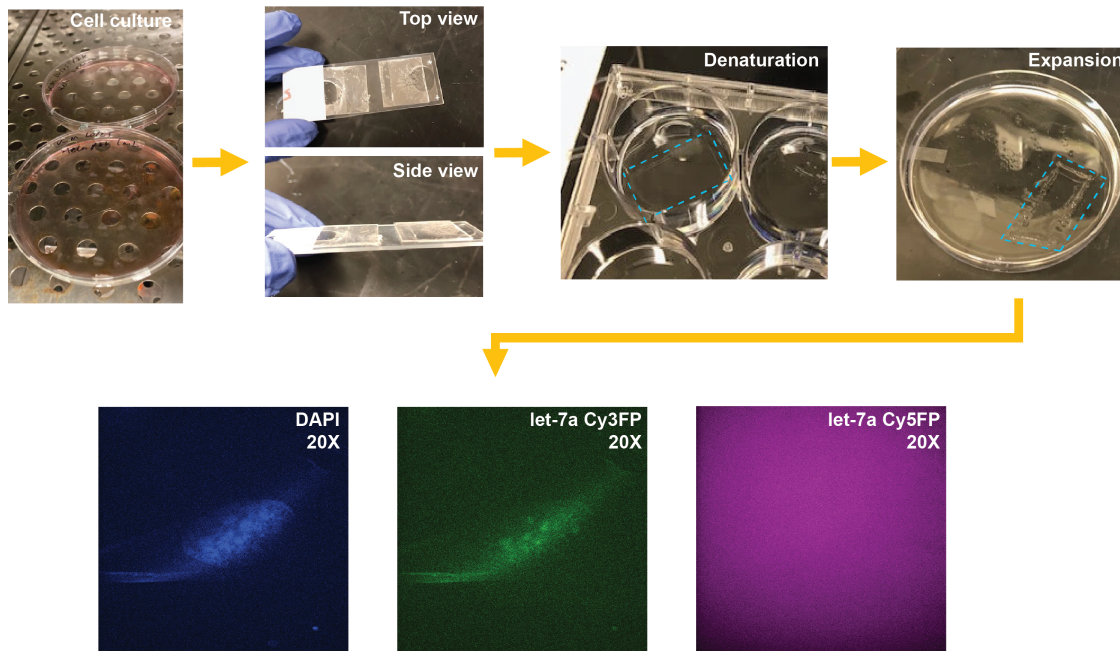
Figure 2-26 Workflow of expansion microscopy. Step 1: Culture cells, followed by fixation and permeabilization. Step 2: Construct a gelling chamber by cutting a glass coverslip with into two pieces and placing them on a glass slide, then place a coverslip with cells above them and introduce a gelling solution. Step 3: Carefully remove sample from the glass slide using a soft brush and place in a well for processing. Step 4: Add freshly prepared denaturation/digestion solution. Step 5: Transfer to a dish and expand the sample by washing in excess ddH$_2$O in 3-5 repeated rounds for 10 minutes. Step 6: Transfer sample to a dish compatible with fluorescent imaging and add fluorescent probes and image.

2.5 Summary and Future Directions

In this chapter, the proof-of-concept of FRET detection *in situ* was demonstrated. A FRET probe pair was designed and optimized to detect let-7a while 2 other miRNA probes are in progress and show high potential in successful detection. The let-7a FRET pair successfully detected target in vitro and has shown itself applicable to a cell environment. I have investigated and found a set of fixation and permeabilization reagents that will present us with optimal amount of information and quality. I have been able to obtain signal within a fixed cell. This was accomplished by investigating and applying conditions for cell fixation and permeabilization to

facilitate miRNA detection. A fixative, EDC, was introduced to further aid in crosslinking miRNA within the cell matrix. Following this, different permeabilization conditions were investigated and the 70-80-99% Ethanol method was chosen since it was discovered that it produced the most signal retention. This chapter also showed that although the assay needs further development, it is possible to utilize FRET probes for detection in fixed cells. Further development includes investigating Locked Expansion Microscopy which would increase the access to miRNA or multiple miRNAs in the sample due to its isotropic volume increase.

Locked expansion microscopy utilizes a mechanically stable gel network to prevent the original polyacrylate network from shrinking in ionic buffers. This method was particularly developed for the application in super-resolution single molecule localization microscopy which utilize anti-photobleaching buffers not compatible with traditional expansion microscopy. Fan *et. al.* introduced a secondary polymer network, poly(ethylene glycol) (PEG), to lock the size of the expanded polyacrylate gels. PEG was utilized since it lacks ionic groups and interacts with water molecules through hydrogen bonding independent of the electrostatics between polyacrylate chains and salt ions. Once this is achieved, detection should be applied in different cell lines to show robustness as well as detection for other miRNA. With increased resolution achieved via expansion, this technique lends itself to multiplexing of miRNA or other analytes simultaneously.

Chapter 3 : Detection and Quantification of Single MicroRNA Molecules in Isolated and Lysed Cells Utilizing a Microfluidic Platform and an Aqueous Two-Phase System

3.1 Overview

Due to variations in spontaneous mutations, epigenetics, and potentially stochastic gene expression between cells, bulk observations of a cell population may not accurately represent all behaviors of individual cells [135]. Cell-to-cell heterogeneity is always present within a cell population and understanding the differences and how components change will provide the ability to uncover mechanisms dictating functions for homeostasis and development of disease states. This has led to a massive effort to categorize every sort of cell as well as to develop technology capable of tracking differences between cells in a heterogenous environment (e.g. tumor). Therefore, new technologies to isolate individual cells from a complex sample and study their genomes and proteomes promises to provide great insights on genome variation and gene expression processes [136]. This led to the development of single cell sequencing technology. Like typical next generation sequencing, single cell sequencing requires a starting sample, in this case isolated single cells, followed by lysis, nucleic acid extraction and amplification, and finally library preparation, sequencing and analysis of the data acquired. Considering the low count of molecules from a single cell, degradation, sample loss and/or contamination will have prominent effects on the quality of the data. This issue can also arise from the amplification necessary to execute adequate analysis of single cells. As such, current techniques for single-cell analysis usually lack adequate sensitivity and quantitative accuracy for rare or hard-to-amplify species.

SiMREPS, the amplification-free kinetic fingerprinting approach for digital single-molecule detection described previously, allows for highly specific, sensitive, and rapid detection of molecular species in free solution. Substituting downstream sequencing with SiMREPS has the potential to develop a high-throughput screening technology. This chapter will address the synergistic approach of microfluidics and SiMREPS utilized for the development of a platform with potential for parallel detection of multiple microRNA (miRNA) biomarkers, to be able to detect their abundance in single cells to help better understand human health and predict the likelihood of human disease, including cancer progression.

3.2 Introduction

A major focus of technology development over the past years has been on increasing sensitivity of biomarker detection tools. At the same time, there has been a considerable amount of effort put into single cell sequencing. We've known for many decades that there are tumor derived cells in the blood stream of a cancer patient, but the sensitivity of technologies was not sufficient. Today we have existing technologies that are allowing us to capture the heterogeneity of a tumor. Understanding the connections and transitional states among the cells within the tumor can help define mechanistic pathways governing cancer evolution. Despite the achievement in current technologies, there are still hurdles to overcome.

3.2.1 Single-Cell Analysis

Single-cell sequencing technologies refer to the sequencing of a single-cell genome or transcriptome to reveal cell population differences and cellular evolutionary relationships. In 2009, Tang's group firstly reported the mRNA-seq whole-transcriptome analysis method on a mammalian single cell [137]. In 2011, Navin *et al.* achieved the genome sequencing of a single

human cell to investigate the structure and evolution of the tumor cell population in breast cancer [138]. It was not long before the development of single-cell techniques that the field began using microfluidics. Researchers have also applied low-throughput single cell analysis techniques, such as immunofluorescence, fluorescence *in situ* hybridization (FISH) and single cell PCR, to detect certain molecular markers of single cells [139,140]. However, microfluidics provides many benefits over conventional techniques.

3.2.2 Microfluidics Application: Its Advantages and Disadvantages

The field of microfluidics concerns the manipulation and precise control of fluids, typically in the microliter to picoliter range, at which the Reynolds number generally is in the laminar flow regime [141–143]. Over the past few decades, there have been many efforts to extend the application of microfluidics into biology and clinical applications [142]. Today, microfluidics is recognized as a powerful enabling technology for investigating complex cellular systems since it provides precise fluid control, low sample consumption, device miniaturization, low analysis cost, and easy handling of nanoliters volumes [143]. The advantages of integrating cell handling and processing synergistically prompted its entry into commercialization. A company, Fluidigm, developed an automated microfluidic system capable of RNA sequencing workflows among others.

Despite the great achievement in analyzing single cells, there are still certain concerns with the current systems. Single-cell sequencing is more challenging to perform than sequencing from cells in bulk. Inputting millions of cells versus isolating single cells and/or performing downstream analysis will result in pronounced effects due to potential degradation, sample loss, and contamination. It is also important to highlight that amplification is accompanied by errors emerging from sequence bias from reverse transcriptases and ligases which can result in uneven

coverage. Additionally, if contaminants are present, further purification is needed which could cause a huge problem at such low concentrations.

Taken together, the downstream application of NGS approaches can result in inaccurate quantification of the target RNAs. To overcome such barriers, SiMREPS was explored as a possible solution. Detecting a specific signal from individual biomolecules of interest poses a challenge due to the low abundance within a single cell and, and therefore, the need to distinguish true signal over background. SiMREPS is capable of high specificity and sensitivity, and its kinetic fingerprinting enables nearly perfect discrimination between specific binding to target molecules and any nonspecific binding to virtually eliminating background, making it a plausible alternative.

3.2.3 SiMREPS: Its Advantages and Disadvantages

To date, SiMREPS has proven successful in detection of molecular analytes as diverse as miRNAs, ctDNAs, proteins, and small molecules with high specificity and sensitivity [97,101,53,144,145]. Early proof-of-concept studies demonstrated the in vitro detection of miRNAs with a limit of detection (LOD) of approximately 1 fM and >500-fold selectivity for single-nucleotide polymorphisms [97]. The SiMREPS approach was subsequently expanded to the detection of rare mutant DNA alleles from biofluids at mutant allele fractions of as low as 1 in 1 million, corresponding to a specificity of >99.99999% [53]. SiMREPS has also been demonstrated to be suitable for the *in situ* detection of miRNAs in cultured cells [101]. Most importantly, SiMREPS has been able to achieve a LOD in the low-femtomolar to attomolar range [146].

The high specificity and sensitivity enabled by SiMREPS motivated its application in combination with microfluidics. In this approach, the microfluidic chip will perform the single-

cell extraction and lysis step, followed by analysis via SiMREPS. An applicable and appropriate biomedical device available at the time included the Fluidigm platform. The Fluidigm system physically isolates each single cell into a single well chamber for lysis and extraction in comparison to other technologies such as 10x Genomics, which pool thousands of cells into one sample. The flexibility offered by Fluidigm facilitated the incorporation of the SiMREPS technology. Particularly, Fluidigm has the capability of introducing user-defined scripts without the necessity of sequencing making the implementation of SiMREPS possible. In addition to the refinement by an amplification-free technique, the new approach also has advantages over other RNA isolation and quantitative techniques as microfluidics rely on just one technology and SiMREPS requires no RNA extraction, therefore eliminating the increased variability caused by technical errors introduced over multi-platform pipelines. However, the particular pipeline described in this chapter comes with its own limitations. After isolating and lysing cells, they are harvested in a volume of around 3µL which decreases the concentration of analytes and necessitates a highly sensitive assay.

Despite their extremely high specificity, the sensitivity of surface-based SiMREPS assays due to mass transport was still an issue. Diffusion-limited surface capture was not sufficient to detect low-abundance targets in biofluids and would pose a huge problem when only analyzing the contents of one cell. The single cells are also in a much larger volume, adding a further barrier. In addition, the significant time requirement for SiMREPS data acquisition (10 min) limited detection of analyte to only a few fields of view, as it does not permit scanning of the whole capture surface. Therefore, an aqueous two-phase system under development for circulating tumor DNA (ctDNA) detection was tested on miRNA to alleviate this limitation and improve the assay [146]. Additionally, as seen in Chapter 2, with an increase in parameters such

as temperature, a higher N_{b+d} was achievable which could increase the confidence of target detection and therefore reduce the necessary acquisition time if the N_{b+d} was sufficiently high to continue being distinguishable above background. This would permit more sample area to be investigated and could further improve the sensitivity of the assay in conjunction with ATPS.

Aqueous Two-Phase System (ATPS) for miRNA Pre-concentration

ATPS is a liquid-liquid extraction system utilizing two aqueous phases capable of separation and purification of biomolecules such as proteins, antibodies and most importantly for this work, nucleic acids [147,148]. The way it functions is by utilizing two-water soluble polymers or a polymer and a salt. When introduced in water, the ATPS will form two immiscible aqueous phases. This system comes with the advantages of utilizing water versus organic components, selective separation, and rapid mass transfer. In this study, the use of a salt and polymer was applied which led to other advantages such as lower cost and a lower viscosity making it easier to handle as well as resulting in less interference with diffusion of the molecules. Here, we used SiMREPS combined with ATPS to improve the potential of miRNA detection and quantification. The power of ATPS permitted an increase in target capture efficiency by enriching a target miRNA into a smaller sample volume, in this way facilitating its mass transport to the surface for a ~14 -fold higher sensitivity.

Multiple FOV Acquisition and 3D Printed Sample Wells

The classical SiMREPS assay design previously required 10 min for acquisition which motivated optimization to decrease acquisition time and design of sample wells. As mentioned above, the diffusion limited surface capture affected sensitivity. In combination with the 10 min observation period, it was difficult to acquire multiple FOVs that would help improve sensitivity because of the larger capture area surveilled. To this end, the detector probes underwent

optimization as presented in Chapter 2. The optimization was expected to allow for faster data acquisition than the previous assay conditions [97]. The decrease in acquisition time enabled further improvement in sensitivity by permitting the investigation of a larger surface area in the same amount of time, therefore detecting additional captured target molecules. Additionally, the sample well surface area and volume size were decreased and facilitated diffusion, thus allowing for a larger fraction of target to be captured within a single FOV, further increasing sensitivity. These combined approaches made it possible to increase the capture efficiency as well as to detect a larger fraction of captured target by scanning multiple FOVs resulting in a higher sensitivity.

3.2.4 SiMREPS-Microfluidics Approach

Here, we used the classical one-color probe SiMREPS to process single cell lysates obtained from the downstream processing of the Fluidigm C1 automated microfluidic system. To improve the detection sensitivity of the SiMREPS assay for application in single cell lysate, we introduced a new sample preparation utilizing ATPS to enhance the surface capture of miRNA target.

3.3 Materials and Methods

3.3.1 Reagents and Consumables

All the DNA oligonucleotides used in this study were purchased from Integrated DNA Technologies (IDT) with standard desalting purification and/or HPLC. The fluorophore-labeled oligonucleotides were HPLC purified. Capture probes with biotin and locked nucleic acid modifications were purchased from Exiqon with HPLC purification. All oligonucleotide sequences are shown in **Table 3-1**. The probes listed are used from Johnson et al. All the

oligonucleotides were aliquoted and stored at -20 °C prior to use. Streptavidin (S-888) was purchased from Invitrogen. 10× Phosphate-buffered Saline (PBS, pH 7.4, Catalog no. 70011044), Trolox (Catalog no. MFCD00006846), 3, 4-Dihydroxybenzoic Acid (PCA, Catalog no. AC114891000) were purchased from Fisher Scientific. Protocatechuate 3,4-dioxygenase (PCD, P8279-25UN), Poly(ethylene glycol) (PEG) with an average molecular weight of 3350 Da (Catalog no. P4338-500G), sodium citrate dihydrate (Catalog no. W302600-1KG-K) and (3-Aminopropyl)triethoxysilane (Catalog no. A3638-100ML) were purchased from Sigma-Aldrich. Sodium chloride was purchased from Fisher (catalog no. S271-10). Methoxy-polyethylene glycol-succinimidyl valerate (mPEG) and biotin-polyethylene glycol-succinimidyl valerate (biotin-PEG) were purchased from Laysan Bio, Inc (catalog no. BIO-PEG-SVA-5K-100MG and MPEG-SVA-5K-1g). Sodium bicarbonate was purchased from Acros Organics (catalog no. AC217120010). Disuccinimidyl tartrate (DST) was purchased from Soltec Ventures. Bis-Acrylamide 19:1 (40% Solution) solutions of 19:1 was purchased from Fisher Scientific (Catalog no. BP1406-1). Ethanol (200 proof; Thermo Fisher, catalog no. T038181000) was purchased from Thermo Fisher. SYBR Gold was purchased from Thermo-Fisher (Catalog no. S-11494). All samples utilized for experiments prepared and storage in GeneMate 2 mL low-adhesion microcentrifuge tubes (VWR, catalog no. 490003-302). All sample wells were attached utilizing Epoxy adhesive (Ellsworth adhesives, hardman double, catalog no. 4001).

Table 3-1 Detail of sequences of oligonucleotides

ID	Sequence 5'-3', T_m (4× PBS)	Remark
let-7a	/Phos/UGAGGUAGUAGGUUGUAUAGUU	RNA target
let-7a FP	/Cy5/ACTATACAAC, T_m = 17.4 °C	Cy5 detection probe
let-7a CP	TACTACCTCA/biotin/, T_m = 41.1 °C	LNA capture probe
miR-16	/Phos/UAGCAGCACGUAAAUAUUGGCG	RNA target

Note: T_m of FP-target was calculated using IDT OligoAnalyzer having parameters: Target type: RNA, Oligo conc: 0.025 µM, Na$^+$: 580 mM (4x PBS).

3.3.2 Cell Line

HeLa (CCl-2, ATCC) cells were propagated in DMEM (GIBCO, #11995) and supplemented with 10% FBS (GIBCO, # 16000). All medium typically contained 1x Penicillin-Streptomycin (GIBCO, #15140). For selection of lysis buffer, cells were imaged before and after incubation with lysis reagent. Cells underwent trypsinization and viability was measured before resuspending in a smaller volume. For the lysis reagents, the mix of the C1 lysis buffer and single cell-to-Ct lysis buffer utilizing either "C1 loading buffer" or "DNA dilution buffer". Additionally, a third lysis mix utilized by Fluidigm, mRNAseq lysis mix was utilized. Refer to the **Table 3-2** below for more details on the lysis mixtures. HeLa cells were cultured and a cell suspension of 60,000-300,000 was prepared ensuring 200-1000 cells are loaded into the microfluidic chip.

Table 3-2 Lysis mixture components.

Lysis mix #1
Single Cell-to-CT Lysis Buffer
C1 Lysis Plus Reagent
C1 DNA Dilution Reagent
Lysis mix #2
Single Cell Lysis Solution
C1 Lysis Plus Reagent
C1 Loading Buffer
Lysis mix #3
C1 DNA Loading Reagent
RNase Inhibitor
3' SMART CDS Primer IIA
Clontech Dilution Buffer

3.3.3 Fluidigm C1

The Fluidigm C1 microfluidic platform was utilized to isolate and then lyse HeLa lysates. The C1 has a script builder modality which was altered to isolate, lyse and then harvest cells for downstream analysis via SiMREPS. The C1 script was programmed to prime the IFC prior to cell introduction. Following this, the cells would flow in through the device and captured at 1 of

96 potential sites available on the device. The lysis mixture was then introduced, and cells were lysed and harvested. The Script is available in the Appendix. Prior to utilizing the script, IFC was selected based on cell size. A hemocytometer was utilized to obtain the size range of the HeLa cells to be used in the process (**Figure 3-1**). Following this, preliminary optimization in tubes had to be performed. A bulk cell sample (1,000× than utilized for the IFC run) was tested with all the reagent mixes to ensure lysis would occur during processing.
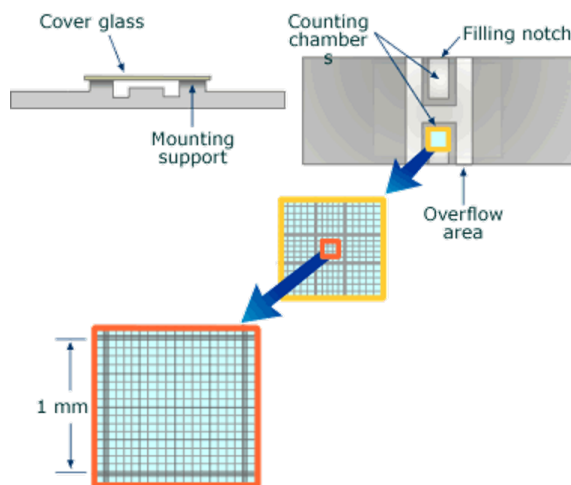
Figure 3-1 Illustration of a hemocytometer. A hemocytometer is a chamber designed to count the number of cells in a sample. The hemocytometer has grooves on both sides with a grid of perpendicular lines attached in the center. A cover glass is placed on top as a lid and the chamber is filled by capillary action. The number of cells in the chamber is used to calculate the concentration of the cells in the sample [149].

3.3.4 Preparation of the Aqueous Two-Phase System

The ATPS used in this study was prepared as described in Li *et al*. The ATPS was composed of PEG 3350, sodium citrate dihydrate and sodium chloride. To prepare the ATPS, a master mix was prepared by dissolving 6.56 g of PEG 3350, 0.348 g of sodium citrate dihydrate and 0.498 g of sodium chloride in 30 mL of milli-Q purified water in a 50-mL centrifuge tube. The mixture was vortexed at high speed until the powder was fully dissolved and solution appeared clear. The solution was centrifuged at 1000 x g for 1 min at room temperature to remove air bubbles. Small volumes (36 μL) of ATPS master mix solution were aliquoted into GeneMate 2 mL low-adhesion microcentrifuge tubes, flash-frozen with liquid nitrogen, and

lyophilized. The lyophilized ATPS aliquot obtained from the 36 µL master mix solution (will be referred to as "0.1× ATPS" for the remaining sections) was used to dissolve 10 µL sample solutions. The final composition of the ATPS components after sample addition was 37.7% (w/w) PEG 3350, 2 % (w/w) sodium citrate and 2.8% (w/w) sodium chloride. The ATPS lyophilized aliquots were stored at room temperature until use for experiments.

3.3.5 Characterization of Enrichment Utilizing a UV-Vis Spectrophotometer

Enrichment of miRNA was investigated utilizing UV-Vis (**Figure 3-2**). A set of concentrations ranging from 0.1 µM – 5 µM were introduced into the ATPS system to determine the enrichment. The ATPS mixture was prepared as described above (Section 3.3.4) without the introduction of water. The powder mixture was vortexed thoroughly and then 222 mg were weighed out into individual Eppendorf tubes. Serial dilutions were performed to obtain corresponding concentrations (0.1 µM – 5 µM) in 300 µL of 1× PBS. The 300 µL were then added to a corresponding tube with ATPS mixture. This particular amount of ATPS mixture would yield ~ 20 µL of the salt-rich phase to facilitate measurements. The mixture was then vortexed for 2 minutes and finally centrifuged at 10,000 g for 1 minute. A clear phase separation was observed. Each salt-rich phase was measured three times per sample at 260 nm, starting with the blank.
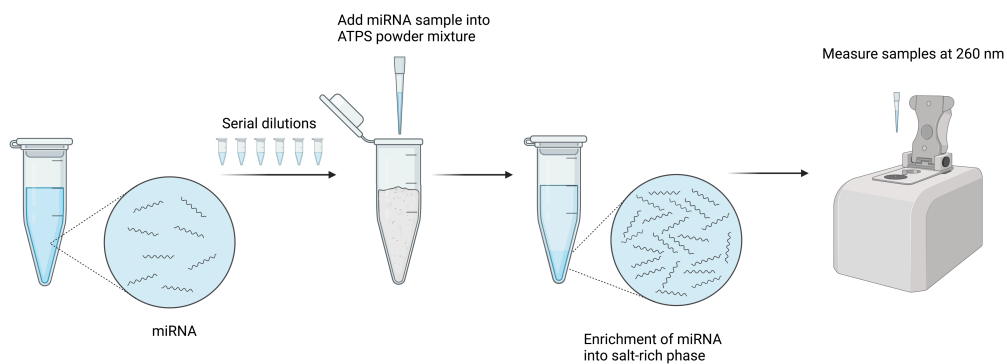
Figure 3-2 An illustration of the workflow for characterization of enrichment of miRNA. Step 1: A known sample of DNA is used to make a set of serial dilutions. Step 2: The diluted samples are added into a ATPS powder mixture. Step 3: The ATPS samples are vortexed, centrifuged and a clear separation is achieved. The nucleic acid partitions into the small volume, salt-rich phase. Step 4: The salt-rich phase is measured at 260 nm to determine the concentration of the miRNA. Figure generated using Biorender.

3.3.6 ATPS-SiMREPs Assay

3D Printed Wells

In contrast to previously published SiMREPS assay protocols [53,67,97–99], here we applied ATPS to miRNA target molecules to pre-concentrate for higher sensitivity. To further facilitate pre-concentration, the assay surface area was adjusted by incorporating a 3D printed strip with 5 wells with openings 0.5, 0.8, 1.2 or 2 mm in diameter. The 3D-printed strip wells were designed in Fusion 360 (Autodesk) and 3D-printed with a z-feature resolution of 16 microns from VisiJet m3 crystal material using a Projet 3500 3D printer at the Duderstadt Center's Fabrication Studio at University of Michigan. Prior to an experiment, 3D-printed well strips were cleaned by sonicating in warm water (45-50°C) multiple times until the washing water was near clear. The washed 3D-printed wells strips were rinsed thoroughly with absolute ethanol and then rinsed again with water. Finally, the wells were blown dry using nitrogen.

Sample Well Preparation

Similar to previously published papers [53,67,97–99], the 3D-printed strip well was

84

attached to biotin-PEG functionalized coverslips with a fast-curing Epoxy adhesive. The 3D printed wells were place on a non-functionalized coverslip on a bench vise, specifically on the stationary jaw (**Figure 3-3**). The sliding jaw was equipped with double-sided tape and was carefully lowered to attach the well strip. The coverslip was then removed and replaced by a biotin-PEG functionalized coverslip. The sliding jaw with the 3D printed strip was carefully lowered onto the coverslip with minimal lateral movement, to avoid damage to the biotin-PEG coating. Then epoxy was utilized for effective sealing in order to prevent leakage. The epoxy was left to dry for at least 15-20 mins and then the sample chamber was carefully removed from the bench vise. The sample wells underwent a visual quality check to ensure the epoxy did not seep into the wells before being ready-to-use for experiments.
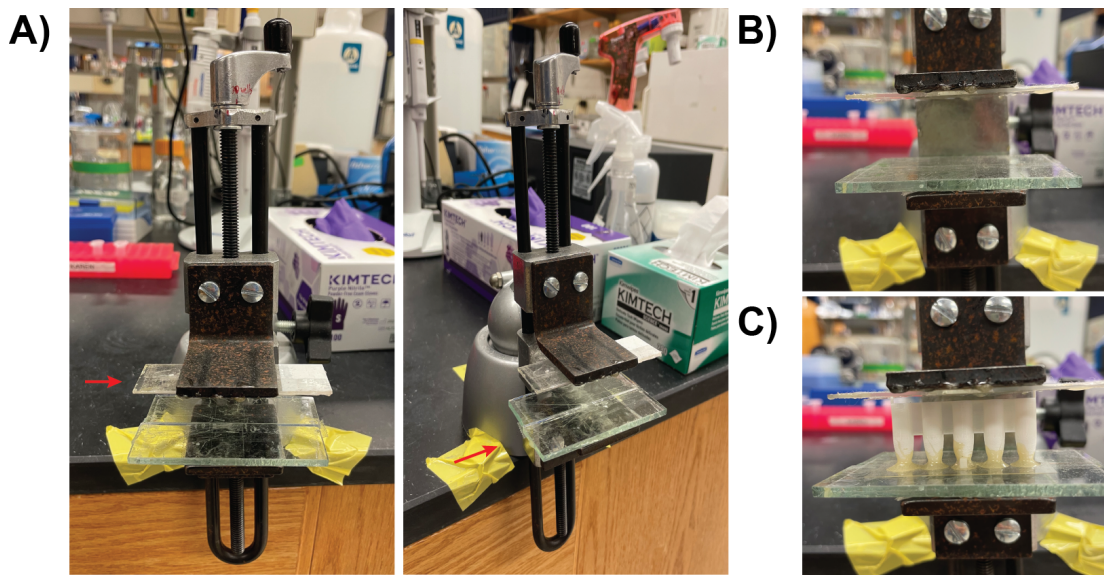
Figure 3-3 Bench vise device utilized in sample well preparation. A) Front view and side view of bench vise showing the sliding jaw with a glass slide attached (red arrow, left photo) and the stationary jaw (red arrow, right photo). B) Zoom in of jaws. Upper, sliding jaw contains double-sided tape for securing 3D-printed well strip. C) Closed jaw with coverslip and 3D-printed well glued with epoxy.

ATPS-SiMREPS Quantification of Synthetic miRNAs

Quantification of synthetic miRNA was performed as follows. Each well was washed once with T50 buffer (10 mM Tris-HCl, pH 8.0, 50 mM NaCl). Next, 10 μL of 1 mg/mL of

streptavidin was added into the 1.2 mm diameter 3D-printed sample wells and incubated for 10 min. This allowed for streptavidin to bind to the biotin-PEG on the coverslip surface. Wells were then washed three times with 100 µL of 1× PBS buffer to remove excess streptavidin, followed by incubation with 10 µL of 100 nM biotinylated and LNA-modified capture probes for 10 min. Wells were then washed three times with 1× PBS, and the final wash was left in the well until the sample was added.

To prepare target solutions for spike-in experiments, we prepared either specific concentrations or serial dilutions in 2 µM dT_{10} in ultra-pure water, where the dT_{10} serves as a carrier to prevent loss of the target. Next, 10 µL of the appropriate concentration of target miRNA solution was added to an aliquot of lyophilized ATPS prepared previously, and then vortexed at maximum speed for 1 min, followed by centrifuging at 10,000g for 1 min. A clear droplet separated from the remaining ATPS mixture indicated successful phase separation. The sample containing the droplet was then introduced into its corresponding 3D-printed sample well coated with streptavidin and biotinylated LNA capture oligonucleotide. The coverslip with 3D printed wells was then centrifuged at 3,000 rpm (1439 x g) in a centrifuge for 1 h at room temperature. A custom 3D-printed coverslip holder was used to hold the coverslip in place inside the swinging bucket. Next, samples were removed from the wells, and the wells were washed with 4× PBS. Finally, 100 µL of an imaging buffer containing an oxygen scavenger system (50 nM protocatechuate dioxygenase, 1 mM Trolox and 5 mM 3,4-dihydroxybenzoate), 25 nM of Cy5-labeled fluorescent probe was added to each well immediately before imaging.

3.3.7 SMFM

SiMREPS experiments were performed on two Olympus IX-81 objective-type TIRF microscope equipped with a 60x oil-immersion objective (APON 60XOTIRF,1.49NA) with both CellTÎRF and z-drift control modules, and an EMCCD camera (IXon 897, Andor). Excitation of the Cy5 fluorescent was provided by a 640 nm red laser operating at 9-20 mW output power (~9-20 mW exiting the objective) at a calculated TIRF penetration depth of 70-90 nm, and emission was detected with an exposure time per movie frame of 250 or 500 ms. The multi-well scanning mode in Metamorph®, the acquisition software, was used to control a motorized stage to collect a total of 10 FOVs for each sample for 30 min for 1.2 mm- diameter 3D-printed wells. Each FOV was was 120×120 μm or 14, 400 μm^2 in size.

3.3.8 Data Analysis

A custom MATLAB code was used to investigate kinetic data as described previously (Section **1.6.2**). The MATLAB code identified sites of fluorescent probe repeated binding and dissociation in a 120 x 120 μm field of view and generated intensity-versus-time trajectories for each detected spot passing a threshold. Then, hidden Markov modeling (HMM) was applied to the intensity-versus-time traces to identify the binding and dissociation events within each trace. Based on the idealized HMM traces, several parameters including N_{b+d}, the number of binding and dissociation events; $\tau_{bound, median}$ and $\tau_{unbound, median}$, the median dwell times in the probe-bound and probe-unbound states, respectively; $\tau_{bound, max}$ and $\tau_{unbound, max}$, the maximum dwell time in the probe-bound and probe-unbound state can be utilized as thresholds to either accept or reject traces. Threshold values for each of these parameters were determined either manually or via another custom MATLAB code for optimization of thresholds to minimize false positives in controls while maximizing true positives in positive controls containing the target analyte [67].

3.4 Results and Discussion[4]

SiMREPS application to an environment *in situ* has the potential to effectively interrogate many analytes. However, the lack of automation of the experimental protocol developed in Chapter 2 motivated exploring another capable module in parallel. Here, we focused on investigating single cells being processed in a microfluidic device (**Figure 3-4**). This investigation of a new platform for profiling single cells was not designed to overlook the importance of other single-cell methods like the *in situ* project described above, but to expand the scope of our understanding of miRNA and to show alternative methods other researches can explore within the capacity of their laboratories.

Figure 3-4 Workflow of single cell miRNA profiling utilizing the Fluidigm platform. Phase 1: Script design for cell isolation, lysis and harvesting performed. IFC, microfluidic chip, size determined by investigating size of cells. Optimization of lysis reagents in bulk cell sample. Phase 2: Isolation of cells followed by imaging. Cells lysed and harvested for downstream analysis. Phase 3: Sample coverslips for SiMREPS prepared. Nucleic acid enrichment of cell lysate material. Data acquisition of cell lysate samples and analysis of miRNA levels.

3.4.1 Single Cell Isolation and Lysis

The detection design of SiMREPS lends itself to many applications. Here, we evaluated its application to detect single cell lysates isolated using microfluidics. Microfluidics offer a

---

[4] K.M. performed and analyzed all data collected. Z.L. provided ATPS aliquots for experiments. All data visualization was produced by K.M.

significant advantage over other platforms as it requires a low volume input of sample and reagents resulting in lower costs as well as the ability to analyze a sample multiple times and has the capability of high-throughput analysis. To obtain single cell lysates, we employed the Fluidigm C1 platform for the microfluidic isolation and lysis of single cells for subsequent analysis of their nucleic acid contents by kinetic fingerprinting. The Fluidigm C1 platform is designed to isolate, lyse, amplify material, and then undergo sequencing. In collaboration with the Single Cell Sequencing Core, we developed the first script (**Appendix Figure 5**) that would allow researchers to apply different downstream analyses to the harvested lysed cells. Contrary to its general application, the script would isolate, lyse and then harvest cells removing the amplification process. The cells would then be analyzed by SiMREPS which omits amplification to alleviate errors that can arise when working with very dilute samples. Here, SiMREPS could overcome potential errors given its direct detection which has shown to be highly specific (99.99999%) and capable of detecting analytes as low as 1 fM and would later achieve attomolar sensity [53,146].
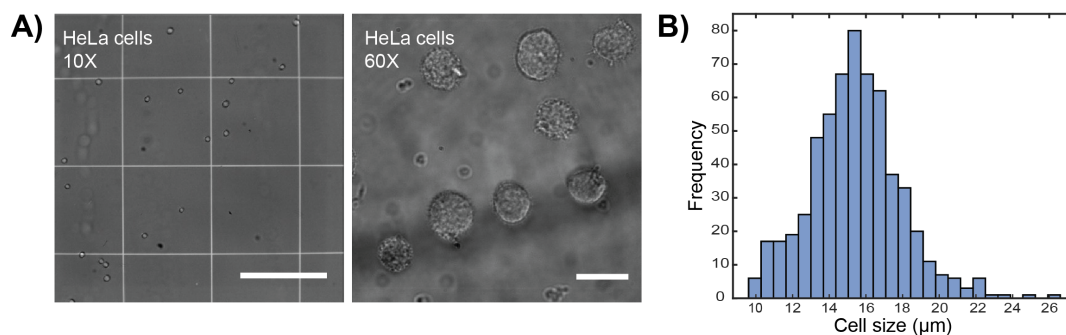
Figure 3-5 Size characterization of HeLa cells. A) HeLa cells analyzed under 10× and 60× magnification. Scale bars are 250 μm and 20 μm, respectively. B) Histogram of cell diameter size extracted from images of HeLa cells.

Before processing cells through the C1 platform, there is a certain procedure to be performed as described in **Section 3.3.3**. First, we had to investigate which IFC was appropriate

for our cells. Our HeLa cells were analyzed under magnification 10× and 60× (**Figure 3-5**) to measure the average diameter of the cells. Based on our analysis, we observed most cells had a diameter around 16 microns leading to our selection of the large IFC (17-25 µm) for efficient capture. Following this, a quality check was performed on lysis reagents to ensure that proper and efficient lysis would take place within the microfluidic chamber. After testing the cells with 3 different lysis mixtures (**Figure 3-6**) described in **Section 3.3.2**, we found that Lysis Mix#1 (Single Cell-to-CT Lysis Buffer, C1 Lysis Plus Reagent, C1 DNA Dilution Reagent) performed efficiently. The lysis was also tested across different time points and 5 minutes was enough to lyse cells (see **Appendix Figure 6**). After this reagent optimization was completed, HeLa cells were processed in the C1 machine and an observed capture near 90% was achieved (**Figure 3-7**). These lysed cells were transferred to PCR tubes for subsequent analysis via SiMREPS.
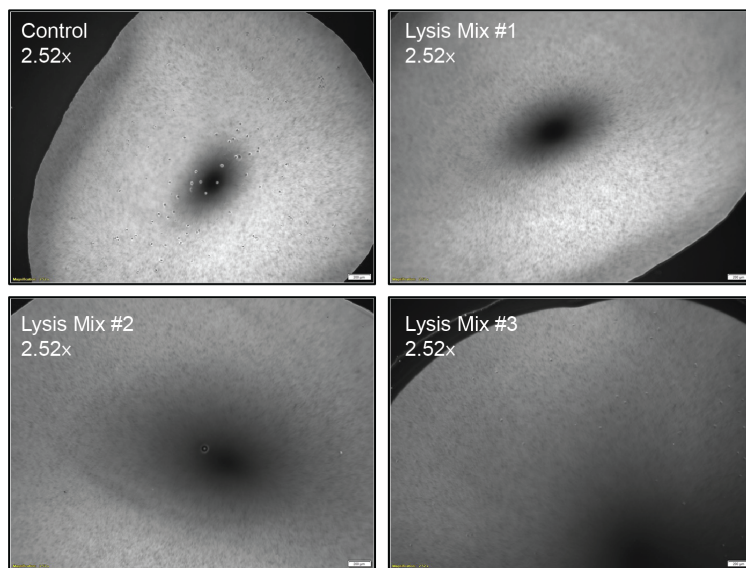
Figure 3-6 Cell lysis optimization. Images of HeLa cells at 2.52 magnification before (top left) and after lysis. Scale bars are 200 µm.
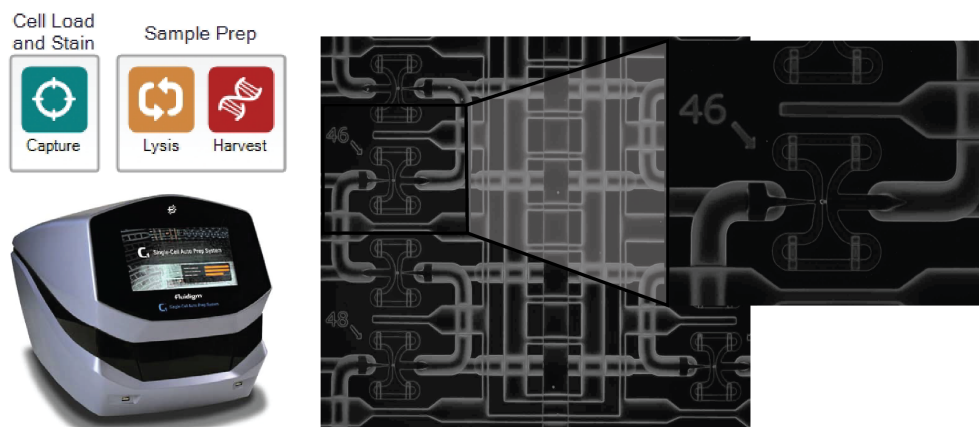
Figure 3-7 Fluidigm C1 system and script utilized for processing HeLa cells [150]. Single HeLa cells were captured efficiently as depicted by the photo of wells of the IFC. A zoomed in view of well 46 shows a captured cell.

3.4.2 Accelerate Data Acquisition through Optimization Conditions

In parallel, we focused on optimization to increase sensitivity considering the single cell lysate sample volume led to a highly diluted sample. The first optimization performed was similar to the probe optimization presented in **Section 2.4**. Here, we utilized the cut pipette tip well setup and spiked-in 400 fM of let-7a. We attempted to increase the N_{b+d} in order to have a very distinct separation from background allowing for a trade-off for lower acquisition time. To achieve the increase of N_{b+d}, the samples were imaged across a set of temperatures. The temperatures investigated were: 23 °C, 24 °C, 25 °C, 27 °C. As seen previously, the increase in temperature resulted in a higher N_{b+d} (**Figure 3-8A,C**). The temperature also influenced the bound time which decreased from 6 seconds down to 2 seconds (**Figure 3-8B, Appendix Figure 7A**). Correspondingly, the k_{off} increased from 1.47×10^{-1} s^{-1} to 4.59×10^{-1} s^{-1} (see **Appendix Figure 8**A).
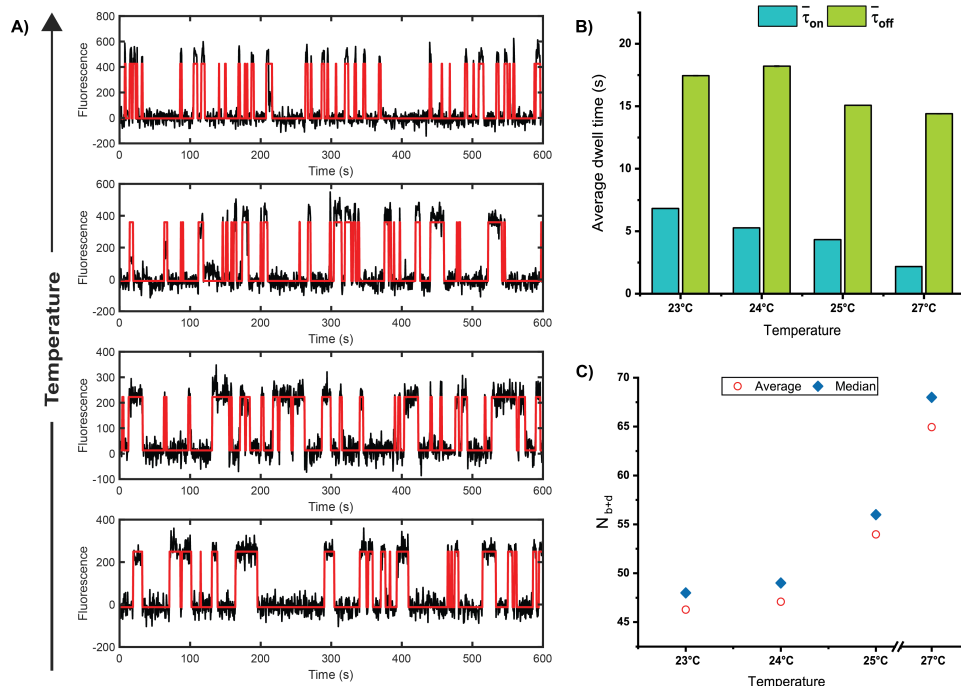
Figure 3-8 Effects of temperature on the detector probe for detecting 400 fM of spiked in let-7a. A) Representative single-molecule traces (black) with an idealized HMM fit (red) as temperature increase, bottom to top. B) The average dwell times the detector probe spent in the bound ($\bar{\tau}_{on}$)(teal) and unbound state ($\bar{\tau}_{off}$)(green) across different temperatures. C) The average and median N_{b+d} exhibited by the detector probe as temperature increased.

Another parameter that displays a similar outcome is the increase of concentration. Contrary to the *in situ* detection, there would not be a significant impact on SN since after target is captured, the sample well is washed, removing biomaterial. SiMREPS works by measuring a kinetic fingerprint, produced by a detector probe. To ensure effective readout, a surplus of detector probe is utilized. The high concentration results in constant replenishment, and, therefore, the detector probe can be captured for extended periods of time. In addition, if the concentration is further increased, the replenishment would occur at a faster rate and the detector probe signal would exhibit more binding and unbinding events. Overall, the average dwell times and rate constants were very similar to those observed in the samples utilizing 25 nM FP. The N_{b+d} increased by 10-20 more events of binding and unbinding events, however, the N_{b+d} distributions were wider for 50 nM probe (**Figure 3-9**) and since the kinetics were similar there

was no justification to move towards its application. All data collected on samples utilizing 50 nM can be found in **Appendix Figure 7B** and **Appendix Figure 8**.
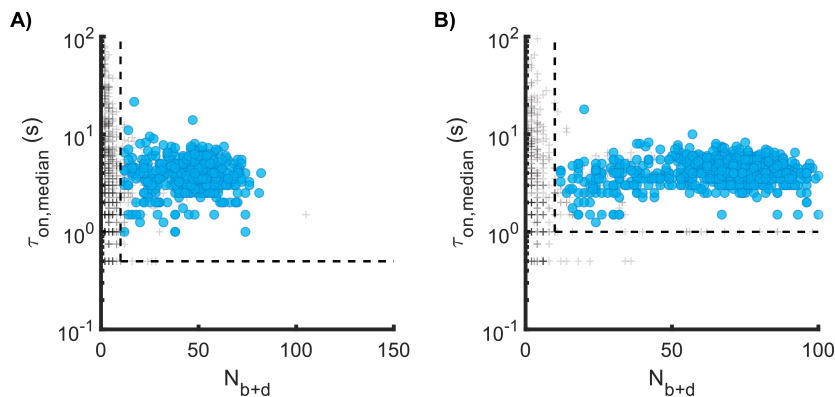
Figure 3-9 Plots of kinetic parameters used to identify let-7a molecules based on their kinetic fingerprints. Plots are generated from one representative movie from each condition, A) 25 nM FP, 24 °C and B) 50 nM nM, 24 °C, after applying thresholds for fluorescence intensity, signal-to-noise, and median bound and unbound dwell times. Each blue circle represents an individual accepted candidate molecule, plotted by its median bound dwell time ($\tau_{on,median}$) and number of binding and dissociation events (N_{b+d}) during a 10 min observation.

In summary, utilizing 25 nM FP across increasing temperatures resulted in a higher N_{b+d}. From this analysis, it was hypothesized that imaging at 5 min was already possible since the N_{b+d} range was between 45-70 events vs an average of 37 events seen at 21-22 °C. To check whether lowering the acquisition by half was attainable, a theoretical analysis was performed. The theoretical analysis consisted of analyzing different lengths of the raw data to determine the feasibility of decreasing acquisition time.
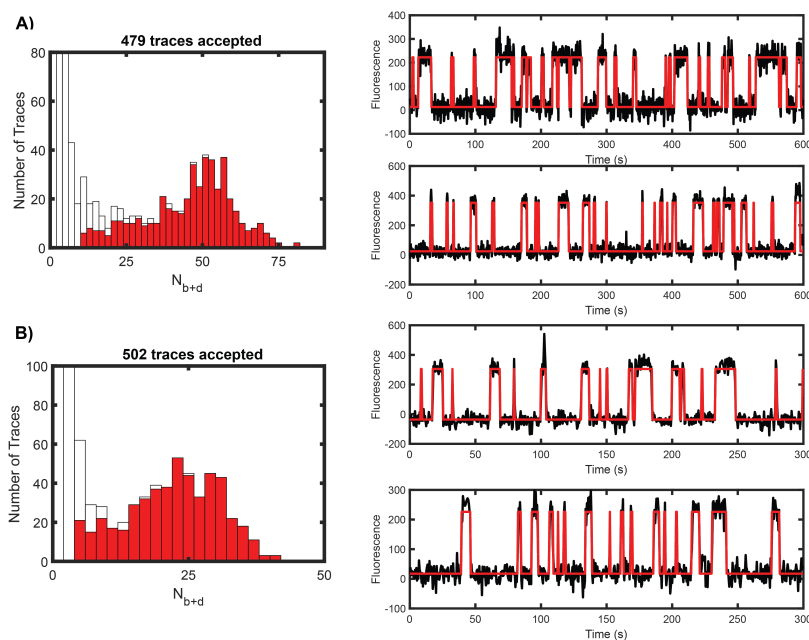
Figure 3-10 Theoretical analysis of a 10 min movie. The movie was acquired at 500 ms for 1200 frames. A) Histograms (left) of the number of accepted candidate molecules (red) per FOV showing the number of binding and dissociation events after application of thresholds for fluorescence intensity, signal-to-noise, and median bound and unbound dwell times for the given condition. On the right, representative single-molecule kinetic traces for molecules passing the thresholds applied. B) The same FOV was analyzed for only 600 frames of those collected in the raw movie. Histograms of the number of candidate molecules per that same FOV showing the N_{b+d}. Representative traces extracted from the 600-frame analysis after applying the same thresholds except that of N_{b+d} as half the movie was analyzed.

The theoretical analysis that was performed observed the positive target readout by analyzing the first 600 frames of the raw data acquired at 24 °C. The sample was arbitrarily chosen to perform the analysis. From this analysis, we were able to confirm that imaging 600 frames at exposure of 500 ms accepted a significant number of traces in comparison to the full analysis and would allow the acquisition time to decrease to 5 min (**Figure 3-10**).
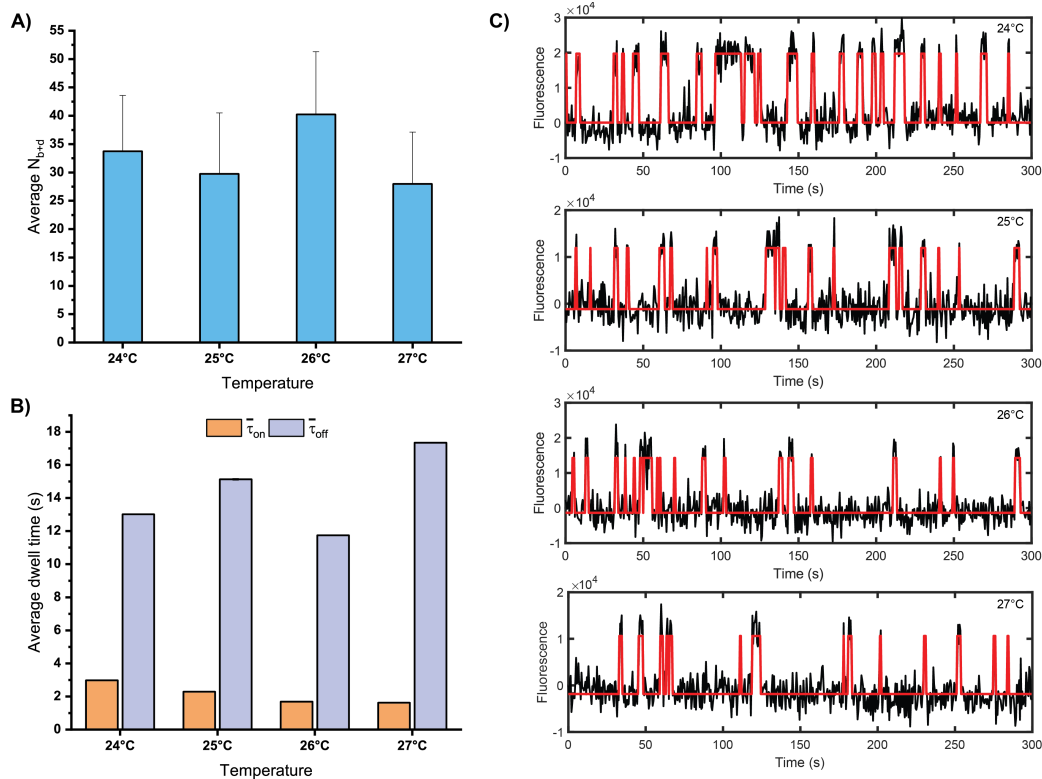
Figure 3-11 Analysis of 5 min (500 ms, 600 frames) movies across temperatures 24 °C, 25 °C, 26 °C, 27 °C. A) Number of binding and dissociation events per temperature. N_{b+d} values were extracted from positive traces. B) The average dwell times the detector probe spent in the bound ($\overline{\tau}_{on}$)(teal) and unbound state ($\overline{\tau}_{off}$)(green) across different temperatures. C) Representative single-molecule traces (black) with an idealized HMM fit (red) extracted from each temperature condition.
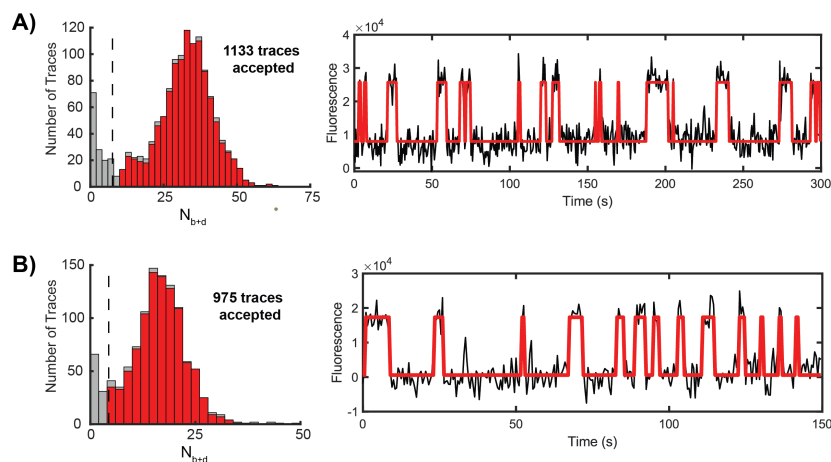
Figure 3-12 Theoretical analysis of a 5 min movie. The movie was acquired at 500 ms for 600 frames. A) Histograms (left) of the number of accepted candidate molecules (red) per FOV showing the number of binding and dissociation events after application of thresholds for fluorescence intensity, signal-to-noise, and median bound and unbound dwell times for the given condition. On the right, representative single-molecule kinetic traces for molecules passing the thresholds applied. B) The same FOV was analyzed for only 300 frames of those collected in the raw movie. Histograms of the number of candidate molecules per that same FOV showing the N_{b+d}.

Representative traces extracted from the 300-frame analysis after applying the same thresholds except that of N_{b+d} as half the movie was analyzed.

Following this, a set of samples were spiked in with 400 fM and imaged for a 5 min period, 600 frames with an exposure time of 500 ms, at different temperatures: 24 °C, 25 °C, 26 °C, 27 °C. It was confirmed that detection of let-7a was as efficient when acquisition time was reduced by half. This was possible due to the increase in the number of binding and dissociation events achieved with the increase in temperature seen for the data acquisition of 1200 frames at 500 ms exposure time (**Figure 3-8**). Contrary to the acquisition of 1200 frames, this set of data did not have a significant change in N_{b+d} across temperatures (**Figure 3-11A**). It was also found that as the temperature increased, there was an increase in the average unbound dwell time (**Figure 3-11C**, **Appendix Figure 9**). This behavior was apparent in the representative traces for each condition (**Figure 3-11B**). From this, we deduced that utilizing 24 °C as the experiment temperature would be appropriate as there was still an average N_{b+d} of 33 events and the average unbound time was the lowest at 13 seconds in comparison to 17 seconds for 27 °C. This set of behaviors would allow for further decrease in acquisition. As such, we further analyzed the data taken at 24 °C by observing the first 300 frames. Here, it was confirmed that this condition might work for the detection of let-7a based on the observation of similar amounts of captured target between the original and theoretical analysis (**Figure 3-12**). This prompted the experimental investigation utilizing a 500 ms exposure time and imaging for 300 frames. As seen for the theoretical analysis, there was successful detection and the acquisition time had been reduced by half again. Upon deeper analysis of the accepted traces, the N_{b+d} was decreasing as expected, however, in combination with unbound events there could be issues in decreasing the acquisition further. The increase in unbound events and decrease in N_{b+d}, could affect the ability to distinguish targets above background. To alleviate the potential problem, the exposure time was

altered. As seen in **Figure 3-8**, as the temperature increased, the traces depicted sharper peaks that indicate a decrease in the bound time. This was confirmed by fitting the bound dwell times, which showed a decreased average bound dwell time. The investigation of a lower exposure time would enhance the resolution of the "peaks". To test the theory, the following conditions were tested and compared: 1) 600 frames, 500 ms 2) 300 frames, 500 ms 3) 600 frames, 250 ms 4) 300 frames, 250 ms (**Figure 3-13**). From this data, we gathered a successful detection when imaging at 250 ms for 600 frames. For the last condition, imaging 300 frames at 250 ms exposure time, the accepted counts were significantly lower across two experiments so we removed this condition. Also, the average N_{b+d} extracted was even lower (**Figure 3-13D**) than that seen for imaging 300 frames at 500 ms exposure time which could pose a problem as it lowered the confidence of detection against background. From this analysis, the samples imaged at 250 ms for 600 frames were selected as most suitable given a higher N_{b+d} than the other conditions, and since they reduced the imaging time to 2.5 min per FOV. Overall, we found that carrying out experiments at 24 °C with a fluorescent probe concentration of 25 nM imaged at 600 frames with exposure time 250 ms was suitable for future experiments. This optimization led us to decrease our acquisition time by 4-fold. The decreased acquisition time would allow for multiple FOVs to be recorded from a sample which would allow for potential improvements of LOD by permitting detection of additional targets in the extra FOVs.
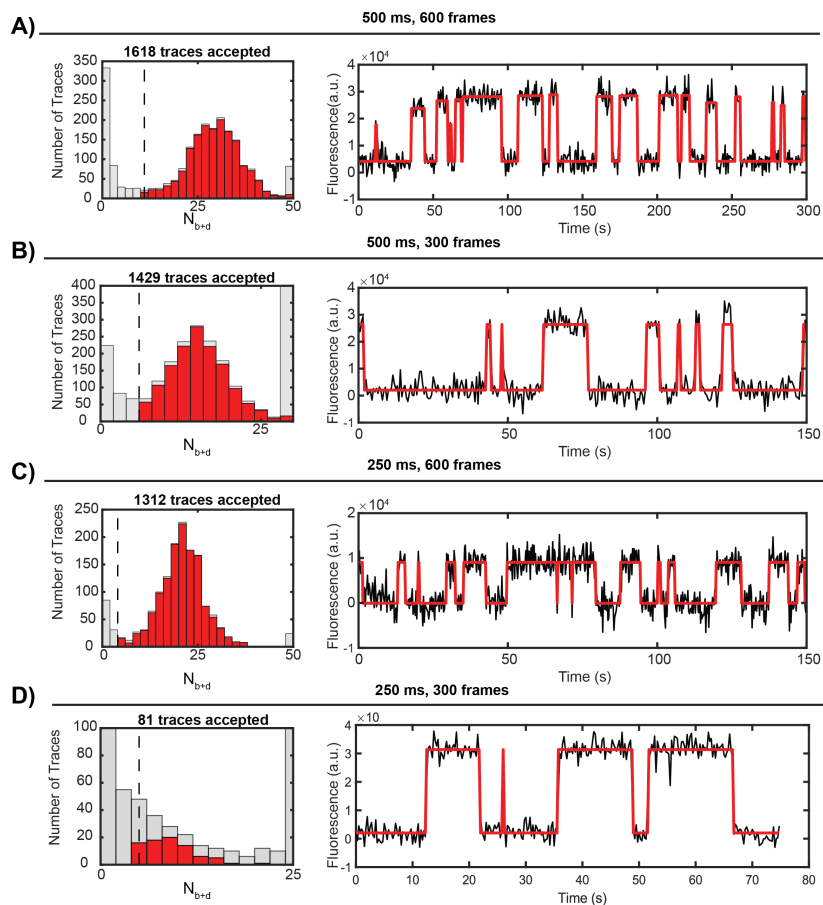
Figure 3-13 Evaluation of kinetic fingerprints in different imaging conditions. A-D) Histograms (left) of the number of accepted candidate molecules (red) per FOV showing the number of binding and dissociation events after application of thresholds for fluorescence intensity, signal-to-noise, and median bound and unbound dwell times for the given condition. On the right, a representative single-molecule kinetic traces for molecules passing the thresholds applied.

3.4.3 Sensitivity Improvement by Multiple FOV Data Collection

The capability of recording multiple FOVs led to an optimization of sample well area size. The classical SiMREPS experimental well setup utilizes a cut pipette tip with a diameter of ~5mm (5,000 µm). With the knowledge that one FOV is 120 µm x120 µm, we could calculate a theoretical number of FOVs a well had. The initial idea was to calculate the full area of a circle using the diameter size and then dividing by the full area of a FOV. However, this would not be entirely true as the edges of a circle are round and, therefore, the squares in the corners would

only record a section of the capture surface. To obtain a more accurate estimation, we utilized the Pythagorean theorem to find the size of a square that would fit within a circle (**Figure 3-14A**). Here, we could then figure out how many FOVs fit within this area and obtain a closer estimation to the true value. In **Figure 3-14A**, a calculation for a well with diameter 500 μm was investigated. With the Pythagorean theorem, we found that the length and width of that square was 353 μm. Again, if we found the area of the square and divided by the area of a single FOV, we would estimate 6 FOVs are available to image. However, if instead we divided the FOV length from the length of the side of the square we would get 2.6 FOVs to image meaning only 2 FOV could be imaged in one length. By multiplying that by the other amount of FOVs available on the other length we would find only 4 FOVs were able to be processed while the remaining potential FOVs (red) would not fully capture the FOV and can lead to misrepresentation as these FOVs may not be identical across wells (**Figure 3-14B**).
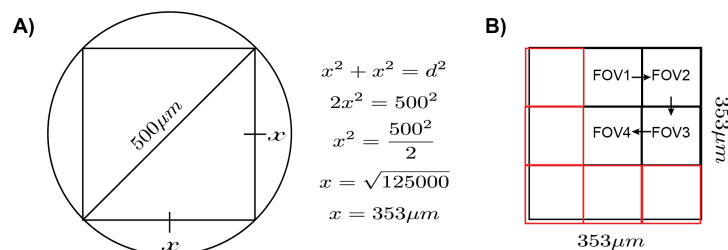
Figure 3-14 Depiction of mathematical approach to identify possible FOVs within a sample well. A) Surface area analysis of a square utilizing the Pythagorean theorem. B) Schematic showing how FOVs were selected (black) and those that did not fit the size criteria (red).

As mentioned, the diameter of our cut-pipette tip wells is 5 mm and the surface area would be approximately 3500 μm x 3500 μm, so to scan through every FOV it would require approximately 28 h to analyze only one sample. The solution for this potential problem could be alleviated by adjusting the surface area similarly to utilizing O-TIRF vs P-TIRF. P-TIRF utilizes a flow sample cell that is essentially a sandwiched microscope slide and glass coverslip resulting in a large surface area and as target is flowed in, the molecules can disperse into this larger area

and therefore reduce the density per FOV. O-TIRF, on the other hand, uses wells that minimizes the surface area and allow for an increase in sample volume, if needed. The decrease in surface area would reduce the amount of area a target can be captured in meaning the smaller the area, the higher the occupancy. This increase in sensitivity due to higher occupancy and, therefore, higher accepted counts would increase our confidence as it would result in a higher resolution allowing us to detect much lower concentrations. As such, we investigated the available area, theoretical FOVs, a well with smaller diameters had. We selected the use of 500 μm (0.5 mm), 800 μm (0.8 mm), 1200 μm (1.2 mm) and 5000 μm (5 mm). **Table 3-3** shows the theoretical FOVs and total acquisition time needed to image a full sample well.

Table 3-3 Theoretical analysis of available FOVs within wells with different diameters.

Well diameter (μm)	Surface area (μm × μm)	Theoretical FOVs	Total acquisition time (min)
500	353 × 353	4	10
800	565 × 565	16	40
1200	848 × 848	36	90
5000	3535 × 3535	680	1700

From this theoretical analysis, a sample well at or below 1.2 mm could be a potential alternative for our experimental setting. We selected to start investigation with the 500 μm well in which we could decrease our sample volume from 100 μL to 10 μL. After running multiple samples, it was deduced that we could only image up to 3 FOVs, but the density of captured molecules significantly increased by around 10-fold (**Figure 3-15A**). Although the well had an increase, there was the potential problem of only obtaining 2 FOVs. Following this, the 1.2 mm well was investigated and 25 FOVs were available. Utilizing the 1.2 mm, we found a 4-fold increase per FOV in comparison to 5 mm (**Figure 3-15A**). As expected, as the well and surface area and sample volume decreased, the capture density increased. From this set of data, the 1.2 mm well was selected for further experimentation and 10 FOVs would be imaged. The reason being that it required 30 min to image one sample and higher sensitivity could already be

achieved as 10 FOVs could account for ~2,000 molecules while only ~1,500 and ~500 for the 0.5 mm and 5 mm wells, respectively. This estimation was made based on the average accepted counts per FOV depicted in **Figure 3-15**. Pursuing this alternate approach resulted in a 2-fold increase in sensitivity.
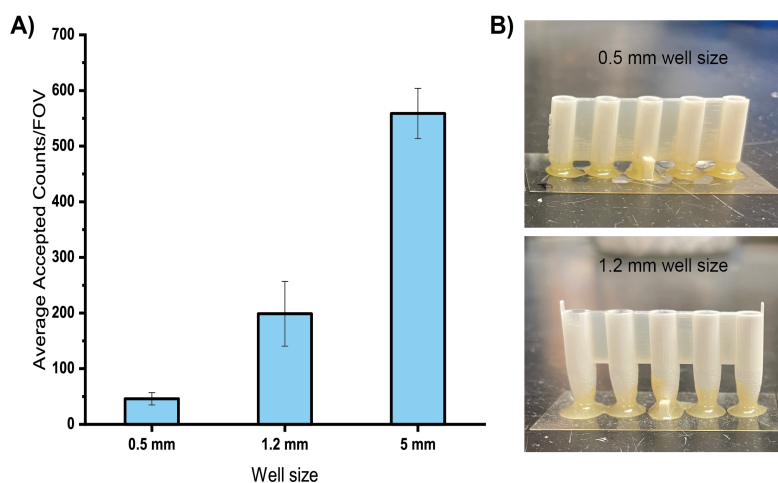
Figure 3-15 Effect of surface capture area and sample volume on capture efficiency. A) Average accepted counts obtained for a FOV across different well sizes. B) 3-D printed well strips of 0.5 mm and 1.2 mm.

3.4.4 ATPS-Mediated Enrichment

Contrary to *in situ* detection, we are now presented with the issue of diffusion given the molecules are in free solution. Since the sample of interest is very dilute and SiMREPS being a surface-based assay, we had to find a solution for the issue of limited capture due to slow mass transport. The final piece in our puzzle was to apply an aqueous two-phase system. While this project was in progress, an ATPS system was in development in the Walter lab focused on circulating tumor DNA (ctDNA) detection. Preliminary testing showed LODs may be reduced by a factor of ~50 which could benefit in single cell lysate detection.

ATPS is utilized for the purification of biomolecules through phase separation. In order to achieve two distinct phases, a certain composition is required and can be found by determining the binodal curve. As mentioned in **Section 3.3.4**, we employed an ATPS composed of PEG, sodium citrate and sodium chloride (NaCl) which has shown to enhance partitioning of nucleic

acids [146,151]. The particular composition of the ATPS used was 37.7% PEG, 2% sodium citrate and 2.8 wt % NaCl as it was shown to be successful in enriching EGFR exon 19 deletion mutation [146]. Different concentrations of the components will result in different droplet or, in this case, salt-rich phase size. The ability to manipulate the size ensured the ATPS could be applied in different well sizes. Additionally, this composition yielded a particular volume of salt-rich phase capable of covering the whole surface area of capture within the 1.2 mm well.
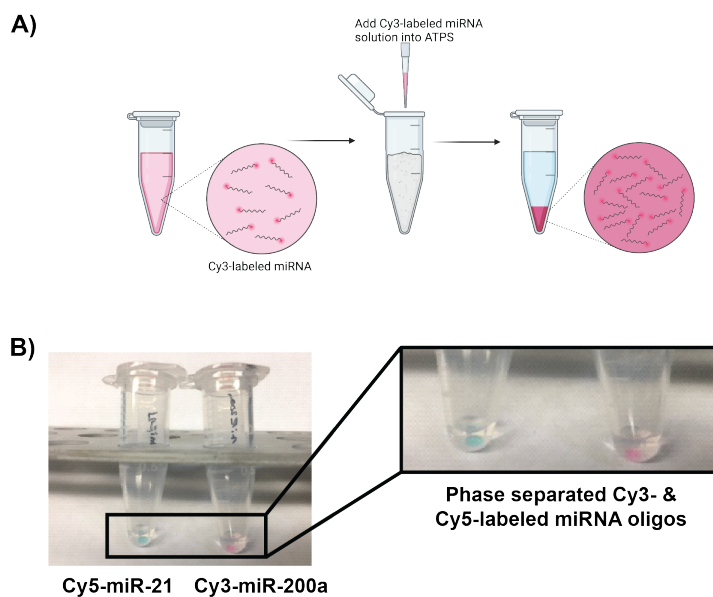
Figure 3-16 A) Schematic of the enrichment of Cy3-labeled miRNA into a smaller volume after being introduced into an ATPS lyophilized aliquot. B) Photos depicting the enrichment of two dye-labeled miRNA into a smaller volume, a salt-rich phase. A zoomed view is presented on the right showing salt phase droplets with dye-labeled miRNA.

To test the application of the ATPS for miRNA enrichment, we tested the partitioning of Cy3- and Cy5-labeled miRNA when added to the ATPS as depicted in **Figure 3-16**. Utilizing a dye-labeled molecule would permit for a quick visual screening of the partitioning within the ATPS. The higher the intensity of the dye in one phase versus the other indicated a stronger and preferred partitioning into that phase. Here, dye-labeled miRNAs were introduced into a respective ATPS aliquot. After mixing the solution and centrifuging, a clear separation between

the dye-labeled miRNA was reconcentrated into the salt-rich phase as achieved for DNA [146]. To better understand the effect the partition had on the concentration of miRNA, we investigated the salt-rich phase by UV-Vis spectroscopy. Similar to the addition of dye-labeled miRNA, here, an input of a known let-7a target concentration (0.5, 1 and 5 μM) was introduced into a lyophilized ATPS aliquot, rigorously vortexed, centrifuged and then the salt-rich phase was analyzed. The absorbance of the samples were measured and then were compared before addition and after addition into the ATPS. As expected, based on our initial test (**Figure 3-17**), the concentration of the target within the salt phase was significantly higher than the concentration added (referred to as the feed concentration) (**Figure 3-17**). The increase in concentration was depicted as an enrichment factor that was calculated by dividing the concentration achieved with ATPS by the feed concentration as seen in Zi *et al*. [146]. An enrichment factor of 14 was obtained for let-7a (**Figure 3-17B**). A subsequent experiment investigated a wider range that reached lower concentrations was examined and showed enrichment could be achieved to the same degree as seen in higher concentrations (**Figure 3-17C**). As for Chapter 2, the investigation of a panel of miRNAs is highly beneficial in better understanding pathways of cellular function so we tested the ATPS for another miRNA, miR-16. As shown in **Figure 3-16D**, a similar enrichment factor was achieved which also informed that a difference in sequence did not alter the results.
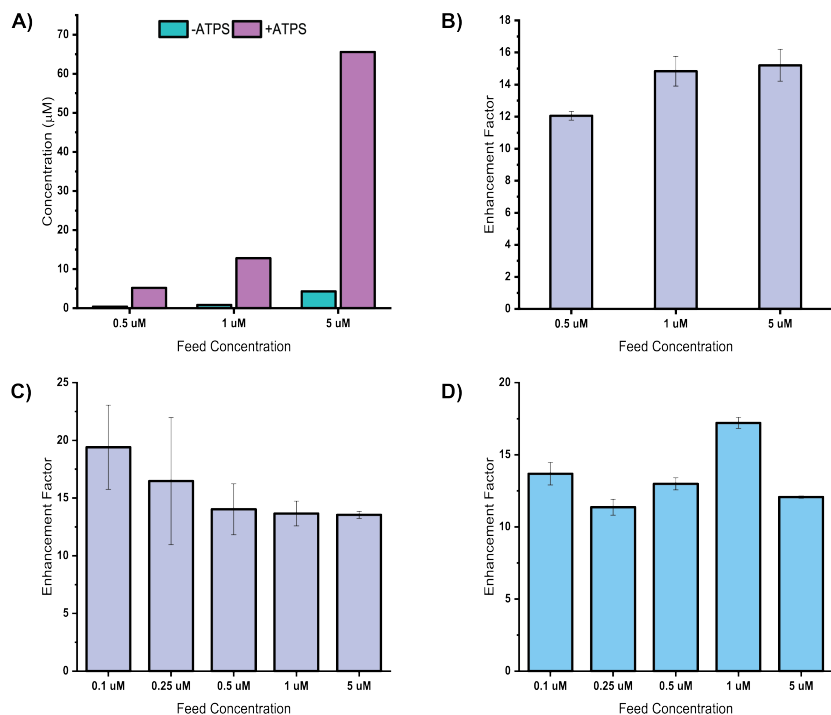
Figure 3-17 Quantification of enhancement after ATPS reconcentration via UV-Vis. A) Comparison between starting nucleic acid (0.5 µM, 1 µM, 5 µM let-7a) and addition into the ATPS (feed concentration). B) Enrichment factor corresponding to the data in panel A. C) Enrichment factor analysis investigating lower feed concentrations (0.5 µM, 1 µM, 5 µM) for let-7a. D) Analysis of enrichment for miR-16. Error bars represent the standard deviation of three independent measurements of the salt phase droplet.

3.4.5 Detection in Single Cells via ATPS-SiMREPS Assay

Next, we began to examine the capability of the ATPS to improve the sensitivity of miRNA detection. To test the effect of ATPS on miRNA enrichment on surface capture efficiency, we conducted a SiMREPS assay for let-7a detection utilizing the classical single probe detection scheme as shown in **Figure 3-18A**. The let-7a was captured via a LNA capture probe immobilized on the surface. A target sample was spiked-in with 100 fM of let-7a and was analyzed without ATPS. Another 100 fM target sample was prepared and was enriched by ATPS. A clear increase was observed with the application of ATPS vs without ATPS (**Figure 3-18**). This further confirmed that the ATPS improves reconcentration and therefore capture efficiency as the salt-rich phase is in direct contact with the capture surface facilitating mass transport of the target molecules.
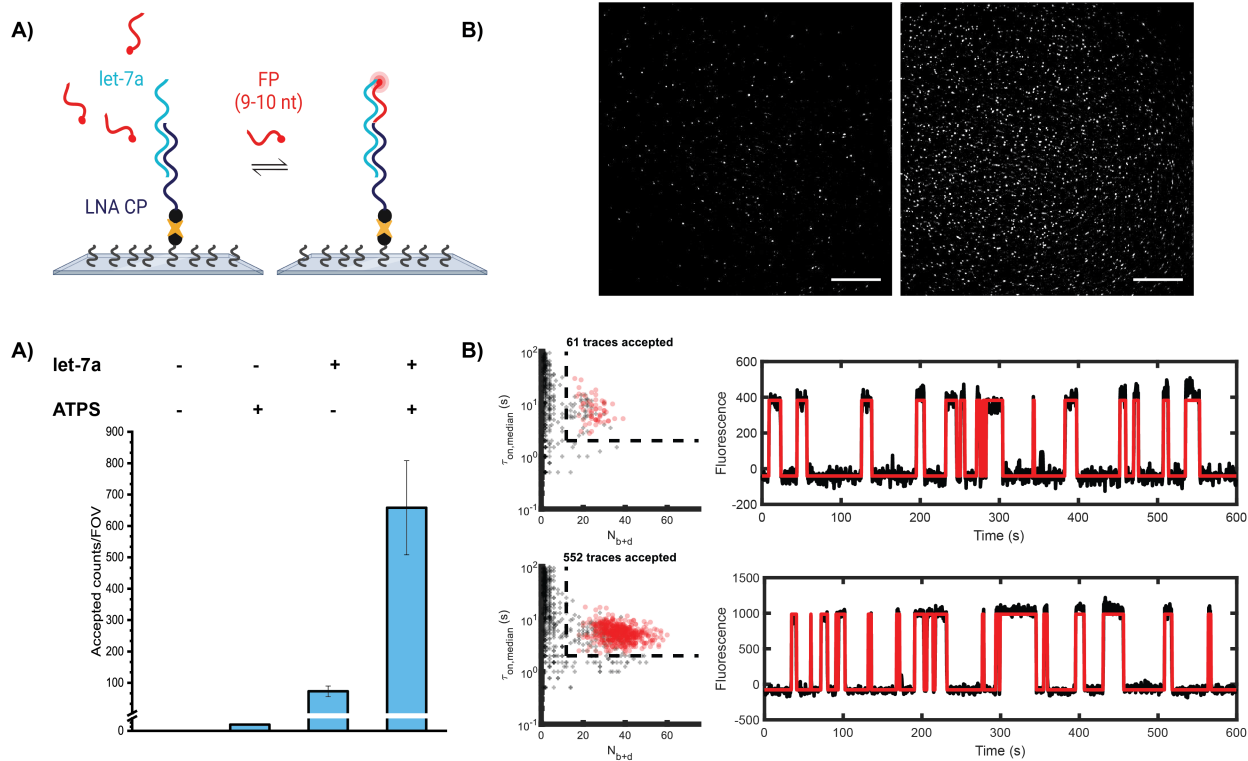
Figure 3-18 Quantification analysis of a SiMREPS experiment utilizing ATPS. A) Schematic depicting the SiMREPS approach for miRNA utilizing a single-color probe. B) Comparison of spot density captured candidate targets with (right) and without (left) the application of ATPS for a 100 fM let-7a sample. The images were obtained after performing intensity averaging on movies. The bright spots represent the transiently binding fluorescent probes. C) Comparison of accepted counts per FOV with and without enrichment by ATPS. The target concentration utilized was 100 fM. B) Plots of N_{b+d} and $\tau_{bound, median}$ and representative kinetic fingerprints for a FOV of a sample with (bottom) and without ATPS (top).

Next, we aimed to test the sensitivity of the ATPS-SiMREPS assay against our isolated single cell lysates. First, we worked on obtaining standard curves for the detection of let-7a in buffer with and without the application of ATPS. As expected, the concentration each target sample was higher in presence of ATPS. Here, an enrichment factor of ~7-fold was achieved when utilizing ATPS. This enrichment factor is close to the 10-fold factor achieved in the application for DNA. However, as shown by the error bars it is evident that there are some issues for the miRNA ATPS system. With respect to the system altogether, we hypothesized that the size of the target miRNA may have an effect on the partitioning coefficient. We revisited the data obtained in the early stages of optimization for the ATPS. There was a preliminary

experiment that tested the difference in partitioning based on oligonucleotide length. From these data, there was a slight increase in the partition coefficient from the 20-mer to 60-mer DNA oligonucleotides and an even more pronounce difference within the range of 8-mer to 20-mer. With respect to the partitioning observed within the 20-mer to 60-mer, the evidence was not conclusive, but worth mentioning. Due to our experimental work with ATPS in application to a short (21-22 nucleotides) oligonucleotide, we hypothesize that the length of our target may be causing the increase in error across different samples.
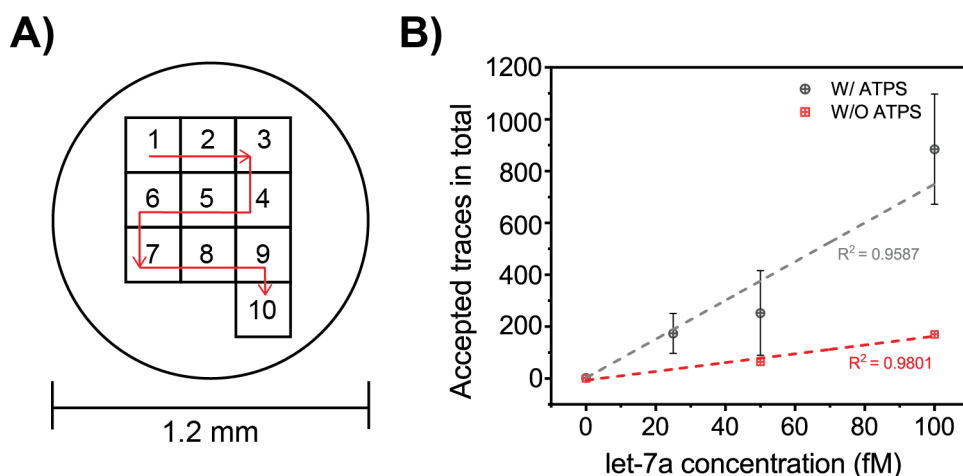
Figure 3-19 Quantification of varying concentrations of let-7a in a PBS buffer utilizing the multiple FOV data collection scheme. A) Multiple FOV data collection scheme for 1.2 mm diameter 3D-printed wells. A total of 10 FOVs were collected starting from the upper left corner of the sample well. The acquisition time for each FOV is 2.5 min. After moving to the next FOV, a 10 s delay was used to allow the autofocus system to establish focus before acquiring the next movie. B) Standard curve for let-7a in a buffer with (red) and without (black) an ATPS target enrichment step. Total counts obtained from 10 FOVs per sample were used for each measurement. An error-weighted linear regression (red and gray dashed lines) was fit to each standard curve with the y-intercept constrained to the mean counts of blank controls.

Despite the issue with consistency across the standard curve measurements, there is still a considerable increase in sensitivity and an estimation of relative counts to concentration for let-7a. Therefore, we set out to examine the performance of the ATPS-SiMREPS assay in detecting miRNA in the single cell lysates. As envisioned, we were able to observe repeated high- and low-fluorescence signal, typical of the SiMREPS single-probe behavior, during data acquisition

of a sample with a single lysed HeLa cell. After analysis was performed, we were able to see that

SiMREPS was capable of detecting analytes within a very diluted sample (**Figure 3-20D, E**).

This was possible due to the application of ATPS (**Figure 3-20C**). As shown in **Figure 3-20**, the

single cell captured in panel A was added in the ATPS after lysis and a comparable amount of

let-7a molecules were detected as opposed to the sample without any ATPS. This work further

illustrates the power of ATPS in increasing capture efficiency by enriching analytes into a

smaller sample volume.
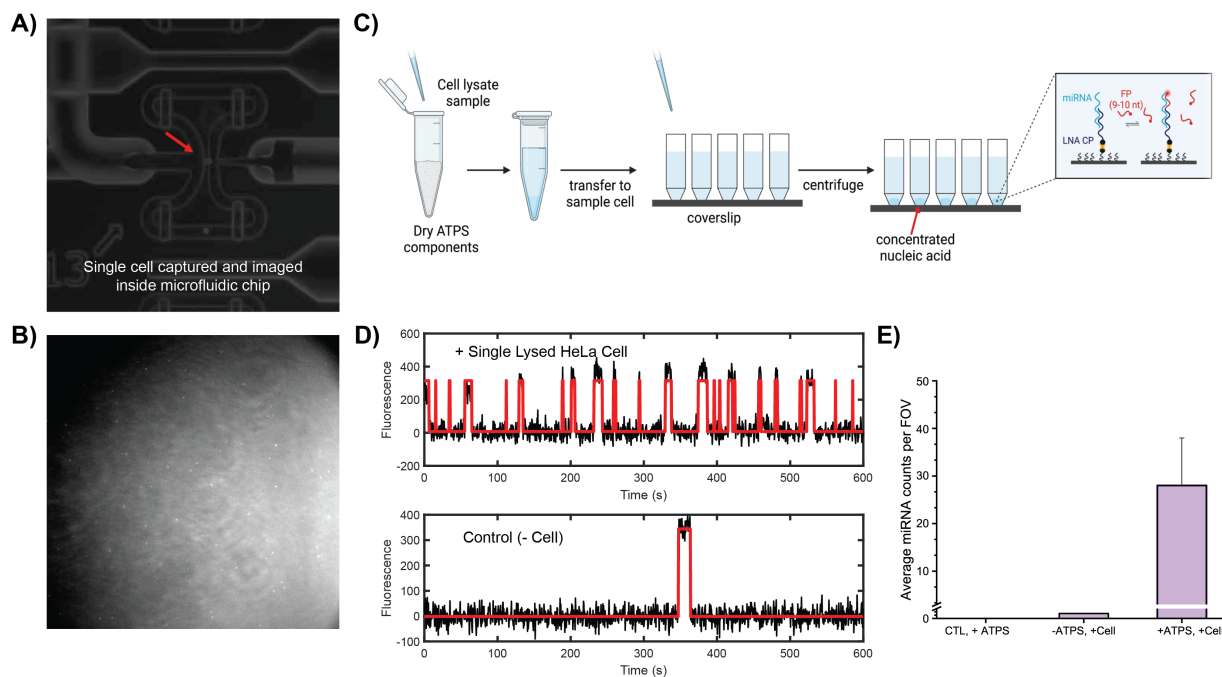
Figure 3-20 Quantification and validation of an assay for let-7a detection in a single HeLa cell lysate. A) Single cell isolated and captured within the Fluidigm C1 IFC. B) Single movie frame from a representative field of view from ATPS-SiMREPS using objective-type TIRF microscopy. C) Workflow of ATPS SiMREPS (Created using Biorender). A cell lysate is introduced into ATPS and then transferred to a sample well. The coverslip with sample wells is centrifuged and a salt-rich phase forms on the surface capture area allowing for detection via a single-probe scheme. D) Single-molecule trace extracted from imaging of HeLa cell and control sample E) Representation of miRNA detection enhancement when utilizing aqueous two-phase system.
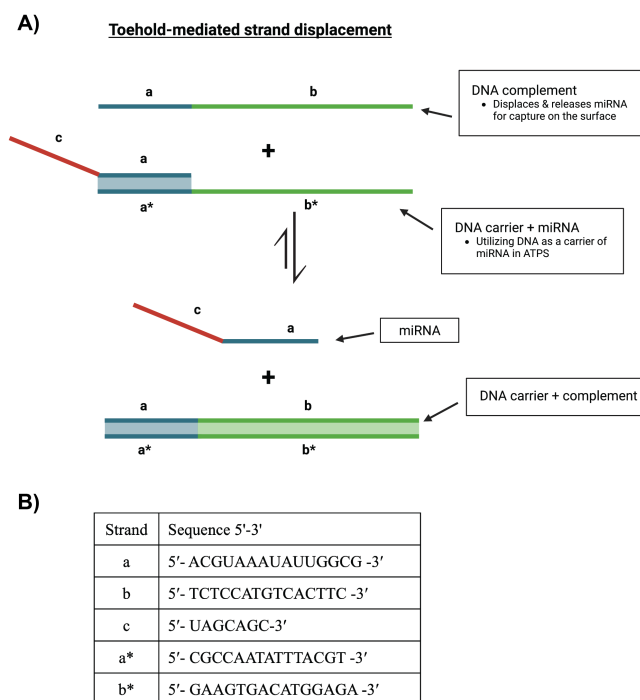
Figure 3-21 Toehold-mediated strand-displacement systems implemented in ATPS for miRNA enrichment. A) Schematic showing a toehold-mediated nucleic acid interaction. The two-strand complex has an exposed toehold domain b* that is complementary to the domain b in the input DNA complement. The input DNA complement binds to the complex and strand displacement through domains a and a* leads to release of an output miRNA is captured on the surface for kinetic fingerprinting. B) Table of strand sequences corresponding to the schematic for miR-16 application.

3.4.6 Toehold-Mediated Strand Displacement Approach

To further improve this assay, one approach is to optimize the ATPS for more effective partitioning for shorter oligonucleotides. Another approach is to figure out a way to keep the miRNA in the salt-rich phase without changes to the system. At the moment, the latter solution was pursued. With the knowledge that larger sizes had a higher partition coefficient and the success seen in Zi *et al.* for enrichment of a 160 bp DNA, we investigated the introduction of a DNA "carrier" for miRNA (**Figure 3-21A**). Since larger DNA partitioned effectively, we exploited Watson-Crick-Franklin pairing and hypothesized that if a DNA with complementarity to the miRNA was added to the ATPS, the pair would have a preferential partitioning to the salt-rich phase. A carrier system utilizing toehold-mediated strand displacement was designed for miR-16 (**Figure 3-21B**). Here, a 30-mer would be initially tested in which there would be

complementarity with a fraction of the miRNA target. The 30-mer DNA (referred to as DNA carrier) would be introduced to a sample with target and then added to ATPS (**Figure 3-22B**). The remaining non-complementary region would be accessible to the LNA capture probe. After incubation for capture, the remaining sample would be removed and a completely complementary strand (referred to as the DNA complement) to the DNA carrier would be introduced to displace the carrier from the miRNA and open it up for detection via SiMREPS. Before introducing this carrier system into the assay, an electrophoretic mobility shift assay was performed to test the ability of a toehold exchange (**Figure 3-22C**). As seen in the gel, miRNA in the presence of DNA carrier results in a shift supporting efficient pairing. This is also apparent when DNA carrier is mixed with the DNA complement. Upon addition of all 3 (miRNA, DNA carrier, and DNA complement), the miRNA is recovered, and a shift is still present supporting the strong binding between the DNA carrier and DNA complement.
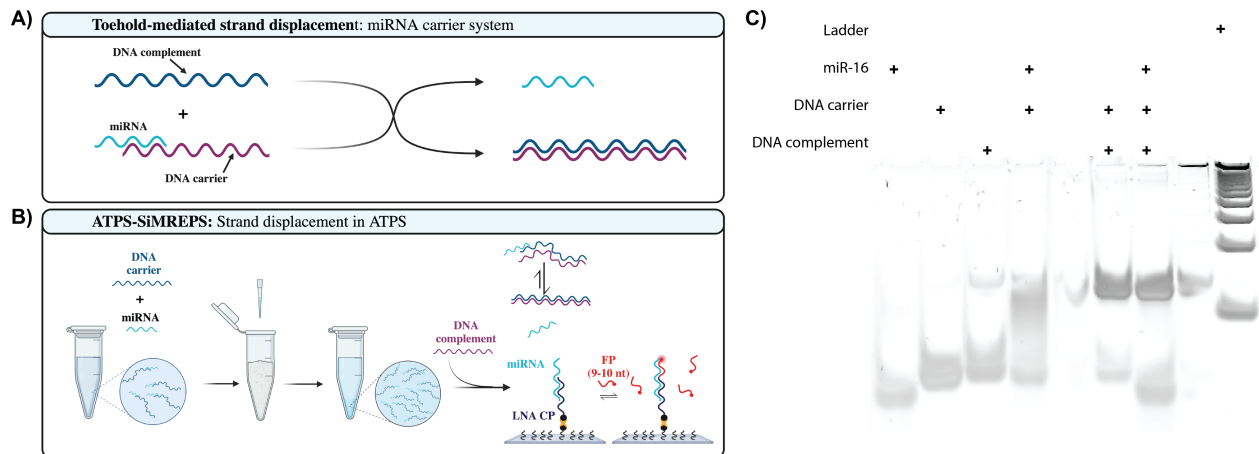
Figure 3-22 Carrier system for miRNA. A) Toehold-mediated strand displacement as a method to carry miRNA. The miRNA shares partial complementarity with the DNA carrier, while the DNA complement has full complementarity to the DNA carrier. Displacement occurs upon DNA complement addition. B) ATPS-SiMREPS schematic with the incorporation of the DNA carrier system. DNA carrier is added with miRNA into an ATPS lyophilized aliquot. The sample is then introduced into a sample well for SiMREPS analysis. The DNA complement is added to displace the DNA carrier and allow for miRNA capture and detection. C) Electrophoretic mobility shift assay to study the interaction between the miRNA, DNA carrier and DNA complement in different conditions.

Preliminary testing of the system has been investigated in the SiMREPS assay and although there was no pronounced effect in accepted counts and capture efficiency, the introduction of the DNA and DNA complement did not negatively affect the results. Additionally, there was speculation that in use of excess DNA complement, there may be an increase in background and therefore decrease in S/N due to the complementary region to the FP detection region. As observed from the FOVs and results of the observed counts, there was no significant change in background and therefore no effect on the number of accepted counts per FOV (**Figure 3-23**). Further optimization is necessary to test the efficiency of this application.
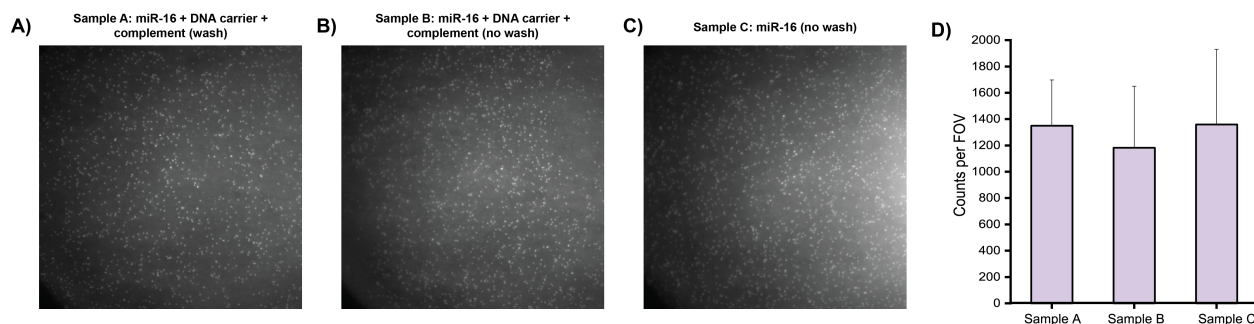
Figure 3-23 Effect of the toehold-mediated strand displacement (DNA carrier system) on miRNA detection. The DNA carrier and miRNA were added to ATPS, and then transferred to a well and incubated for one hour. A) A wash was performed on the wells and then the DNA complement was added in the FP imaging solution. B) No wash was performed. The DNA complement and the FP imaging was added after removal of sample from the well. C) A control sample was investigated. Only miR-16 was introduced to the ATPS system, followed by no wash, and finally introduction of the FP imaging solution.

3.5 Summary and Future Directions

In this chapter, we have shown the successful development and optimization of a workflow capable of isolation and lysis of HeLa cells followed by subsequent detection and quantification of let-7a by kinetic fingerprinting using a single fluorescently labeled probe following surface capture assisted by an aqueous two-phase system (ATPS). We demonstrated the ATPS-enhanced surface capture also extended to miRNA and thus were able to reconcentrate the lysate (which is necessarily diluted in the Fluidigm system) into the smaller salt-rich phase

increasing capture efficiency compared to the slow mass transport in the absence of the system. In addition to the optimized sensitivity via the use of ATPS, a set of experimental conditions were investigated and found to promote a further enhancement of in sensitivity by decreasing the acquisition time by 4-fold and therefore allowing for a larger surface area to be scanned. While utilizing a different sample cell setup resulted in a 2-fold increase by optimizing the capture surface area and sample volume to obtain a higher density of molecules in a smaller surface area and therefore increase the amount of captured molecules. Using these combined efforts, we have demonstrated detection of single miRNAs from a single lysed HeLa cell.

This assay could be further improved by facilitating the transport of miRNA. Further development includes investigation of the ATPS system in application to the enrichment of miRNA. Since miRNA is relatively smaller to the 160 bp DNA molecules successfully enriched in Zi *et al.*, we hypothesized that the miRNA has a different partition coefficient. To alleviate this, we are currently investigating a carrier system utilizing a toehold exchange mechanism. Since larger nucleic acids partitioned very favorably to the salt-rich phase, we are utilizing this knowledge and manipulating Watson-Crick-Franklin base pairing to use a larger sized DNA strand to bind and help "carry" the miRNA into the salt phase for capture efficiency to stabilize and/or improve. After this step is optimized, we plan to retest the sensitivity of our ATPS-enhanced SiMREPS assay by obtaining standard curves and then continuing the analysis of the remaining single cell lysates.

Another possible route to improve the assay is by combining SiMREPS with a different microfluidic chip. A microfluidic system for solid-phase RNA capture on a glass coverslip or polymer beads was developed by the Sims group [152,153]. This device, in comparison to other

microfluidic systems, fabricates a microwell array on top of a glass coverslip and isolates and traps single cells into individual chambers. The coverslip (or beads) is functionalized with oligo(dT) primers that permit mRNA capture of the single cells. Contrary to the Fluidigm IFC, the cells do not require a harvesting step and instead TIRF can be directly applied removing the need of reconcentration with ATPS. Additionally, if the beads are employed, both miRNA and mRNA expression profiles can be investigated.

With further development, we can apply either of these approaches to circulating tumor cells to investigate its application in studying profiling and its effect on cell state and fate.

Chapter 4 Conclusions and Future Directions

4.1 Overview and Summary of Dissertation

Over the past decades, advancements in microscopy have enabled the investigation of single molecules. As a result, this has given researchers the opportunity to tackle problems affecting the quality of life. The ability to observe the microscopic world to the single molecule level helps uncover biomarker expression levels and permits the profiling of genetic compositions to gain a better understanding of diseased states. Overall, measurement of single molecules circumvents traditional bulk analysis and allows for exploration of heterogeneity. This is particularly important when it comes to the understanding the seeding and survival of cancer.

Cancer is a pervasive disease that has affected the lives of many. It is known that metastasis occurs from seeding of CTCs. Previously, it was accepted that CTC enumeration sufficed in diagnosis [12]. Now with advances in science, current technologies like PCR [44–49], hybridization-based techniques [45,47] and NGS [45] allow for nucleic acid detection. Techniques that utilize amplification, like PCR and NGS, to increase the concentrations of targets for detection have high sensitivity. However, PCR-based methods are accompanied by bias in amplification as well as reverse transcriptases and ligases which can result in differences in expressions and/or completely dilute certain sequences due to replication errors and/or primer mismatches. While hybridization techniques, although amplification-free and low in cost compared to other profiling methods, they encounter problems with specificity due to the nature of hybridization thermodynamics. SiMREPS addresses the drawbacks of these existing

technologies. It is an amplification-free technique that does not require nucleic acid isolation. It manipulates the binding and dissociation of a detector probe to exhibit a certain signal pattern, kinetic fingerprint, in presence and absence of a target on surface. This simple set-up lends itself to the application for detection of multiple analytes such as ctDNA, proteins and miRNA among others. It overcomes binding thermodynamics by employing a transient hybridization approach which has shown to distinguish between SNVs.

With the need to obtain a more detailed analysis at the single-cell and single-molecule level, the high sensitivity of SiMREPS allowed for the development of a suitable assay. Through the work described in this dissertation, we have established a proof of concept demonstrating the assay's ability to detect miRNA with the potential to achieve better resolution to elucidate growth pathways, cell fate, and responses to environmental stimuli that cells exhibit to survive.

Chapter 2 focused on the development of an assay workflow utilizing *in situ* hybridization with a SiMREPS detection scheme. This assay design would permit quantification as well as conservation of spatial expression of miRNAs for diagnostics and biological information. This approach would also overcome limitations with yield since it does not require cell lysis and RNA extraction. In addition, SiMREPS would no longer be just a surface-based method, another advancement of this technology. In this chapter, let-7a FRET probe pair design requirements were established in which the donor would have a higher affinity than the acceptor probe to exhibit a stronger interaction with the target as to mimic the LNA capture probe employed in the traditional set-up as well as to ensure excitation to the acceptor. The acceptor probe, on the other hand, had a lower affinity to permit more transient interaction with the target and therefore allow for the generation of a unique fingerprint distinguishable from background. Several acceptor probes were investigated with varying length, leading to different GC%, in

different conditions to determine which was the most effective for downstream *in situ* detection application. Other miRNA FRET probe pairs were also investigated and showed effective FRET but need further optimization. For the application in cells, cell fixation and permeabilization conditions were investigated for suitable miRNA detection. PFA and an additional fixative were used, as miRNA have been shown to leak out during further processing. Permeabilization conditions were chosen based on which resulted in less removal of biochemical information. Finally, the FRET detector probes were applied to an *in situ* setting and demonstrated the capability of detection utilizing this assay.

Chapter 3 aimed to further expand the scope of miRNA detection in single cells. Contrary to Chapter 2, the technology explored in this chapter was not capable of retaining spatial expression, however it introduced the ability to analyze single CTCs by exploring an automated approach. Microfluidic technology was incorporated into the assay to use the full potential of SiMREPS with the goal of developing a high throughput (automated) assay to uncover heterogeneity across single cells. The Fluidigm C1 was utilized for processing cells for subsequent analysis via SiMREPS. The cells were isolated into 96 wells and were then lysed and harvested for miRNA detection via kinetic fingerprinting. Despite the high success (~90%) in isolation and lysis of single cells, harvesting required a much large volume and therefore necessitating reconcentration. To alleviate this issue, ATPS was applied for enrichment of biomolecules as shown for DNA [146]. This technique showed the capability of up to a ~14-fold improvement in sensitivity. Additionally, the detector probe conditions were optimized to decrease data acquisition time. This resulted in the ability to image more FOVs, and therefore, increase sensitivity further by ~2-fold. The surface area and volume were adjusted to improve diffusion and enhance capture efficiency. The switch from the traditional 5 mm cut-pipette tip

wells to a 3D-printed well strip with diameter of 1.2 mm resulted in a 5-fold increase in counts per FOV. Overall, the application of ATPS and 3D-printed wells achieved detection of let-7a in single cells.

4.2 Outlook/Future Directions

The FRET *in situ* detection assay presented in Chapter 2 describes an improved assay for identification and quantification of miRNA in fixed single cells. However, there were issues with high background which can be further improved. One particular approach to build on the assay described is to utilize expansion microscopy (ExM). Given the limitation in resolution of a light microscope, ExM was developed to increase the resolution by expanding biological specimens utilizing a polymer gel while retaining the spatial expression of the starting sample. The first reported protocol for ExM required the synthesis of labeling reagents for tagging proteins of interest [154], but now scientists have advanced the technique and users can anchor proteins or RNA of interest and fluorescently tag them before or after expansion [134]. The application of SiMREPS in an expanded specimen was considered and studied to alleviate crowding of biomolecules and/or reduce background. The investigation was described in **Section 2.4.6**, and due to the nature of the technique and the requirements of SiMREPS, there was a lack of compatibility. SiMREPS requires the use of salts to achieve the transient hybridization necessary to achieve a kinetic signature, while expanded specimens will shrink dramatically in the presence of salts as electrostatic repulsion between the polymer chains is shielded by the free ions.

A recent protocol, termed locked expansion microscopy (locked-ExM) also referred to as "mechanically locked expansion microscopy," was developed to integrate super-resolution techniques that typically use imaging buffers to control the photophysics of fluorophores. Previously, anti-photobleaching buffers such as the standard stochastic optical reconstruction

microscopy (STORM) buffer that utilizes 10 mM NaCl was not compatible with traditional expansion microscopy. In comparison to other published protocols [154–157], this method incorporated a different polymer, a non-ionic hydrophilic polymer, to offer a "mechanical" support to resist deswelling. With the introduction of this secondary polymer network, poly(ethylene glycol) (PEG), to lock the size of the expanded polyacrylate gels, we could achieve high resolution and improve our assay. Once this is achieved, detection should be more straight forward by facilitating access to miRNA in a very crowded environment. Additionally, if this application proves successful, with the increased resolution achieved via expansion, this technique lends itself to multiplexing of miRNA or other analytes simultaneously which can further advance the application of SiMREPS.

There is also the possibility of further improvements to the assay utilizing microfluidics for single cell isolation and lysis in combination with SiMREPS. Chapter 3 established that SiMREPS with ATPS enrichment could detect low concentrations of molecules from a single lysed cell. However, it was clear that the ATPS is not robust as it was for DNA. The difference in size as well as the interactions miRNA has with Ago protein, may be causing a change in partitioning than that observed for DNA. Given that the APTS composition is suitable for DNA, this assay be further improved by facilitating the transport of miRNA utilizing DNA as a "carrier" as described in **Section 3.4.6**. The DNA would help in transporting the miRNA into the salt-rich phase. Once in the salt-rich phase, the miRNA can diffuse faster than within the original sample volume and be captured by a 9-10 nt complementary LNA capture probe. To free the miRNA for detection, we would employ a toehold exchange mechanism. This optimization could enhance the sensitivity of our ATPS-SiMREPS assay and permit analysis of the single cell

lysates with a higher resolution and minimal change in the design. Alternatively, the ATPS can be investigated and optimized for the efficient partitioning of miRNA.

Since miRNA detection in ATPS has not been consistent, we could also alter the assay. One design change would be to utilize a different microfluidic system. As mentioned in **Section 3.5**, there is a microfluidic chip with a microwell array on top of a glass coverslip that isolates and traps single cells into individual chambers [152,153]. Similar to the Fluidigm IFC, this device permits single cell isolation and subsequent processing within an individual well. In contrast to the Fluidigm chip, the use of the glass coverslip permits for functionalization on the surface. The coverslip is functionalized with oligo(dT) primers that permit RNA capture of the single cells. Similar to SiMREPS, we could employ this device and utilize our mPEG:biotin-PEG functionalized coverslips for miRNA capture and subsequent TIRF imaging which was not possible with the Fluidigm IFC. With this new design, it would eliminate the necessitation of the ATPS since the harvesting step would be removed. Additionally, this device was also developed for mRNA capture utilizing beads functionalized with oligo(dT) primers. If utilized in combination with a mPEG:biotin-PEG functionalized coverslip, both miRNA and mRNA expression profiles can be investigated which would enhance our understanding of gene expression regulation within cells.

Overall, with further development, we could utilize these techniques to their full potential. With ExM, we can gain access to better resolution while with microfluidics we can reduce turnaround time and gain portability, making these assays ideal for point-of-care devices. In addition, these devices have the potential to evaluate multiple analytes at once giving us access to multidimensional analysis. In the early 2000s, the significance of miRNA was slowly being uncovered and now with the advancement in science as shown in this thesis, it is possible

to study its presence and behavior in single cells and future work will further open windows to readily investigate the synchronization of miRNA, mRNA, and/or protein expression necessary to sustain or disrupt a cell.

Appendix
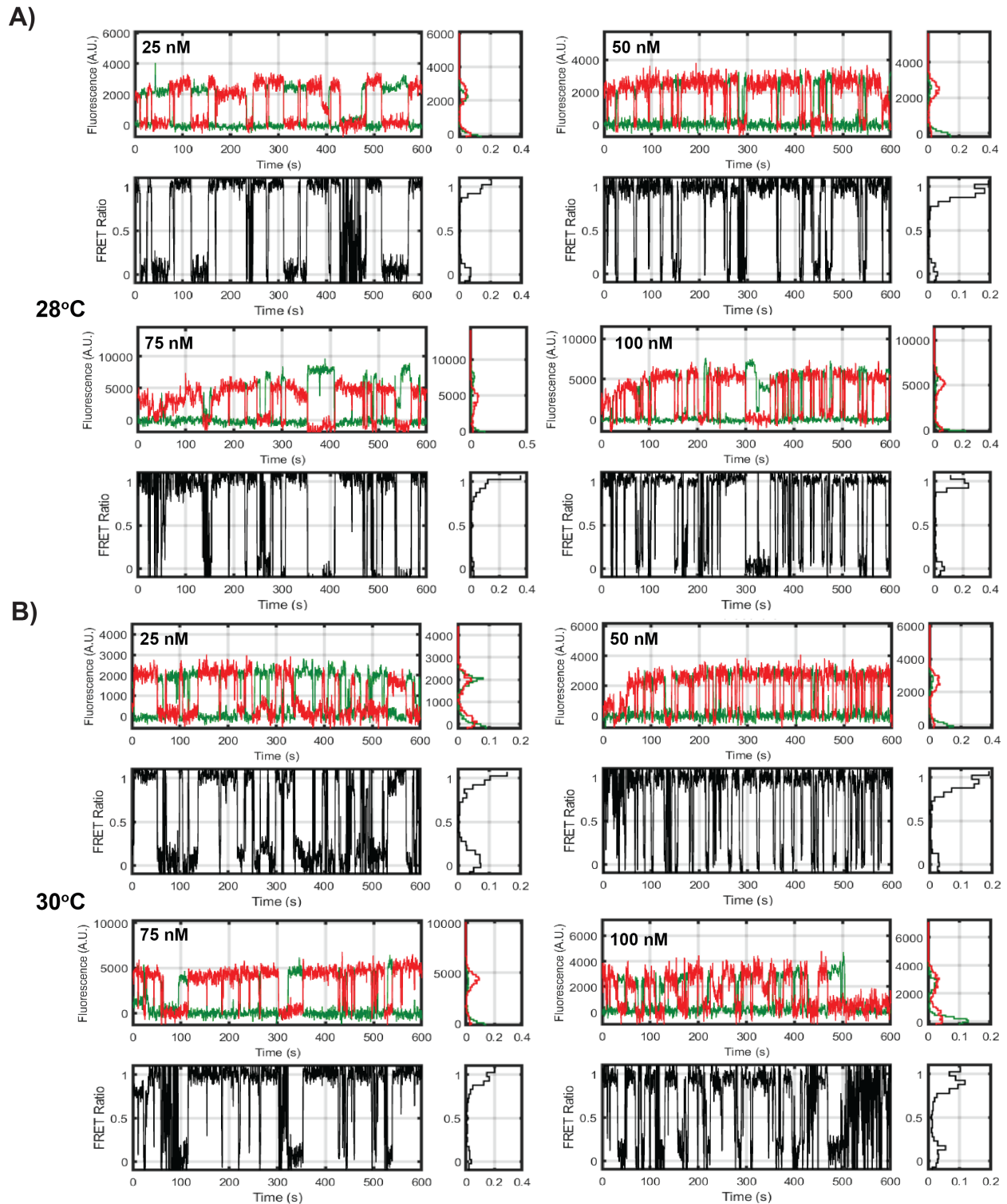
Appendix Figure 1 Representative FRET traces for let-7a detection across two temperatures. Each temperature was combined with a different FP concentration ranging from 25-100 nM. A) Traces obtained for temperature 28C. B) Traces obtained for temperature 30C.
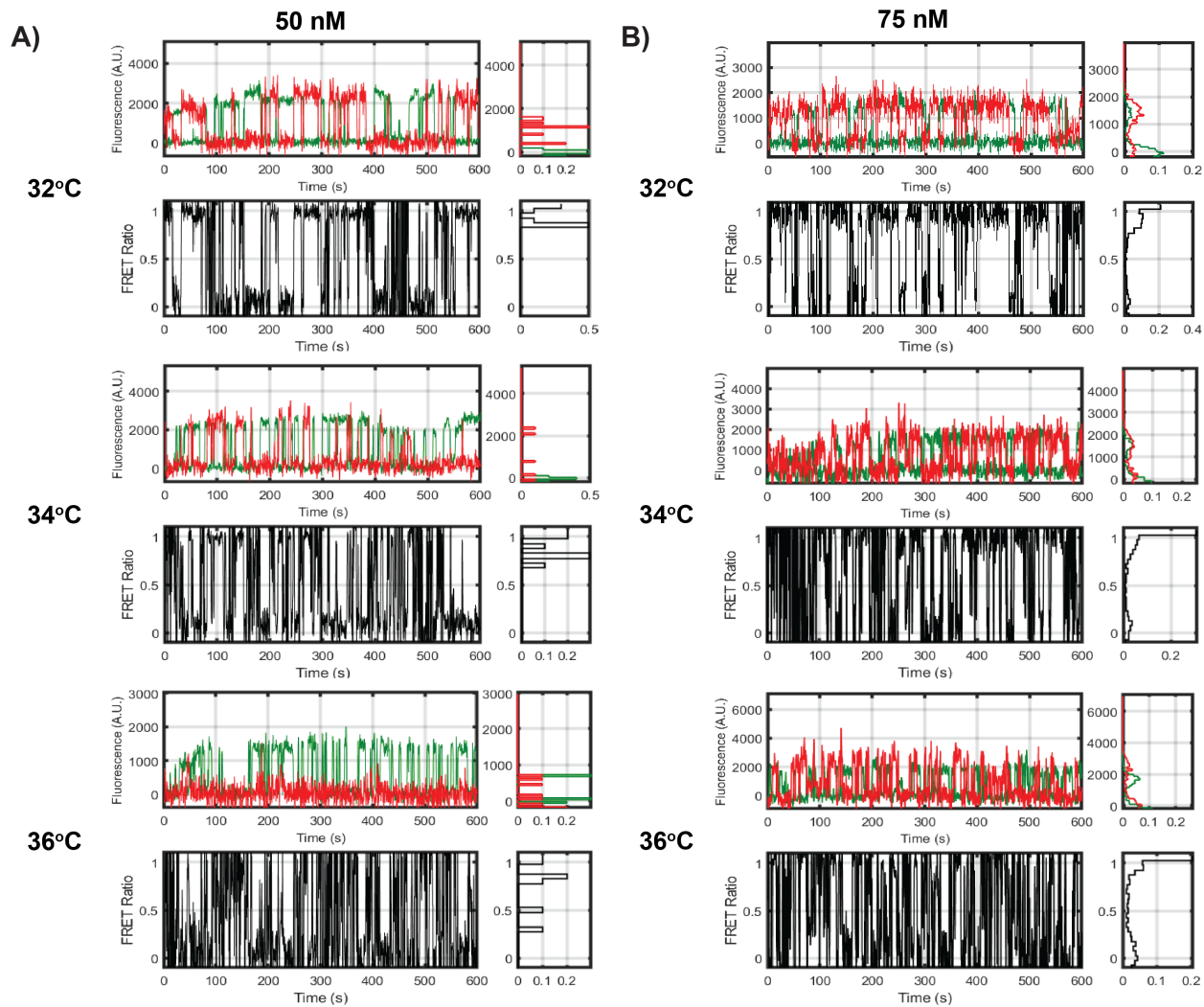
Appendix Figure 2 Representative FRET traces for let-7a detection across two concentrations. Each concentration was combined with a different temperature ranging from 32-26C. A) Traces obtained from using 50 nM FP. B) Traces obtained from using 75 nM FP.

A)

miR-21 probe	Sequence	T$_m$(°C)	GC%
Cy3FP1	/5Cy3/CTGATAAGCTA	28.6/29.8	36.4
Cy5FP1	TCAACATCA/3Cy5/	17.5/18.6	33.3
Cy5FP2	TCA ACA TCA G/3Cy5/	22.2/23.2	40

B)

miR-16 probes	Sequence	T$_m$(°C)	GC%
Cy3FP1	/5Cy3/GTG CTG CTA	33.4/34.3	55.6
Cy5FP1	GCCAATATT/3Cy5/	23.2/24.4	33.3
Cy3FP1	CGCCA ATATTT/3Cy3/	34.4/35.6	36.4
Cy5FP2	/5Cy5/TGCTGCTA	22.9/23.8	50
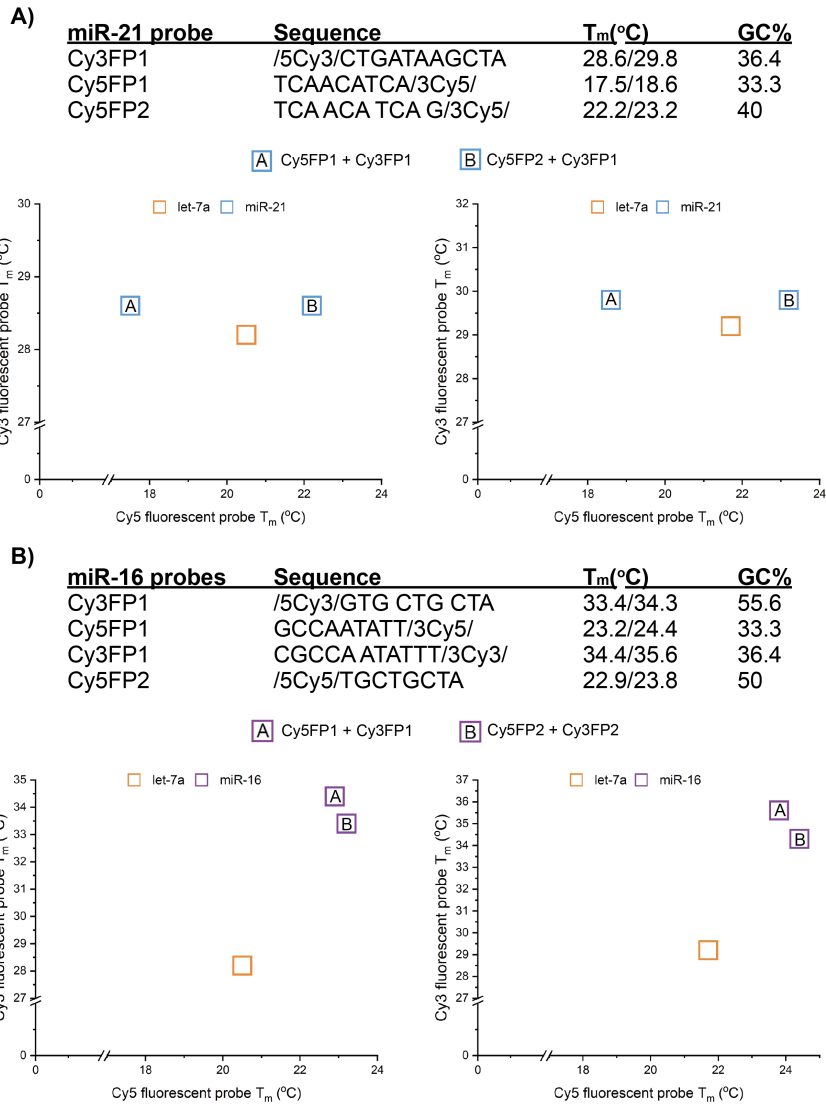
Appendix Figure 3 FRET pair probes selected for investigation. Probes were chosen to have similar melting temperatures to those found optimal for the let-7a pair probes. A) Table of miR-21 probes selected. Tm is provided for 4×/6× PBS conditions. Plots compare the selection pairs (blue) to the conditions of let-7a (orange). B) Table and representative comparison plots for miR-16.
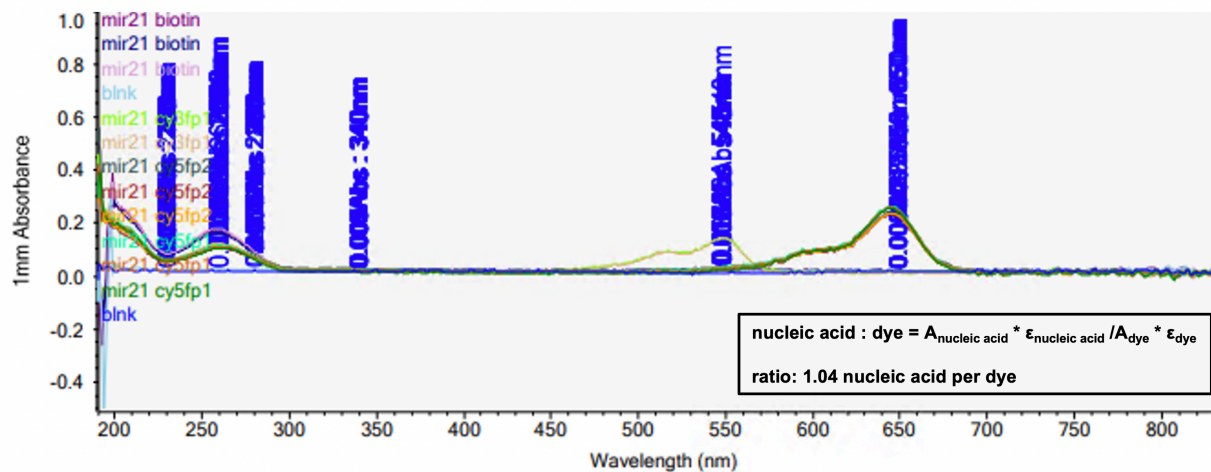
Appendix Figure 4 Absorbance vs wavelength for miR-21 Cy3FP1 graph. Calculation of ratio of nucleic acid to dye for miR-21 Cy3FP1.

C1™ Script Builder™

Name	Lysis Only Updated
Version	1
Description	Protocol for lysis and harvesting of single cells without RT steps or amplification.
Authors	
Institution	
Lab	
Special Instructions	

Cell Load and Stain

Capture

Sample Prep

Lysis   Harvest
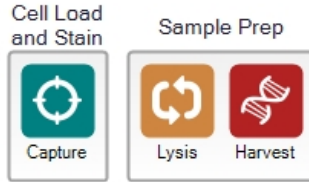
Script Summary - Prime	
Runtime Estimates	
Barcode	**Estimate**
1861x (5-10 um diameter cells)	0 hours, 11 minutes
1862x (10-17 um diameter cells)	0 hours, 13 minutes
1863x (17-25 um diameter cells)	0 hours, 12 minutes
Script Summary - Cell Load and Stain	
Runtime Estimates	
Barcode	**Estimate**
1861x (5-10 um diameter cells)	0 hours, 9 minutes
1862x (10-17 um diameter cells)	0 hours, 18 minutes
1863x (17-25 um diameter cells)	0 hours, 13 minutes
Script Summary - Sample Prep	
Runtime Estimates	
Barcode	**Estimate**
1861x (5-10 um diameter cells)	1 hours, 25 minutes
1862x (10-17 um diameter cells)	1 hours, 25 minutes
1863x (17-25 um diameter cells)	1 hours, 25 minutes

Incubation Profile			
Script Step	**Operation**	**Temperature (C)**	**Duration (s)**
Lysis	Incubation	25	300

C1™ Script Builder™

Script Reagent Details - Prime
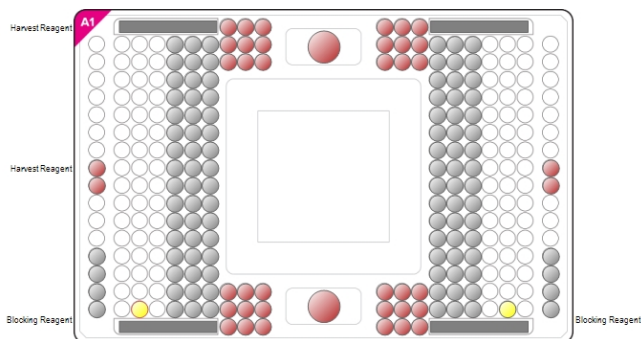
Reagent Loading			
Name	**Volume (µl)**	**IFC Inlet**	**Notes**
● Harvest Reagent	200 µl	A1	
● Harvest Reagent	200 µl	A2	
● Blocking Reagent	♻ 15 µl	C1	
● Blocking Reagent	15 µl	C2	
● Harvest Reagent	20 µl	P1	
● Harvest Reagent	20 µl	P2	

Reagent Mix Recipe - Prime			
Blocking Reagent			
Reagent (Stock Concentration)	**Mix Prep (µl)**	**Prep Conc.**	**Chamber Conc.**
C1 Blocking RGT (1X)			
Harvest Reagent			
Reagent (Stock Concentration)	**Mix Prep (µl)**	**Prep Conc.**	**Chamber Conc.**
C1 Harvest RGT (1X)			

126

C1™ Script Builder™

Script Reagent Details - Cell Load and Stain
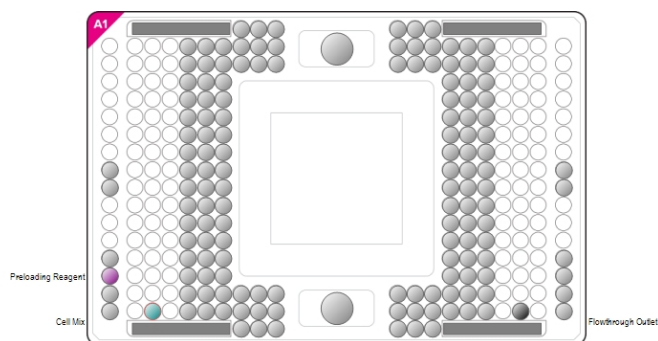
Inlet Reuse		
Name	**IFC Inlet**	**Instructions**
● Cell Mix	C1	Aspirate inlet prior to loading reagents
● Flowthrough Outlet	C2	Aspirate inlet prior to loading reagents (1862x, 1863x only)

Reagent Loading			
Name	**Volume (µl)**	**IFC Inlet**	**Notes**
● Preloading Reagent	24	2	
● Cell Mix	♻ 6	C1	

Reagent Mix Recipe - Cell Load and Stain

Preloading Reagent			
Reagent (Stock Concentration)	**Mix Prep (µl)**	**Prep Conc.**	**Chamber Conc.**
C1 Preloading RGT (1X)			

Cell Mix			
Reagent (Stock Concentration)	**Mix Prep (µl)**	**Prep Conc.**	**Chamber Conc.**
Suspension Reagent (2.5X)	40	1	1
Cells 66-330 / µL	60		

100 Total Prep Volume

127

C1™ Script Builder™

Script Reagent Details - Sample Prep

Reagent Loading

Name	Volume (µl)	IFC Inlet	Notes
● Preloading Reagent	0	2	
● Lysis Inhibitor Mix	7	3	
● Harvest Reagent	180 µl each	Harvest Inlets	

Reagent Mix Recipe - Sample Prep

Preloading Reagent

Reagent (Stock Concentration)	Mix Prep (µl)	Prep Conc.	Chamber Conc.
C1 Preloading RGT (1X)			

Lysis Inhibitor Mix (Secondary)

Reagent (Stock Concentration)	Mix Prep (µl)	Prep Conc.	Chamber Conc.
RNase Inhibitor (40 U/µl)	1	2	
Lysis Plus Reagent	19		

20 Total Prep Volume

Lysis Inhibitor Mix

Special Instructions:

Thaw all reagents on ice. Gently vortex each reagent and briefly spin down before adding to a tube labeled as "Lysis Mix". Store the Lysis Mix on ice.

Reagent (Stock Concentration)	Mix Prep (µl)	Prep Conc.	Chamber Conc.
C1 Lysis Plus Reagent	2.55		
C1 DNA Dilution Reagent (20X)	0.9	1	0.667
Single Cell Lysis Solution	12.75		
Lysis Inhibitor Mix	1.8		

18 Total Prep Volume

C1™ Script Builder™

Harvest Reagent

Reagent (Stock Concentration)	Mix Prep (µl)	Prep Conc.	Chamber Conc.
C1 Harvest Reagent (1X)			

129

C1™ Script Builder™

Protocol Reagent Shopping List

Reagent Name	Vendor	Part Number	Kit Part Number	Stock Concentration
Single Cell Lysis Solution	Life Technologies			

Fluidigm Reagent Kits

Reagent Name	Part Number	Stock Concentration	PN 100-8920	PN 100-6201	PN 100-7357	PN 100-5319	PN 100-8921
C1 Blocking RGT	100-5316	1X	☑	☑	☑	☑	
C1 Harvest RGT	100-6248	1X	☑	☑	☑		
C1 Preloading RGT	100-5311	1X	☑	☑	☑	☑	
Suspension Reagent	100-5315	2.5X	☑	☑	☑	☑	
C1 Lysis Plus Reagent							
C1 DNA Dilution Reagent	100-5170	20X	☑	☑			☑
C1 Harvest Reagent	100-6248	1X	☑	☑	☑		

Appendix Figure 5 C1 script protocol worksheet.
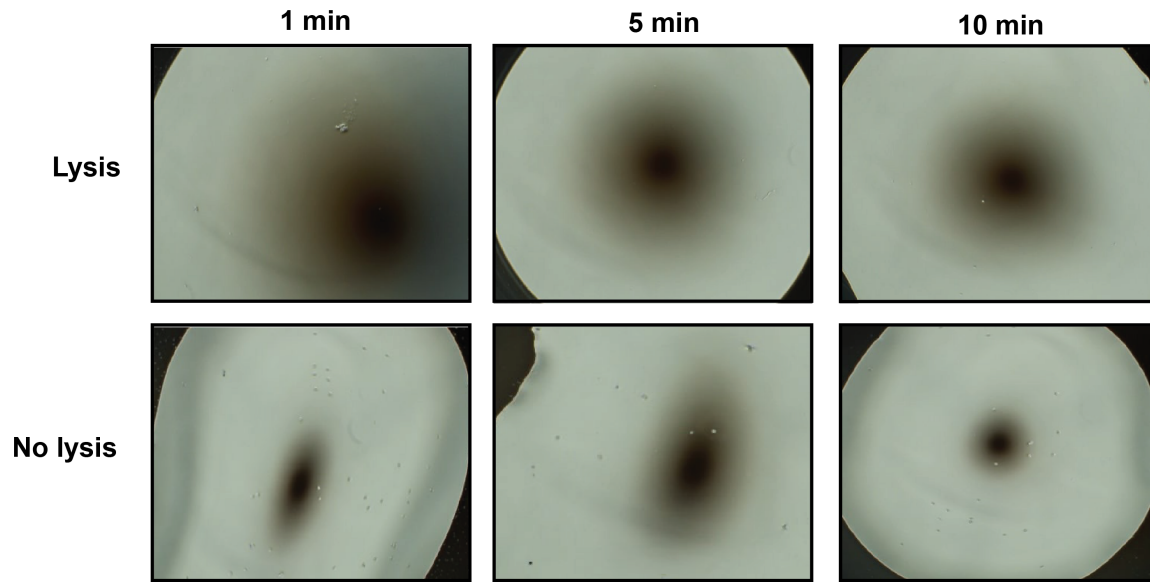
Appendix Figure 6 Cell lysis (top) over a 10 minute frame. Around 1000 cells/uL were exposed to lysis buffer. A control was included (bottom) to compare across all time points.
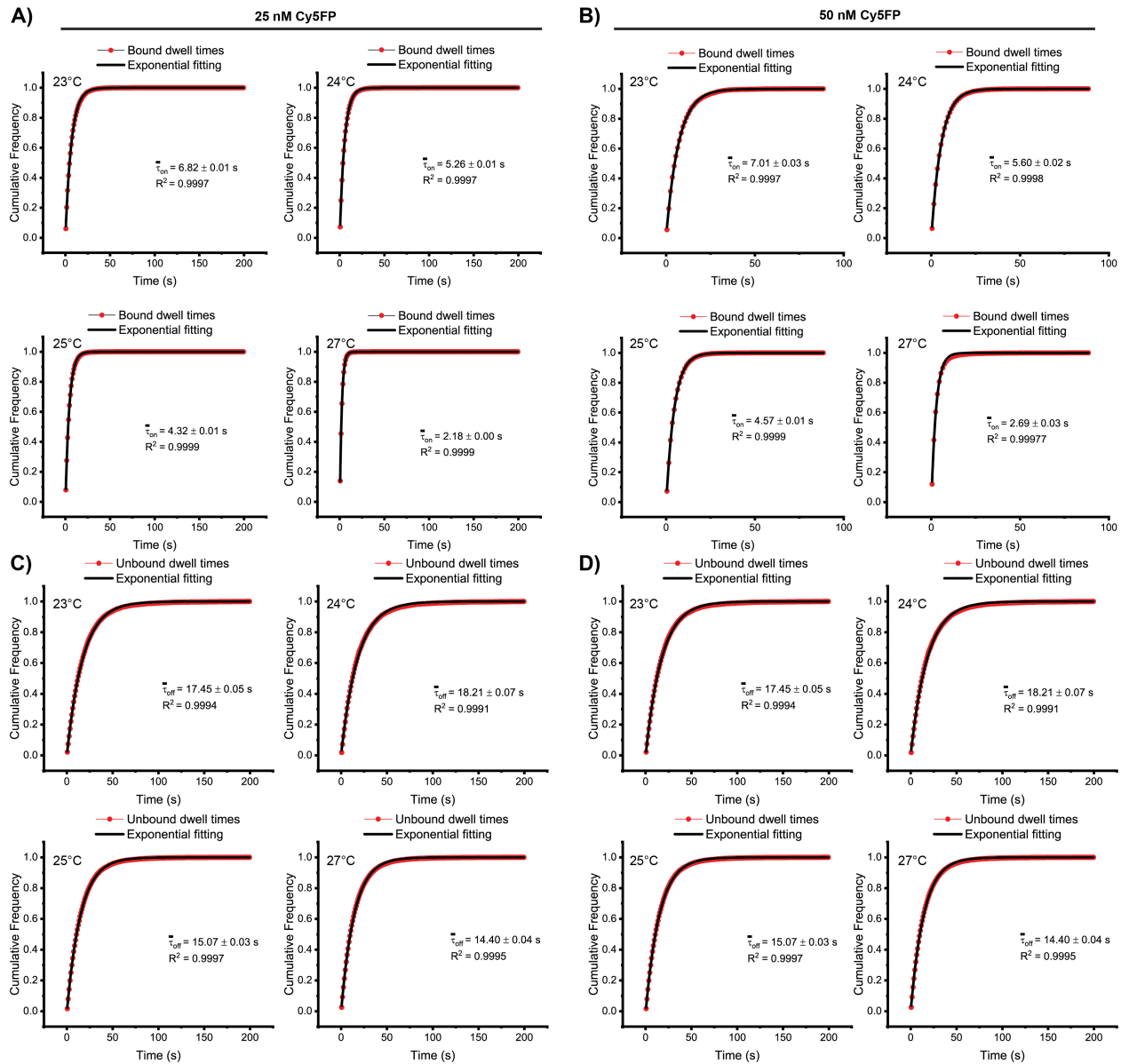
Appendix Figure 7 Exponential fitting of dwell time cumulative frequency for let-7a target bound ($\bar{\tau}_{on}$) and non-target-bound ($\bar{\tau}_{off}$) states for the corresponding FP concentrations 25 nM and 50 nM, respectively. A) Experiment was performed in imaging conditions: [FP] = 25 nM, [Na$^+$] = 580 nM. (4X PBS), Exposure time = 500 ms, Number of frames = 1200. B) Experiment was performed in imaging conditions: [FP] = 50 nM, [Na$^+$] = 580 nM. (4X PBS), Exposure time = 500 ms, Number of frames = 1200. The time (t1) listed reflects the dwell time calculated from the fitted curve using all accepted traces for each condition.
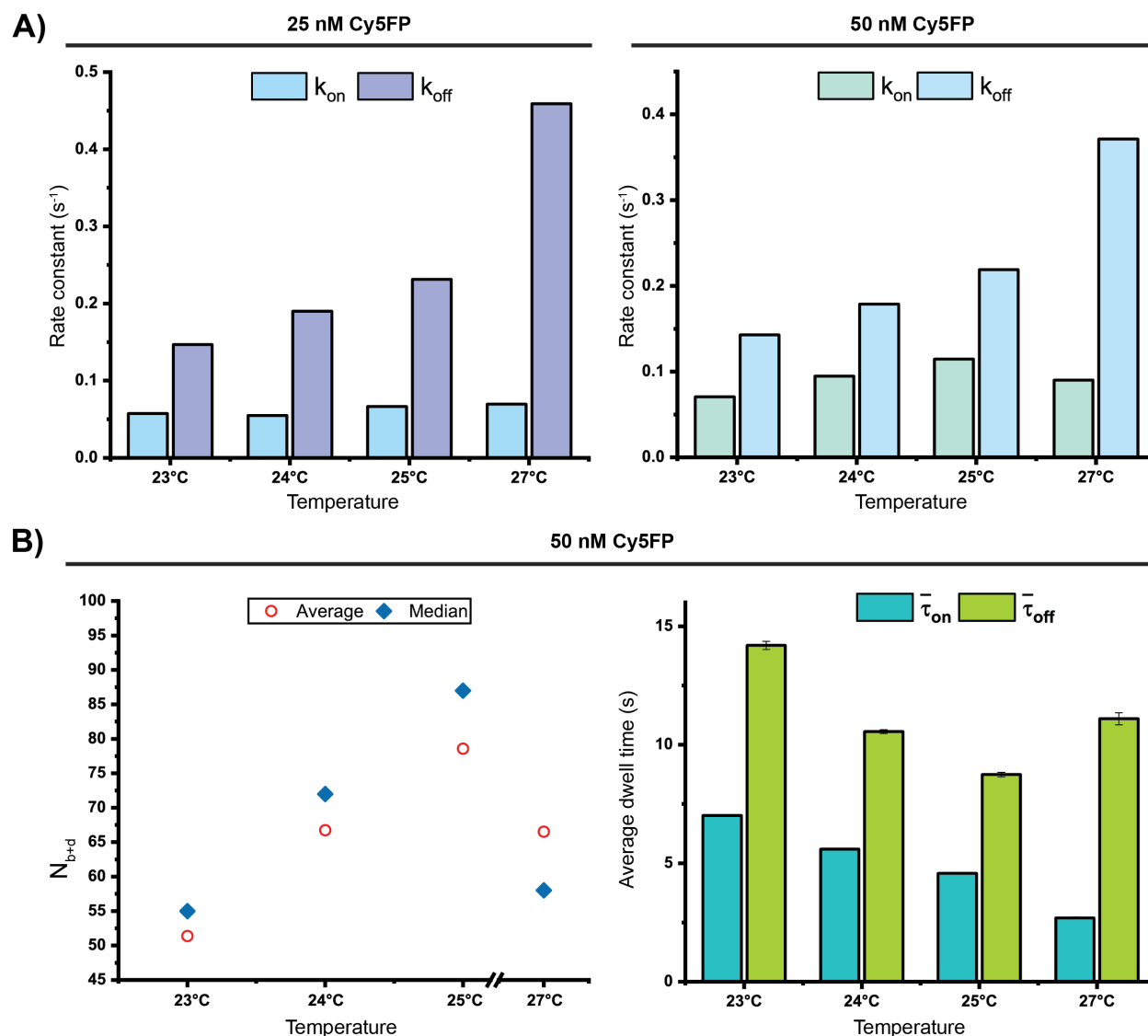
Appendix Figure 8 Effects of fluorescent probe concentration for detecting 400 fM of spiked in let-7a. A) Association (k_{on}) and dissociation rates (k_{off}) of 25 nM and 50 nM fluorescent probe, respectively, binding to the target let-7a. C) The average and median N_{b+d} exhibited by the detector probe at 50 nM fluorescent probe (left). The average dwell times the detector probe spent in the bound ($\bar{\tau}_{on}$) and unbound state ($\bar{\tau}_{off}$) when in presence of 50 nM fluorescent probe (right).
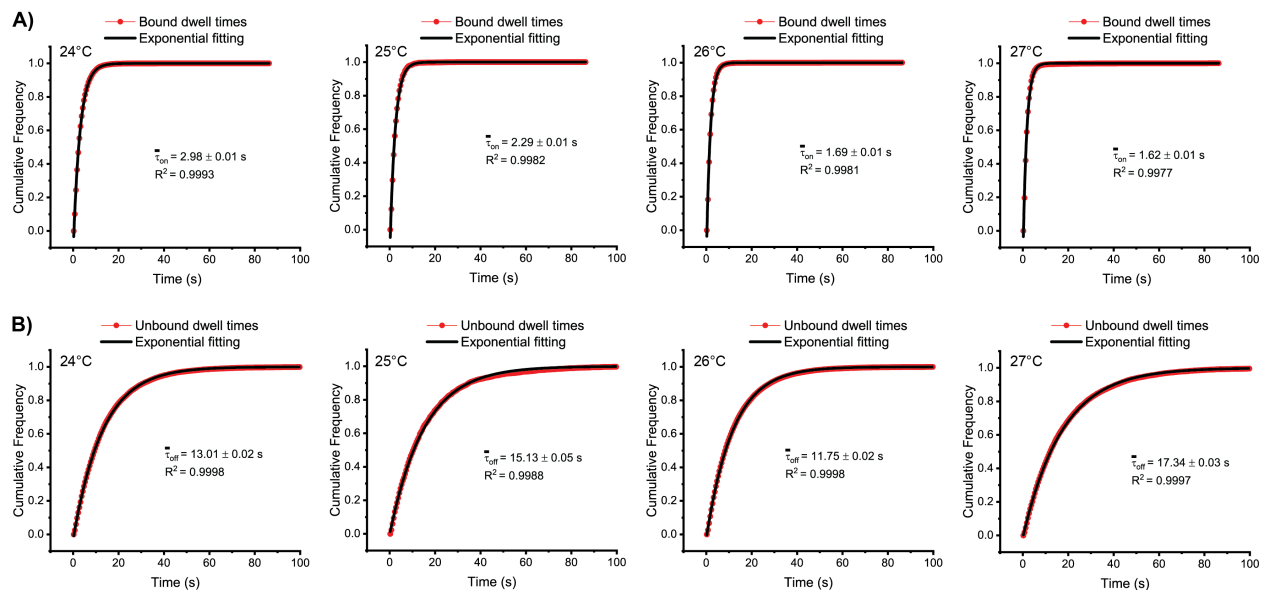
Appendix Figure 9 Exponential fitting of dwell time cumulative frequency for let-7a A) target bound ($\bar{\tau}_{on}$) and B) non-target-bound ($\bar{\tau}_{off}$) states for the corresponding temperatures: 24 °C, 25 °C, 26 °C, 27 °C. Experiment was performed in imaging conditions: [FP] = 25 nM, [Na$^+$] = 580 nM. (4X PBS), Exposure time = 500 ms, Number of frames = 600. The time (t1) listed reflects the dwell time calculated from the fitted curve using all accepted traces for each condition.

Bibliography

[1] Gest H. The discovery of microorganisms by Robert Hooke and Antoni van Leeuwenhoek, Fellows of The Royal Society. Notes Rec R Soc Lond. 2004;58:187–201.

[2] Nagai H, Kim YH. Cancer prevention from the perspective of global cancer burden patterns. J Thorac Dis. 2017;9:448–451.

[3] Cancer | CDC [Internet]. 2020 [cited 2022 Feb 4]. Available from: https://www.cdc.gov/chronicdisease/resources/publications/factsheets/cancer.htm.

[4] Nowell PC. The Clonal Evolution of Tumor Cell Populations. Science [Internet]. 1976 [cited 2022 Feb 3]; Available from: https://www.science.org/doi/abs/10.1126/science.959840.

[5] Malone ER, Oliva M, Sabatini PJB, et al. Molecular profiling for precision cancer therapies. Genome Med. 2020;12:8.

[6] Hassanpour SH, Dehghani M. Review of cancer from perspective of molecular. Journal of Cancer Research and Practice. 2017;4:127–129.

[7] Wang W, Quan Y, Fu Q, et al. Dynamics between Cancer Cell Subpopulations Reveals a Model Coordinating with Both Hierarchical and Stochastic Concepts. PLoS One. 2014;9:e84654.

[8] Dagogo-Jack I, Shaw AT. Tumour heterogeneity and resistance to cancer therapies. Nat Rev Clin Oncol. 2018;15:81–94.

[9] Yang C, Xia B-R, Jin W-L, et al. Circulating tumor cells in precision oncology: clinical applications in liquid biopsy and 3D organoid model. Cancer Cell International. 2019;19:341.

[10] Akpe V, Kim TH, Brown CL, et al. Circulating tumour cells: a broad perspective. Journal of The Royal Society Interface. 2020;17:20200065.

[11] Krebs MG, Hou J-M, Ward TH, et al. Circulating tumour cells: their utility in cancer management and predicting outcomes. Ther Adv Med Oncol. 2010;2:351–365.

[12] Toss A, Mu Z, Fernandez S, et al. CTC enumeration and characterization: moving toward personalized medicine. Ann Transl Med. 2014;2:108.

[13] Agnoletto C, Corrà F, Minotti L, et al. Heterogeneity in Circulating Tumor Cells: The Relevance of the Stem-Cell Subset. Cancers (Basel). 2019;11:483.

[14] Keller L, Pantel K. Unravelling tumour heterogeneity by single-cell profiling of circulating tumour cells. Nat Rev Cancer. 2019;19:553–567.

[15] Brandwein R-M. Liquid Biopsy—Changing How We Diagnose and Treat Cancer [Internet]. The Foundation For Gender-Specific Medicine. 2017 [cited 2022 Nov 23]. Available from: https://gendermed.org/liquid-biopsy-changing-diagnose-treat-cancer/.

[16] Crick FHC. ON PROTEIN SYNTHESIS. molecular biology. 1956;27.

[17] Crick F. Central Dogma of Molecular Biology. 1970;3.

[18] Sana J, Faltejskova P, Svoboda M, et al. Novel classes of non-coding RNAs and cancer. Journal of Translational Medicine. 2012;10:103.

[19] Lee RC, Feinbaum RL, Ambros V. The C. elegans heterochronic gene lin-4 encodes small RNAs with antisense complementarity to lin-14. Cell. 1993;75:843–854.

[20] miRBase [Internet]. [cited 2022 Feb 15]. Available from: https://www.mirbase.org/summary.shtml?org=hsa.

[21] Bartel DP. MicroRNAs: Target Recognition and Regulatory Functions. Cell. 2009;136:215–233.

[22] Ameres SL, Zamore PD. Diversifying microRNA sequence and function. Nat Rev Mol Cell Biol. 2013;14:475–488.

[23] Jonas S, Izaurralde E. Towards a molecular understanding of microRNA-mediated gene silencing. Nat Rev Genet. 2015;16:421–433.

[24] Huntzinger E, Izaurralde E. Gene silencing by microRNAs: contributions of translational repression and mRNA decay. Nat Rev Genet. 2011;12:99–110.

[25] Brennecke J, Stark A, Russell RB, et al. Principles of MicroRNA–Target Recognition. PLoS Biol. 2005;3:e85.

[26] Friedman RC, Farh KK-H, Burge CB, et al. Most mammalian mRNAs are conserved targets of microRNAs. Genome Res. 2009;19:92–105.

[27] Sayed D, Abdellatif M. MicroRNAs in development and disease. Physiol Rev. 2011;91:827–887.

[28] Rottiers V, Näär AM. MicroRNAs in metabolism and metabolic disorders. Nat Rev Mol Cell Biol. 2012;13:239–250.

[29] Hwang H-W, Mendell JT. MicroRNAs in cell proliferation, cell death, and tumorigenesis. Br J Cancer. 2006;94:776–780.

[30] Carleton M, Cleary MA, Linsley PS. MicroRNAs and Cell Cycle Regulation. Cell Cycle. 2007;6:2127–2132.

[31] Esteller M. Non-coding RNAs in human disease. Nat Rev Genet. 2011;12:861–874.

[32] Hamam R, Hamam D, Alsaleh KA, et al. Circulating microRNAs in breast cancer: novel diagnostic and prognostic biomarkers. Cell Death Dis. 2017;8:e3045.

[33] Jansson MD, Lund AH. MicroRNA and cancer. Mol Oncol. 2012;6:590–610.

[34] Chen P-S, Su J-L, Hung M-C. Dysregulation of MicroRNAs in cancer. Journal of Biomedical Science. 2012;19:90.

[35] Krol J, Loedige I, Filipowicz W. The widespread regulation of microRNA biogenesis, function and decay. Nat Rev Genet. 2010;11:597–610.

[36] Tétreault N, De Guire V. miRNAs: their discovery, biogenesis and mechanism of action. Clin Biochem. 2013;46:842–845.

[37] Condrat CE, Thompson DC, Barbu MG, et al. miRNAs as Biomarkers in Disease: Latest Findings Regarding Their Role in Diagnosis and Prognosis. Cells. 2020;9:276.

[38] Zhang Y, Li M, Gao X, et al. Nanotechnology in cancer diagnosis: progress, challenges and opportunities. J Hematol Oncol. 2019;12:137.

[39] Mitchell PS, Parkin RK, Kroh EM, et al. Circulating microRNAs as stable blood-based markers for cancer detection. PNAS. 2008;105:10513–10518.

[40] Croce CM. Causes and consequences of microRNA dysregulation in cancer. Nat Rev Genet. 2009;10:704–714.

[41] MicroRNA dysregulation in cancer: diagnostics, monitoring and therapeutics. A comprehensive review. EMBO Molecular Medicine. 2012;4:143–159.

[42] Kreth S, Hübner M, Hinske LC. MicroRNAs as Clinical Biomarkers and Therapeutic Tools in Perioperative Medicine. Anesthesia & Analgesia. 2018;126:670–681.

[43] Chevillet JR, Lee I, Briggs HA, et al. Issues and Prospects of microRNA-Based Biomarkers in Blood and Other Body Fluids. Molecules. 2014;19:6080–6105.

[44] Sofi Ibrahim M, Kulesh DA, Saleh SS, et al. Real-Time PCR Assay To Detect Smallpox Virus. J Clin Microbiol. 2003;41:3835–3839.

[45] Mestdagh P, Hartmann N, Baeriswyl L, et al. Evaluation of quantitative miRNA expression platforms in the microRNA quality control (miRQC) study. Nat Methods. 2014;11:809–815.

[46] Cissell KA, Rahimi Y, Shrestha S, et al. Bioluminescence-based detection of microRNA, miR21 in breast cancer cells. Anal Chem. 2008;80:2319–2325.

[47] de Planell-Saguer M, Rodicio MC. Analytical aspects of microRNA in diagnostics: a review. Anal Chim Acta. 2011;699:134–152.

[48] de Planell-Saguer M, Rodicio MC. Detection methods for microRNAs in clinic practice. Clin Biochem. 2013;46:869–878.

[49] Zhang R, Chen B, Tong X, et al. Diagnostic accuracy of droplet digital PCR for detection of EGFR T790M mutation in circulating tumor DNA. Cancer Manag Res. 2018;10:1209–1218.

[50] Kim K, Oh J-W, Lee YK, et al. Associating and Dissociating Nanodimer Analysis for Quantifying Ultrasmall Amounts of DNA. Angew Chem Int Ed Engl. 2017;56:9877–9880.

[51] Digital direct detection of microRNAs using single molecule arrays - PubMed [Internet]. [cited 2022 Aug 24]. Available from: https://pubmed.ncbi.nlm.nih.gov/28637221/.

[52] Jin Z, Geißler D, Qiu X, et al. A Rapid, Amplification-Free, and Sensitive Diagnostic Assay for Single-Step Multiplexed Fluorescence Detection of MicroRNA. Angew Chem Int Ed Engl. 2015;54:10024–10029.

[53] Hayward SL, Lund PE, Kang Q, et al. Ultraspecific and Amplification-Free Quantification of Mutant DNA by Single-Molecule Kinetic Fingerprinting. J Am Chem Soc. 2018;140:11755–11762.

[54] Pritchard CC, Cheng HH, Tewari M. MicroRNA profiling: approaches and considerations. Nat Rev Genet. 2012;13:358–369.

[55] Kilic T, Erdem A, Ozsoz M, et al. microRNA biosensors: Opportunities and challenges among conventional and commercially available techniques. Biosens Bioelectron. 2018;99:525–546.

[56] Zhu C, Zhu L, Tan D, et al. Avenues Toward microRNA Detection In Vitro: A Review of Technical Advances and Challenges. Computational and Structural Biotechnology Journal. 2019;17:904–916.

[57] Mullis K, Faloona F, Scharf S, et al. Specific enzymatic amplification of DNA in vitro: the polymerase chain reaction. Cold Spring Harb Symp Quant Biol. 1986;51 Pt 1:263–273.

[58] Chugh P, Dittmer DP. Potential Pitfalls in microRNA Profiling. Wiley Interdiscip Rev RNA. 2012;3:601–616.

[59] Sreejith KR, Ooi CH, Jin J, et al. Digital polymerase chain reaction technology – recent advances and future perspectives. Lab Chip. 2018;18:3717–3732.

[60] Varkonyi-Gasic E, Wu R, Wood M, et al. Protocol: a highly sensitive RT-PCR method for detection and quantification of microRNAs. Plant Methods. 2007;3:12.

[61] Chen C, Ridzon DA, Broomer AJ, et al. Real-time quantification of microRNAs by stem–loop RT–PCR. Nucleic Acids Res. 2005;33:e179.

[62] Liu C-G, Calin GA, Meloon B, et al. An oligonucleotide microchip for genome-wide microRNA profiling in human and mouse tissues. Proc Natl Acad Sci U S A. 2004;101:9740–9744.

[63] Koshiol J, Wang E, Zhao Y, et al. Strengths and limitations of laboratory procedures for microRNA detection. Cancer Epidemiol Biomarkers Prev. 2010;19:907–911.

[64] Postel M, Roosen A, Laurent-Puig P, et al. Droplet-based digital PCR and next generation sequencing for monitoring circulating tumor DNA: a cancer diagnostic perspective. Expert Rev Mol Diagn. 2018;18:7–17.

[65] Motameny S, Wolters S, Nürnberg P, et al. Next Generation Sequencing of miRNAs – Strategies, Resources and Methods. Genes (Basel). 2010;1:70–84.

[66] Li BT, Janku F, Jung B, et al. Ultra-deep next-generation sequencing of plasma cell-free DNA in patients with advanced lung cancers: results from the Actionable Genome Consortium. Annals of Oncology. 2019;30:597–603.

[67] Mandal S, Li Z, Chatterjee T, et al. Direct kinetic fingerprinting for high-accuracy single-molecule counting of diverse disease biomarkers. Acc Chem Res. 2021;54:388–402.

[68] Acuña AU, Amat-Guerri F. Early History of Solution Fluorescence: The Lignum nephriticum of Nicolás Monardes. In: Berberan-Santos MN, editor. Fluorescence of Supermolecules, Polymers, and Nanosystems [Internet]. Berlin, Heidelberg: Springer; 2008 [cited 2022 Aug 23]. p. 3–20. Available from: https://doi.org/10.1007/4243_2007_006.

[69] Stokes GG. XXX. On the change of refrangibility of light. Philosophical Transactions of the Royal Society of London. 1852;142:463–562.

[70] Rotman B. MEASUREMENT OF ACTIVITY OF SINGLE MOLECULES OF β-D-GALACTOSIDASE*. Proc Natl Acad Sci U S A. 1961;47:1981–1991.

[71] Moerner WE, Kador L. Optical detection and spectroscopy of single molecules in a solid. Phys Rev Lett. 1989;62:2535–2538.

[72] Betzig E, Chichester RJ. Single Molecules Observed by Near-Field Scanning Optical Microscopy. Science. 1993;262:1422–1425.

[73] Shashkova S, Leake MC. Single-molecule fluorescence microscopy review: shedding new light on old problems. Biosci Rep. 2017;37:BSR20170031.

[74] Walter NG, Huang C-Y, Manzo AJ, et al. Do-it-yourself guide: How to use the modern single molecule toolkit. Nat Methods. 2008;5:475–489.

[75] Liu Z, Lavis LD, Betzig E. Imaging Live-Cell Dynamics and Structure at the Single-Molecule Level. Molecular Cell. 2015;58:644–659.

[76] Roy R, Hohng S, Ha T. A practical guide to single-molecule FRET. Nat Methods. 2008;5:507–516.

[77] Tokunaga M, Imamoto N, Sakata-Sogawa K. Highly inclined thin illumination enables clear single-molecule imaging in cells. Nat Methods. 2008;5:159–161.

[78] Jalihal AP, Lund PE, Walter NG. Coming Together: RNAs and Proteins Assemble under the Single-Molecule Fluorescence Microscope. Cold Spring Harb Perspect Biol. 2019;11:a032441.

[79] Lelek M, Gyparaki MT, Beliu G, et al. Single-molecule localization microscopy. Nat Rev Methods Primers. 2021;1:1–27.

[80] Xu J, Ma H, Liu Y. Stochastic optical reconstruction microscopy (STORM). Curr Protoc Cytom. 2017;81:12.46.1-12.46.27.

[81] McKinney SA, Joo C, Ha T. Analysis of Single-Molecule FRET Trajectories Using Hidden Markov Modeling. Biophysical Journal. 2006;91:1941–1951.

[82] Najkar N, Razzazi F, Sameti H. A novel approach to HMM-based speech recognition systems using particle swarm optimization. Mathematical and Computer Modelling. 2010;52:1910–1920.

[83] Li J, Zhang L, Johnson-Buck A, et al. Automatic classification and segmentation of single-molecule fluorescence time traces with deep learning. Nat Commun. 2020;11:5833.

[84] Fan HC, Blumenfeld YJ, Chitkara U, et al. Noninvasive diagnosis of fetal aneuploidy by shotgun sequencing DNA from maternal blood. Proc Natl Acad Sci U S A. 2008;105:16266–16271.

[85] Foulkes WD, Knoppers BM, Turnbull C. Population genetic testing for cancer susceptibility: founder mutations to genomes. Nat Rev Clin Oncol. 2016;13:41–54.

[86] Vasan RS. Biomarkers of cardiovascular disease: molecular basis and practical considerations. Circulation. 2006;113:2335–2362.

[87] Umek RM, Lin SS, Chen Yp Y, et al. Bioelectronic detection of point mutations using discrimination of the H63D polymorphism of the Hfe gene as a model. Mol Diagn. 2000;5:321–328.

[88] Kim NW, Wu F. Advances in quantification and characterization of telomerase activity by the telomeric repeat amplification protocol (TRAP). Nucleic Acids Res. 1997;25:2595–2597.

[89] van der Meide WF, Schoone GJ, Faber WR, et al. Quantitative Nucleic Acid Sequence-Based Assay as a New Molecular Tool for Detection and Quantification of Leishmania Parasites in Skin Biopsy Samples. J Clin Microbiol. 2005;43:5560–5566.

[90] Liu GY. Isolation, sequence identification, and tissue expression profile of 3 novel porcine genes: NCF2, BCKDHB and BCKDHA. J Appl Genet. 2009;50:47–50.

[91] Diaz LA, Bardelli A. Liquid biopsies: genotyping circulating tumor DNA. J Clin Oncol. 2014;32:579–586.

[92] Rybicka M, Stalke P, Bielawski KP. Current molecular methods for the detection of hepatitis B virus quasispecies. Rev Med Virol. 2016;26:369–381.

[93] Chen G, Mosier S, Gocke CD, et al. Cytosine deamination is a major cause of baseline noise in next-generation sequencing. Mol Diagn Ther. 2014;18:587–593.

[94] Chen L, Liu P, Evans T, et al. DNA damage is a pervasive cause of sequencing errors, directly confounding variant identification. Science. 2017;355:752–756.

[95] Potapov V, Ong JL. Examining Sources of Error in PCR by Single-Molecule Sequencing. PLOS ONE. 2017;12:e0169774.

[96] Kinde I, Wu J, Papadopoulos N, et al. Detection and quantification of rare mutations with massively parallel sequencing. Proc Natl Acad Sci U S A. 2011;108:9530–9535.

[97] Johnson-Buck A, Su X, Giraldez MD, et al. Kinetic fingerprinting to identify and count single nucleic acids. Nat Biotechnol. 2015;33:730–732.

[98] Johnson-Buck A, Li J, Tewari M, et al. A guide to nucleic acid detection by single-molecule kinetic fingerprinting. Methods. 2019;153:3–12.

[99] Chatterjee T, Li Z, Khanna K, et al. Ultraspecific analyte detection by direct kinetic fingerprinting of single molecules. TrAC Trends in Analytical Chemistry. 2020;123:115764.

[100] Floyd DL, Harrison SC, van Oijen AM. Analysis of Kinetic Intermediates in Single-Particle Dwell-Time Distributions. Biophys J. 2010;99:360–366.

[101] Li L, Yu Y, Wang C, et al. Transient Hybridization Directed Nanoflare for Single-Molecule miRNA Imaging. Anal Chem. 2019;91:11122–11128.

[102] Pena JTG, Sohn-Lee C, Rouhanifard SH, et al. miRNA in situ hybridization in mammalian tissues fixed with formaldehyde and EDC. Nat Methods. 2009;6:139–141.

[103] Schor SL, Schor AM. Tumour-stroma interactions: Phenotypic and genetic alterations in mammary stroma: implications for tumour progression. Breast Cancer Research. 2001;3:373.

[104] Binnewies M, Roberts EW, Kersten K, et al. Understanding the tumor immune microenvironment (TIME) for effective therapy. Nat Med. 2018;24:541–550.

[105] Östman A. The tumor microenvironment controls drug sensitivity. Nat Med. 2012;18:1332–1334.

[106] Deng R, Zhang K, Li J. Isothermal Amplification for MicroRNA Detection: From the Test Tube to the Cell. Acc Chem Res. 2017;50:1059–1068.

[107] Deng R, Tang L, Tian Q, et al. Toehold-initiated rolling circle amplification for visualizing individual microRNAs in situ in single cells. Angew Chem Int Ed Engl. 2014;53:2389–2393.

[108] Huber D, Voith von Voithenberg L, Kaigala GV. Fluorescence in situ hybridization (FISH): History, limitations and what to expect from micro-scale FISH? Micro and Nano Engineering. 2018;1:15–24.

[109] Pardini B, Sabo AA, Birolo G, et al. Noncoding RNAs in Extracellular Fluids as Cancer Biomarkers: The New Frontier of Liquid Biopsies. Cancers (Basel). 2019;11:1170.

[110] Drula R, Ott LF, Berindan-Neagoe I, et al. MicroRNAs from Liquid Biopsy Derived Extracellular Vesicles: Recent Advances in Detection and Characterization Methods. Cancers (Basel). 2020;12:2009.

[111] Kwon S. Single-molecule fluorescence in situ hybridization: quantitative imaging of single RNA molecules. BMB Rep. 2013;46:65–72.

[112] Cui C, Shu W, Li P. Fluorescence In situ Hybridization: Cell-Based Genetic Diagnostic and Research Applications. Frontiers in Cell and Developmental Biology [Internet]. 2016 [cited 2022 Nov 23];4. Available from: https://www.frontiersin.org/articles/10.3389/fcell.2016.00089.

[113] Haimovich G, Gerst JE. Single-molecule Fluorescence in situ Hybridization (smFISH) for RNA Detection in Adherent Animal Cells. Bio Protoc. 2018;8:e3070.

[114] Xie F, Timme KA, Wood JR. Using Single Molecule mRNA Fluorescent in Situ Hybridization (RNA-FISH) to Quantify mRNAs in Individual Murine Oocytes and Embryos. Sci Rep. 2018;8:7930.

[115] Moffitt JR, Hao J, Bambah-Mukku D, et al. High-performance multiplexed fluorescence in situ hybridization in culture and tissue with matrix imprinting and clearing. Proceedings of the National Academy of Sciences. 2016;113:14456–14461.

[116] Pena JTG, Sohn-Lee C, Rouhanifard SH, et al. miRNA in situ hybridization in formaldehyde and EDC-fixed tissues. Nat Methods. 2009;6:139–141.

[117] Bronson JE, Fei J, Hofman JM, et al. Learning Rates and States from Biophysical Time Series: A Bayesian Approach to Model Selection and Single-Molecule FRET Data. Biophysical Journal. 2009;97:3196–3205.

[118] Gaussian Blur - an overview | ScienceDirect Topics [Internet]. [cited 2022 Nov 15]. Available from: https://www.sciencedirect.com/topics/engineering/gaussian-blur.

[119] Li Y, Yong B, Wu H, et al. An Improved Top-Hat Filter with Sloped Brim for Extracting Ground Points from Airborne Lidar Point Clouds. Remote Sensing. 2014;6:12885–12908.

[120] Lu M, Zhang Q, Deng M, et al. An Analysis of Human MicroRNA and Disease Associations. PLOS ONE. 2008;3:e3420.

[121] Ruepp A, Kowarsch A, Schmidl D, et al. PhenomiR: a knowledgebase for microRNA expression in diseases and biological processes. Genome Biology. 2010;11:R6.

[122] Russo F, Bella SD, Nigita G, et al. miRandola: Extracellular Circulating MicroRNAs Database. PLOS ONE. 2012;7:e47786.

[123] Hoffman EA, Frey BL, Smith LM, et al. Formaldehyde Crosslinking: A Tool for the Study of Chromatin Complexes. J Biol Chem. 2015;290:26404–26411.

[124] Tan W, Liu B, Qu S, et al. MicroRNAs and cancer: Key paradigms in molecular therapy (Review). Oncology Letters. 2018;15:2735–2742.

[125] Chirshev E, Oberg KC, Ioffe YJ, et al. Let-7 as biomarker, prognostic indicator, and therapy for precision medicine in cancer. Clin Transl Med. 2019;8:24.

[126] Barh D, Malhotra R, Ravi B, et al. Microrna let-7: an emerging next-generation cancer therapeutic. Curr Oncol. 2010;17:70–80.

[127] Vester B, Wengel J. LNA (locked nucleic acid): high-affinity targeting of complementary RNA and DNA. Biochemistry. 2004;43:13233–13241.

[128] Kretschy N, Sack M, Somoza MM. Sequence-Dependent Fluorescence of Cy3- and Cy5-Labeled Double-Stranded DNA. Bioconjugate Chem. 2016;27:840–848.

[129] Iqbal A, Wang L, Thompson KC, et al. The Structure of Cyanine 5 Terminally Attached to Double-Stranded DNA: Implications for FRET Studies. Biochemistry. 2008;47:7857–7862.

[130] Kretschy N, Somoza MM. Comparison of the Sequence-Dependent Fluorescence of the Cyanine Dyes Cy3, Cy5, DyLight DY547 and DyLight DY647 on Single-Stranded DNA. PLOS ONE. 2014;9:e85605.

[131] number of copies of the microRNA let-7 RNA pe - Human Homo sapiens - BNID 101301 [Internet]. [cited 2022 Nov 23]. Available from: https://bionumbers.hms.harvard.edu/bionumber.aspx?s=n&v=2&id=101301.

[132] Allawi HT, Dahlberg JE, Olson S, et al. Quantitation of microRNAs using a modified Invader assay. RNA. 2004;10:1153–1161.

[133] Shin S, Jung Y, Uhm H, et al. Quantification of purified endogenous miRNAs with high sensitivity and specificity. Nat Commun. 2020;11:6033.

[134] Wassie AT, Zhao Y, Boyden ES. Expansion microscopy: principles and uses in biological research. Nat Methods. 2019;16:33–41.

[135] Altschuler SJ, Wu LF. Cellular Heterogeneity: Do Differences Make a Difference? Cell. 2010;141:559–563.

[136] Hu P, Zhang W, Xin H, et al. Single Cell Isolation and Analysis. Front Cell Dev Biol. 2016;4:116.

[137] Tang F, Barbacioru C, Wang Y, et al. mRNA-Seq whole-transcriptome analysis of a single cell. Nat Methods. 2009;6:377–382.

[138] Navin N, Kendall J, Troge J, et al. Tumour evolution inferred by single-cell sequencing. Nature. 2011;472:90–94.

[139] Taniguchi K, Kajiyama T, Kambara H. Quantitative analysis of gene expression in a single cell by qPCR. Nat Methods. 2009;6:503–506.

[140] Citri A, Pang ZP, Sudhof TC, et al. Comprehensive qPCR profiling of gene expression in single neuronal cells. Nat Protoc. 2011;7:118–127.

[141] Stone HA, Stroock AD, Ajdari A. Engineering Flows in Small Devices: Microfluidics Toward a Lab-on-a-Chip. Annual Review of Fluid Mechanics. 2004;36:381–411.

[142] Sackmann EK, Fulton AL, Beebe DJ. The present and future role of microfluidics in biomedical research. Nature. 2014;507:181–189.

[143] Whitesides GM. The origins and the future of microfluidics. Nature. 2006;442:368–373.

[144] Chatterjee T, Knappik A, Sandford E, et al. Direct kinetic fingerprinting and digital counting of single protein molecules. Proceedings of the National Academy of Sciences. 2020;117:22815–22822.

[145] Weng R, Lou S, Li L, et al. Single-Molecule Kinetic Fingerprinting for the Ultrasensitive Detection of Small Molecules with Aptasensors. Anal Chem. 2019;91:1424–1431.

[146] Li Z, McNeely M, Sandford E, et al. Attomolar Sensitivity in Single Biomarker Counting upon Aqueous Two-Phase Surface Enrichment. ACS Sens. 2022;7:1419–1430.

[147] Raja S, Murty VR, Thivaharan V, et al. Aqueous Two Phase Systems for the Recovery of Biomolecules – A Review. Science and Technology. 2011;1:7–16.

[148] Iqbal M, Tao Y, Xie S, et al. Aqueous two-phase system (ATPS): an overview and advances in its applications. Biol Proced Online. 2016;18:18.

[149] Pandey A. Measurements of microbial growth [Internet]. Microbiology Notes. 2020 [cited 2022 Nov 23]. Available from: https://microbiologynotes.org/measurements-of-microbial-growth/.

[150] Pasteur research pasteur fr-Institut. Fluidigm C1 - single-cell profiling [Internet]. Research. [cited 2022 Nov 23]. Available from: https://research.pasteur.fr/en/equipment/single-cell-cdna-preparation/.

[151] Luechau F, Ling TC, Lyddiatt A. Selective partition of plasmid DNA and RNA in aqueous two-phase systems by the addition of neutral salt. Separation and Purification Technology. 2009;68:114–118.

[152] Yuan J, Sheng J, Sims PA. SCOPE-Seq: a scalable technology for linking live cell imaging and single-cell RNA sequencing. Genome Biology. 2018;19:227.

[153] Bose S, Wan Z, Carr A, et al. Scalable microfluidics for single-cell RNA printing and sequencing. Genome Biology. 2015;16:120.

[154] Chen F, Tillberg PW, Boyden ES. Expansion microscopy. Science. 2015;347:543–548.

[155] Gao R, Asano SM, Boyden ES. Q&A: Expansion microscopy. BMC Biology. 2017;15:50.

[156] Asano SM, Gao R, Wassie AT, et al. Expansion Microscopy: Protocols for Imaging Proteins and RNA in Cells and Tissues. Curr Protoc Cell Biol. 2018;80:e56.

[157] Truckenbrodt S, Sommer C, Rizzoli SO, et al. A practical guide to optimization in X10 expansion microscopy. Nat Protoc. 2019;14:832–863.